

**ELUCIDATING THE FRESH AND HARDENED PROPERTIES OF  
LIMESTONE CALCINED CLAY CEMENTS THROUGH DATA  
ANALYTICS**

A Dissertation  
Presented to  
The Academic Faculty

by

Oğulcan Canbek

In Partial Fulfillment  
of the Requirements for the Degree  
Doctor of Philosophy in the  
School of Civil and Environmental Engineering

Georgia Institute of Technology  
August 2022

**COPYRIGHT © 2022 BY OĞULCAN CANBEK**

# **ELUCIDATING THE FRESH AND HARDENED PROPERTIES OF LIMESTONE CALCINED CLAY CEMENTS THROUGH DATA ANALYTICS**

Approved by:

Dr. Kimberly E. Kurtis, Advisor  
School of Civil and Environmental  
Engineering  
*Georgia Institute of Technology*

Dr. Yajun Mei  
School of Industrial and Systems  
Engineering  
*Georgia Institute of Technology*

Dr. Newell R. Washburn  
Department of Chemistry  
*Carnegie Mellon University*

Dr. Susan E. Burns  
School of School of Civil and  
Environmental Engineering  
*Georgia Institute of Technology*

Dr. Iris Tien  
School of School of Civil and  
Environmental Engineering  
*Georgia Institute of Technology*

Date Approved: June 29, 2022

## ACKNOWLEDGEMENTS

I will forever be grateful to my advisor, Dr. Kimberly Kurtis, not only for scholarly reasons but also for my cultural experience at Georgia Tech. She brings wonderful people together and always fosters collaborations, which make personal and professional failure impossible. All these years I have been very fortunate to take tremendous support, encouragement, and guidance from her. I am also indebted to her for all the invaluable opportunities and inspirations she has provided me throughout my studies. I hope I can collaborate with her for years to come, also be invited to group celebrations.

I acknowledge the valuable contributions from my committee members Dr. Newell Washburn, Dr. Yajun Mei, Dr. Susan Burns and Dr. Iris Tien. I would like to express my sincere gratitude to Dr. Newell Washburn for providing me the opportunity to work in an interdisciplinary research project. His motivation and guidance helped me to stay in the right direction. I appreciate the knowledge Dr. Yajun Mei has taught me in his data science courses. I am also thankful for his contributions to my dissertation.

To my fellow colleagues from Kurtis group, I cannot thank you enough for your friendship and support. I was able to finish my dissertation thanks to the fun, creative and collaborative environment in our workspace for years, which I will always long for. To Dr. Francesca Lolli and Dr. Christopher Childs, thank you for your contributions to Chapter 6. I also thank Qunzhi Xu for his contributions to Chapter 4. I would also like to thank the wonderful undergraduate researchers who helped me all these years: Connor Szeto, Victoria Clark, and Alexandra Madriz Pizarro. Special thanks to Connor Szeto not only for

his contributions to this dissertation, but also for encouraging me in my mentorship with his decision to pursue a PhD in our research group.

To my beloved family and friends, I feel privileged every day because of you. No matter how much I thank you for your support, it will not be enough. Nevertheless, thank you for everything. Special thanks to my M.S. advisor in METU from Turkey, Dr. Sinan Turhan Erdoğan. Without his encouragement and mentorship during my M.S., I could not have been motivated to stay in graduate school, let alone complete a PhD in Georgia Tech.

I would like to acknowledge the funding source of this dissertation Advanced Research Projects Agency-Energy (ARPA-E). I would like to thank ARPA-E program director Dr. Joseph King who has always challenged me with his questions during our quarterly meetings. I am thankful to Georgia Tech Institute for Materials (IMat) for being awarded the Graduate Student Fellowship in 2020. I am also thankful to American Concrete Institute for being awarded Georgia ACI Robert H. Kulman and LaGrit F. “Sam” Morris Student Scholarship in 2021.

I would like to finish my words here with a note to the future members of Kurtis group. Perhaps you are reading this because you have already started planning your graduation. For what it's worth, I'd advise you to spend all your remaining free time in Atlanta with the people you care about. Because the time will fly, and when the day comes, farewells are not always bittersweet but sometimes they are bitter only. Also, thank you for reading my dissertation.

# TABLE OF CONTENTS

<b>ACKNOWLEDGEMENTS</b>	<b>iii</b>
<b>LIST OF TABLES</b>	<b>viii</b>
<b>LIST OF FIGURES</b>	<b>x</b>
<b>LIST OF SYMBOLS AND ABBREVIATIONS</b>	<b>xiv</b>
<b>SUMMARY</b>	<b>xvii</b>
<b>CHAPTER 1. Introduction</b>	<b>1</b>
1.1 Background	1
1.2 Motivation and Problem Statement	4
1.3 Objectives: Data Analytics Guided Design of LC <sup>3</sup>	8
1.4 Thesis Organization	10
<b>CHAPTER 2. Literature Review</b>	<b>12</b>
2.1 Kaolinite	12
2.2 Key Microstructural Concepts	15
2.2.1 Virtue of LC <sup>3</sup> : Carboaluminate Phases	15
2.2.2 The Filler Effect	18
2.2.3 Sulfate optimization	20
2.3 Property Evolution	23
2.3.1 Compressive Strength Development	23
2.3.2 Durability	24
2.3.3 Rheology	26
2.4 Summary of the Knowledge Gaps and Technical Needs Addressed	30
<b>CHAPTER 3. A Quantitative Approach to Determining Sulfate Balance for LC<sup>3</sup></b>	<b>33</b>
3.1 Introduction	33
3.2 Research Significance	35
3.3 Experimental	35
3.3.1 Materials	35
3.3.2 Mix design	38
3.3.3 Experimental	38
3.4 Computational methods	40
3.4.1 Regression model for predicting the sulfate balance of LC <sup>3</sup>	40
3.4.2 Kernel smoothing for parametrizing heat flow curves	43
3.5 Experimental Results	45
3.5.1 Influence of Metakaolin Fraction	45
3.5.2 Influence of Limestone Particle Size	49
3.5.3 Influence of Added Gypsum Amount	54
3.5.4 Influence of W/S	56
3.5.5 Influence of Superplasticizer Content	59

3.5.6	Relationship between the slope of silicate peak and sulfate depletion point	61
3.5.7	In-situ XRD to understand the sulfate balance	63
<b>3.6</b>	<b>Identification of the sulfate depletion point in undersulfated LC<sup>3</sup> systems</b>	<b>66</b>
<b>3.7</b>	<b>Statistical Results</b>	<b>68</b>
<b>3.8</b>	<b>Conclusions</b>	<b>70</b>
<b>CHAPTER 4. Structure-Property Relationship For LC<sup>3</sup> Rheology</b>		<b>73</b>
<b>4.1</b>	<b>Introduction</b>	<b>73</b>
<b>4.2</b>	<b>Research Significance</b>	<b>74</b>
<b>4.3</b>	<b>Experimental</b>	<b>75</b>
4.3.1	Materials	75
4.3.2	Mix design	75
4.3.3	Tests and Analytical Methods	77
<b>4.4</b>	<b>Computational Methods</b>	<b>79</b>
4.4.1	Machine learning approach	79
4.4.2	Kernel smoothing for isothermal calorimetry data	83
<b>4.5</b>	<b>Results and Discussion</b>	<b>86</b>
4.5.1	Composition- rheology linkages	87
4.5.2	Statistical Analysis and Modelling Results	99
4.5.3	Relationship between heat release and yield stress	101
<b>4.6</b>	<b>Conclusions</b>	<b>107</b>
<b>CHAPTER 5. Relating LC<sup>3</sup> Microstructure, Surface Resistivity and Compressive Strength Development</b>		<b>110</b>
<b>5.1</b>	<b>Introduction</b>	<b>110</b>
<b>5.2</b>	<b>Research Significance</b>	<b>112</b>
<b>5.3</b>	<b>Experimental</b>	<b>113</b>
5.3.1	Materials	113
5.3.2	Mix Design	113
5.3.3	Analytical Methods	114
5.3.4	Testing	115
<b>5.4</b>	<b>Results</b>	<b>120</b>
5.4.1	Influence of PC:MK:LS	121
5.4.2	Influence of limestone particle size	125
5.4.3	Influence of added gypsum content	129
<b>5.5</b>	<b>Discussion</b>	<b>133</b>
5.5.1	Formation Factor	133
5.5.2	Linking portlandite consumption and bound water evolution to surface resistivity and strength development	136
5.5.3	Compressive strength vs. Surface Resistivity	139
<b>5.6</b>	<b>Conclusions</b>	<b>141</b>
<b>CHAPTER 6. Multi-Objective Design of LC<sup>3</sup>: Sustainability and Strength</b>		<b>144</b>
<b>6.1</b>	<b>Introduction</b>	<b>144</b>
<b>6.2</b>	<b>Research Significance</b>	<b>146</b>
<b>6.3</b>	<b>Methodology</b>	<b>146</b>
6.3.1	Mix Design	147

6.3.2	Analytical and Test Methods	149
6.3.3	Sustainability Analysis	150
6.3.4	Statistical methods	152
6.3.5	Multi-Objective Optimization	152
<b>6.4</b>	<b>Results and Discussion</b>	<b>153</b>
6.4.1	Assessment of Sustainability	153
6.4.2	Compressive Strength	154
6.4.3	Strength vs. Sustainability	157
6.4.4	Significance of Limestone Characteristics on Heat Evolution	160
6.4.5	Statistical Analysis	161
6.4.6	Multi-Objective Optimization	163
<b>6.5</b>	<b>Conclusions</b>	<b>167</b>
<b>CHAPTER 7.</b>	<b>Conclusions and Recommendations</b>	<b>169</b>
<b>7.1</b>	<b>Summary of Findings</b>	<b>169</b>
<b>7.2</b>	<b>Recommendations for Practice</b>	<b>171</b>
<b>7.3</b>	<b>Recommendations for Future Research</b>	<b>173</b>
<b>REFERENCES</b>		<b>175</b>

## LIST OF TABLES

Table 3.1 - D <sub>50</sub> , specific surface area (SSA) and specific gravity of raw materials .....	37
Table 3.2 - Oxide and phase composition of the materials .....	37
Table 3.3 - Experimental matrix based on mass ratio for isothermal calorimetry .....	38
Table 3.4 - Heat flow parameters of LC <sup>3</sup> pastes including L15 influenced by metakaolin fraction (w/s = 0.40, 0.55, 0.60, 0.65, 0.75, SP = 0%, 0.5%, added gypsum content = 2%) .....	49
Table 3.5 - Heat flow parameters of LC <sup>3</sup> pastes influenced by limestone particle size (w/s = 0.40, 0.75, SP = 0%, 0.5%, added gypsum content = 2%) .....	53
Table 3.6 - Heat flow parameters of the 55:30:15 pastes including L15 influenced by added gypsum content (w/s = 0.75, SP = 0%) .....	55
Table 3.7 - Heat flow parameters of LC <sup>3</sup> pastes including L15 influenced by w/s (without SP, added gypsum content = 2%) .....	58
Table 3.8 - Heat flow parameters of the LC <sup>3</sup> pastes including L15 influenced by SP content (w/s = 0.55, SP = 0%, added gypsum content = 2%) .....	61
Table 3.9 - The stepwise regression model variables, standardized coefficients, and p-values for the sulfate balance ( $R^2 = 0.811$ and RMSE = 0.841 h) .....	70
Table 3.10 - The stepwise regression model variables, standardized coefficients, and p-values for the cumulative heat evolved by 24 h ( $R^2 = 0.907$ , RMSE = 2.877 J/g) .....	70
Table 4.1 - Experimental matrix .....	77
Table 4.2 - Packing indexes (K) calculated for LC <sup>3</sup> pastes with varying PC:MK:LS at different w/s ratios. ....	92
Table 4.3 - Packing indexes (K) calculated for LC <sup>3</sup> pastes influenced by PC:MK:LS and limestone particle size at constant w/s of 0.75 .....	96
Table 4.4 - The selected model variables, standardized coefficients, and p-values for yield stress .....	101
Table 4.5 - The selected model variables, standardized coefficients, and p-values for plastic viscosity .....	101
Table 5.1 - Experimental matrix, showing binder content by mass fraction and superplasticizer content by weight of solids (PC+Metakaolin+Limestone+Gypsum). ..	114



Table 5.2 - The degree of hydration inputs assumed for each LC <sup>3</sup> formulation based on [48]. Effects of limestone fineness and gypsum dosage on the degree of hydration were assumed as negligible. ....	120
Table 5.3 - Percentage (%) change in surface resistivity and compressive strength of LC <sup>3</sup> mixtures with varying PC:MK:LS between 3 and 7 days and 7 and 28 days.....	125
Table 5.4 - Percentage (%) change in surface resistivity and compressive strength of LC <sup>3</sup> mixtures with varying limestone particle size between 3 and 7 days and 7 and 28 days. ....	129
Table 5.5 - Percentage (%) change in surface resistivity and compressive strength of LC <sup>3</sup> mixtures with varying added gypsum content between 3 and 7 days and 7 and 28 days. ....	133
Table 5.6 - Estimated formation factor (unitless) of LC <sup>3</sup> formulations.....	136
Table 6.1 - Experimental matrix by sample identifier, based on mass ratio.....	149
Table 6.2 - GWP (kg CO <sub>2</sub> e/t) of the raw materials used to produce LC <sup>3</sup> cement .....	152
Table 6.3 - The model variables, standardized coefficients, and p-values .....	162
Table 6.4 - Constraints on the minimum and maximum fractions of each LC <sup>3</sup> component (for w/s = 0.40), considering LS particle size.....	163
Table 6.5 - Compressive strength and GWP of the selected LC <sup>3</sup> compositions from the Pareto front.....	166

## LIST OF FIGURES

Figure 1.1 – Global distribution of common clay minerals (Adapted from [14]) .....	4
Figure 1.2 - Varying $^{27}\text{Al}$ NMR spectra of kaolinite with respect to calcination temperature (From [23]) .....	6
Figure 1.3 – A schematic illustrating the research approach and objectives. Composition-property relationships are constructed separately for the sulfate balance, rheology, compressive strength, and durability (assessed by only surface resistivity). Also, the influence of sulfate balance on rheology, strength and durability are explored. ....	10
Figure 2.1 – Scanning electron microscopy image for kaolinite (From [39]) .....	13
Figure 2.2 – Atomic structure of kaolinite (From [39]).....	14
Figure 2.3 - Illustration of the filler effect in cementitious systems (From [56]). ....	19
Figure 2.4 - Original strength-SO <sub>3</sub> -porosity graphic for white Portland cement (From [59]).....	21
Figure 2.5 – Zeta potential according to electrical double layer model.....	29
Figure 2.6 - Interparticle potential energy curves for PC showing the significance of the zeta potential to achieve dispersion in the cement suspensions [79, 82]. ....	29
Figure 3.1 - Particle size distribution of materials used.....	36
Figure 3.2 - The time of max. of silicate peak and the sulfate depletion point determined by NW Kernel estimate.....	45
Figure 3.3 - Heat evolution of LC <sup>3</sup> pastes during first 24 h influenced by metakaolin fraction (w/s = 0.75, SP = 0%, added gypsum content = 2%): (a) constant limestone particle size (L15) used in each mix, (b) the 55:30:15 paste includes L15 while the pastes 55:22.5:22.5 and 55:15:30 include L3).....	48
Figure 3.4 - Heat evolution of the 55:30:15 pastes during first 24 h influenced by limestone particle size (w/s = 0.75, without SP, added gypsum content = 2%) .....	52
Figure 3.5 - Heat evolution of the 55:30:15 pastes including L15 during first 24 h influenced by added gypsum content (w/s = 0.75, without SP). First 48 h of hydration was given in this figure to show the full shape of the alumina peak observed in 5% added gypsum paste.....	55
Figure 3.6 - Heat evolution of the 55:30:15 pastes including L15 during first 24 h influenced by w/s (without SP, added gypsum content = 2%) .....	58

Figure 3.7 - Heat evolution of the 55:30:15 pastes including L15 during first 24 h influenced by SP content (w/s = 0.55, added gypsum content = 2%) .....	61
Figure 3.8 – Relationship between the slope of silicate peak and sulfate depletion point with and without superplasticizer for LC <sup>3</sup> pastes including constant added gypsum content 2%. .....	63
Figure 3.9 - Evolution of hydrated phases identified in the 55:22.5:22.5 pastes including L3 by in-situ XRD: (a) 0% added gypsum, (b) 5% added gypsum. These pastes were prepared at w/s of 0.4 and contain 0.5% superplasticizer by mass of solid.....	65
Figure 3.10 – Heat evolution and in-situ XRD results of the 55:22.5:22.5 pastes including L3: (a) 0% added gypsum, (b) 5% added gypsum. These pastes were prepared at w/s of 0.4 and contain 0.5% superplasticizer by mass of solid. ....	66
Figure 3.11 - The derivative of the heat evolution curve and in-situ XRD results of the 55:22.5:22.5 paste including L3 without added gypsum. ....	68
Figure 4.1 - Illustration of the Nadaraya-Watson kernel estimate used to predict the heat flow parameters for 55:22.5:22.5-0.75-L3-G2 such as rate of heat release during the induction period. Top figure shows the predicted heat flow, and the bottom figure shows the time derivative of the heat flow. ....	86
Figure 4.2 - Relationship between the solid volume concentration and the yield stress (a) and plastic viscosity (b) of LC <sup>3</sup> formulations. Varying PC:MK:LS and limestone particle sizes are represented with different colors and marker styles. The influence of the added gypsum content on the yield stress and plastic viscosity of 55:30:15 including L15 is indicated by the red dashed circle. ....	89
Figure 4.3 - Influence of the metakaolin fraction on the yield stress (a), and plastic viscosity (b) of LC <sup>3</sup> pastes at different w/s ratios. Limestone particle size (L15) and added gypsum content (2% by mass of total solid) are constant in these pastes. Error bars indicate one standard deviation measured for each formulation. ....	91
Figure 4.4 - Influence of the limestone particle size on the yield stress (a) and plastic viscosity (b) of LC <sup>3</sup> pastes with varying PC:MK:LS. These pastes were prepared at constant w/s of 0.75. Error bars indicate one standard deviation measured for each formulation.....	95
Figure 4.5 - Influence of the added gypsum content on the yield stress (a) and plastic viscosity (b) of 55:30:15 including L15. These pastes were prepared at constant w/s of 0.75. Error bars indicate one standard deviation measured for each formulation. ....	98
Figure 4.6 - (a) Influence of the PC:MK:LS on the onset heat of pastes including L15 and 2% added gypsum; (b) Influence of the limestone particle size on the onset heat of pastes with varying PC:MK:LS at w/s of 0.75; (c) Influence of the added gypsum content on the onset heat of 55:30:15 pastes including L15. Error bars indicate one standard deviation calculated for each formulation. ....	105

Figure 4.7 - Relationship between the estimated TPD and the onset heat for all pastes examined. ....	105
Figure 4.8 – Correlation between the onset heat and yield stress .....	107
Figure 5.1 - DTG and mass loss of LC <sup>3</sup> at 28 days of hydration influenced by PC:MK:LS. ....	122
Figure 5.2 - Surface resistivity development of LC <sup>3</sup> mixtures influenced by PC:MK:LS. Inset shows the results until 7 days of hydration. ....	123
Figure 5.3 - Compressive strength development of LC <sup>3</sup> mixtures influenced by mixture proportioning.....	125
Figure 5.4 - DTG and mass loss of LC <sup>3</sup> at 28 days of hydration influenced by limestone particle size. ....	126
Figure 5.5 - Surface resistivity development of LC <sup>3</sup> mixtures influenced by limestone particle size. ....	127
Figure 5.6 - Compressive strength development of LC <sup>3</sup> mixtures influenced by limestone particle size. ....	129
Figure 5.7 - DTG and mass loss of LC <sup>3</sup> at 28 days of hydration influenced by gypsum dosage. ....	130
Figure 5.8 - Surface resistivity development of LC <sup>3</sup> mixtures influenced by gypsum dosage. ....	131
Figure 5.9 - Compressive strength development of LC3 mixtures influenced by gypsum dosage. ....	133
Figure 5.10 - (a) Relationship between bound water (measured by TGA) and compressive strength, (b) Relationship between portlandite content and compressive strength. The blue dotted line represents the linear trendlines fitted to the data. ....	138
Figure 5.11 - (a) Relationship between bound water (measured by TGA) and surface resistivity, (b) Relationship between portlandite content and surface resistivity. In both figures y-axis represents the natural logarithm (ln) of the surface resistivity. The blue dotted line represents the linear trendlines fitted to the data. ....	139
Figure 5.12 - Relationship between compressive strength development and surface resistivity at 3, 7 and 28 days of hydration. All the resistivity and strength results at 3, 7 and 28 days of hydration are included. The blue dotted line represents the logarithmic trendline fitted to the data. ....	141
Figure 6.1 - Methodology followed to obtain the optimized LC <sup>3</sup> mix designs at 3 and 56 days .....	147

Figure 6.2 - GWP potential (kg CO <sub>2</sub> e/t) of different LC <sup>3</sup> pastes investigated in laboratory. Purple bars represent the variability from various limestone sizes considered for each mix .....	154
Figure 6.3 - Compressive strength development of LC <sup>3</sup> pastes including different limestone particle sizes; (a) at 3 days of hydration, (b) 7 days of hydration, (c) 28 days of hydration, (d) 56 days of hydration. Black bars indicate the standard deviation of compressive strength, $\pm 1\sigma$ , for each mix .....	157
Figure 6.4 - Strength development vs. GWP of LC <sup>3</sup> pastes investigated; (a) at 3 days of hydration, (b) at 56 days of hydration. Kernel density estimates for each of the limestone particle sizes are shown next to top horizontal and secondary vertical axes .....	159
Figure 6.5 - The peak rate of heat release in the acceleration period (mW/g) explained by LSI.....	161
Figure 6.6 - In multi-objective optimization, there exists a ‘frontier’ of optimal solutions. From this there is an inherent trade-off shown where the maximization of one output leads to a lower value in the other. (a) Shows this Pareto front for the 3-day strength while (b) plots this front for the 56-day strength .....	165

# LIST OF SYMBOLS AND ABBREVIATIONS

## Abbreviations

AASHTO	American Association of State Highway and Transportation Officials
ACM	Alternative Cementitious Material
ASR	Alkali-Silica Reaction
ASTM	American Society for Testing and Materials
DTG	Differential Thermogravimetry
EDS	Energy Dispersive Spectroscopy
GHG	Greenhouse Gas Emissions
GWP	Global Warming Potential
LC <sup>3</sup>	Limestone Calcined Clay Cements
LCA	Life Cycle Assessment
LS	Limestone
ML	Machine Learning
MK	Metakaolin
NMR	Nuclear Magnetic Resonance
NW	Nadaraya-Watson
NIST	National Institute of Standards and Technology
O	Octahedral Sheet
PC	Portland Cement
RILEM	The International Union of Laboratories and Experts in Construction Materials, Systems and Structures
RMSE	Root Mean Squared Error
SCM	Supplementary Cementitious Material

SEM	Scanning Electron Microscopy
SP	Superplasticizer
SR	Surface Resistivity
SSA	Specific Surface Area
PPM	Parts per Million
T	Tetrahedral Sheet
TGA	Thermogravimetric Analysis
XRD	X-ray Diffraction
XRF	X-ray Fluorescence

### **Cement Chemistry Notations and Abbreviations**

A	Aluminum Oxide ( $\text{Al}_2\text{O}_3$ )
AFm	$\text{Al}_2\text{O}_3\text{-Fe}_2\text{O}_3$ (mono)
AFt	$\text{Al}_2\text{O}_3\text{-Fe}_2\text{O}_3$ (tri)
C	Calcium Oxide ( $\text{CaO}$ )
$\hat{\text{C}}$	Carbon Dioxide ( $\text{CO}_2$ )
$\text{C}_3\text{A}$	Tricalcium Aluminate ( $3\text{CaO}.\text{Al}_2\text{O}_3$ )
$\text{C}\hat{\text{C}}$	Calcium Carbonate ( $\text{CaO}.\text{CO}_2$ )
$\text{C}_3\text{A}.\text{C}\hat{\text{C}}.\text{H}_{11}$	Monocarboaluminate ( $3\text{CaO}.\text{Al}_2\text{O}_3.\text{CaO}.\text{CO}_2.11\text{H}_2\text{O}$ )
$\text{C}_3\text{A}.\text{C}\hat{\text{C}}_{0.5}.\text{H}_{12}$	Hemicarboaluminate ( $3\text{CaO}.\text{Al}_2\text{O}_3.\text{CaO}.0.5\text{CO}_2.12\text{H}_2\text{O}$ )
$\text{C}_4\text{AF}$	Tetracalcium Aluminoferrite ( $4\text{CaO}.\text{Al}_2\text{O}_3.\text{Fe}_2\text{O}_3$ )
CH	Calcium Hydroxide ( $\text{Ca}(\text{OH})_2$ )
$\text{C}_2\text{S}$	Dicalcium Silicate ( $2\text{CaO}.\text{SiO}_2$ )
$\text{C}_3\text{S}$	Tricalcium Silicate ( $3\text{CaO}.\text{SiO}_2$ )
$\text{C}\$$	Anhydrite ( $\text{CaO}.\text{SO}_3$ )

C-(A)-S-H	Calcium-Alumino-Silicate-Hydrate
C-S-H	Calcium-Silicate-Hydrate
H	Water (H <sub>2</sub> O)
S	Silicon Dioxide (SiO <sub>2</sub> )
\$	Sulfur trioxide (SO <sub>3</sub> )

### **Symbols**

$\pi$	Pi mathematical constant
$\varepsilon$	Relative dielectric constant of the medium
$\varepsilon_0$	Permittivity of fress space
$r$	Particle Radius
$\varphi$	Zeta Potential
$K$	Debye-Huckel Parameter
$h$	Interparticle Distance
D <sub>10</sub>	10 <sup>th</sup> Percentile Particle Diameter
D <sub>50</sub>	50 <sup>th</sup> Percentile Particle Diameter
D <sub>90</sub>	90 <sup>th</sup> Percentile Particle Diameter
$\Phi$	Solid Volume Concentration
w/b	Water-to-Binder Mass Ratio
w/s	Water-to-Solid Mass Ratio



## SUMMARY

Limestone calcined clay cements ( $LC^3$ ) are a broad class of blended mineral compositions that are alternatives to conventional Portland cement (PC) and are one of the most promising technologies to achieve carbon neutrality in the concrete industry. However, a mechanistic understanding of fresh and hardened properties of  $LC^3$ -based pastes, mortars, and concrete, as well as empirical design approaches are lacking. This dissertation addresses these knowledge gaps by developing composition-property linkages with the purpose of facilitating the transition of  $LC^3$  from the laboratory to practice. Specifically, the influence of  $LC^3$  composition on early hydration kinetics, rheological properties, compressive strength development and durability assessed by surface resistivity test is investigated. The compositional design space considers variations in water-to-solids ratio, proportions of constituent materials (PC, calcined clay or “metakaolin” (MK), limestone (LS)), added gypsum content, limestone particle size and superplasticizing admixture dosage. The composition-property linkages are established by combining laboratory data with data analytics approaches including Machine learning (ML).

A guiding hypothesis is that the sulfate balance (defined in this dissertation as time difference between the maximum of silicate peak and the sulfate depletion point measured during isothermal calorimetry), influences both the fresh (i.e., rheology) and hardened properties (e.g., compressive strength, surface resistivity) of  $LC^3$ . To examine this, first, a non-parametric kernel regression technique Nadaraya-Watson (NW) estimator is applied to the heat evolution curves obtained from isothermal calorimetry, allowing quantification of the influence of compositional factors on early hydration kinetics (e.g., slope of silicate peak, sulfate depletion point) in a novel way. Thereafter, linkages between composition

and sulfate balance are established first and then the hypothesis of the role of sulfate balance in influencing fresh and hardened properties of LC<sup>3</sup> is tested in further chapters. Next, to predict the rheological behavior of LC<sup>3</sup>, domain knowledge is embedded in ML in the form of five physicochemical predictors, all based on composition. The ML modeling approach helps to elucidate the diversity of mechanisms through which the MK component dominates the rheological behavior of LC<sup>3</sup>, both directly and through its interactions with the other mineral constituents. Analytical measures (e.g., changes in portlandite and bound water contents over time) show how microstructural development translates to compressive strength and surface resistivity development. For instance, LC<sup>3</sup> mortar strength over 28 days of hydration can be accurately predicted not only from its portlandite content over time, but also shows strong correlation with concrete surface resistivity development. Finally, a multi-objective optimization tool is developed to simultaneously predict LC<sup>3</sup>'s global warming potential and compressive strength development, which are two parameters central in the industrywide shift in cement compositions. Overall, this dissertation provides new foundational understanding of LC<sup>3</sup>'s early hydration kinetics and property evolution that supports the concrete industry's adaptation to LC<sup>3</sup>; this work provides insights that not only rely on empirical findings but also generates models and analytical techniques that can be used to accurately predict fresh and hardened properties based on LC<sup>3</sup> composition.

# CHAPTER 1. INTRODUCTION

## 1.1 Background

In retrospect, concrete has advanced human civilization by enabling construction of key components of global infrastructure during the last century such as dams, bridges, and residential buildings. Therefore, it has become the most important and most used human-made material on Earth, serving the needs of humankind [1]. However, concrete production is also a destructive process in our planet and a culprit behind the climate change. Because, 7-9% global anthropogenic carbon dioxide ( $\text{CO}_2$ ) equivalent greenhouse gas emissions are associated with manufacturing of one of concrete's component, cement [2, 3]. Portland cement (PC) production in 2018 was  $\sim 4.1$  Gt [4], with 86.6 million tons in United States, and estimated to increase to  $\sim 4.7$  Gt by 2050 when population on Earth is expected to grow up to almost 10 billion people [5]. In other words, a “game changer” is needed in the cement industry to curb the  $\text{CO}_2$  emissions associated with its production while providing construction technologies for increasing urbanization. Such a transformation in the cement industry towards sustainability would allow exploitation of concrete's everlasting benefits to humanity without endangering the environment.

During the production of PC clinker at kiln temperatures higher than  $1400^\circ\text{C}$ , between 0.85 and 0.95 ton of  $\text{CO}_2$  are emitted into the atmosphere per ton of PC [6]. This is due to the calcination process, i.e., thermal treatment that leads to a chemical decomposition, during which limestone ( $\text{CaCO}_3$ ) is decomposed into calcium oxide ( $\text{CaO}$ ) and  $\text{CO}_2$ . Hence, the  $\text{CO}_2$  released into the atmosphere comes both from the chemical reaction that occurs in the cement kiln, and from the combustion of fossil fuels needed to

reach the high temperature. Accordingly, research is focused on using alternative fuels and carbon capture to drive the production process of cement clinker to a greener future, together with studying alternative cementitious materials (ACMs) with lower carbon footprint, which incorporate some supplementary cementitious materials (SCMs) partially substituting for PC clinker [1, 3].

SCMs are materials that can partially replace PC or fine aggregate to improve the workability, and long-term mechanical and durability properties of concrete [1, 7-9]. SCMs are finely divided siliceous or aluminosiliceous minerals that can be derived from many industries as by-products. For instance, fly ash as one of the most widely used SCMs, is a by-product of coal-combusting thermal power plants. Furthermore, other typical SCMs used in concrete industry such as blast furnace slag (BFS) and silica fume are by-products of pig iron and ferrosilicon production, respectively.

Partially replacing PC clinker with SCMs is a recognized strategy to reduce CO<sub>2</sub> emissions that has been documented by many institutions [10, 11]. For instance, partially substituting fly ash for PC clinker is one of the cost-beneficial sustainable approaches in the global greenhouse gas abatement curve for 2030 [11]. Concurrently, it is expected that by 2030 the industrial waste generation will increase by more than 2.5 times [12], causing environmental pollution. Hence, identifying an ACM that can also incorporate SCMs or industrial waste materials would have the double effect of contributing to the management of industrial waste and providing an additional solution for a greener concrete industry. However, despite being low-cost alternatives, fly ash and blast furnace slag feedstock may not meet the demand by concrete industry in the long term. On the one hand, the abundance of fly ash is threatened in many countries, including U.S., by the recent plans of retiring

the existing coal-fired plants [8]. On the other hand, slag abundancy worldwide was reported as ~10% of the total cement produced and is not projected to increase towards being a sustainable SCM for cement production [13]. To design and adapt an ACM, which is more environmentally friendly than PC in the long run, limestone calcined clay cements (LC<sup>3</sup>) emerged as a promising technology. This attention is largely due to its mixture formulation, which incorporates widely abundant SCMs, clay and limestone, and its satisfactory performance in laboratory [13]. Among common clay minerals, kaolinitic clays – common in humid equatorial and subtropical regions (Figure 1.1) [13, 14] -, has been selected to produce LC<sup>3</sup> because of its capability to transform a highly reactive material called “metakaolin” upon calcination [15].

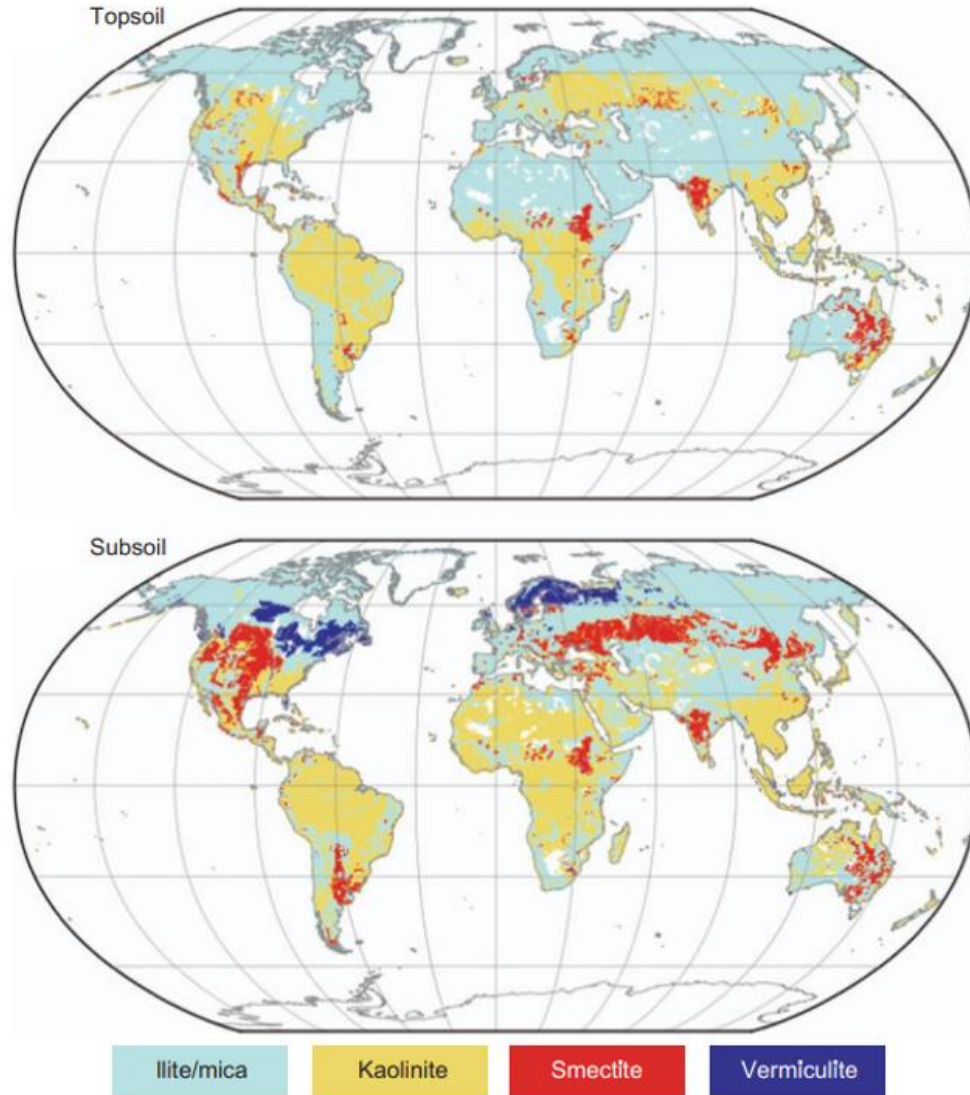


**Figure 1.1 – Global distribution of common clay minerals (Adapted from [14])**

## **1.2 Motivation and Problem Statement**

Several studies have explored the limestone-blended ternary cements as well as PC-limestone and PC-calcined clay binary binders that ushered in the advent of LC<sup>3</sup> with potentially fewer CO<sub>2</sub> emissions than PC [13, 16]. LC<sup>3</sup> is proposed as a sustainable alternative to PC because it partially replaces PC with SCMs that are abundant on earth, such as clay (used after calcined), and limestone [13]. A typical LC<sup>3</sup> formulation consists of 50% PC clinker, 30% calcined clay, 15% limestone, and 5% gypsum, by mass; though,

these proportions may vary. It promises 30% reduction in CO<sub>2</sub> emissions compared to PC, mainly due to lower PC clinker content in its formulation [16].

Thermal treatment (calcination) is necessary to produce calcined clay, which is usually carried out between 600 °C and 800 °C [13, 15, 17]. Typically, kaolinitic clays are sourced for producing LC<sup>3</sup> because kaolinite transforms to a highly reactive aluminosilicate material called calcined kaolinite or mostly “metakaolin” upon calcination [15, 17]. This reactivity of metakaolin originates from the 5-coordinated Al groups that manifests post-calcination (Figure 1.2) associated with the removal of the hydroxyl groups creating a disordered structure [15, 18]. Clay calcination can be realized with either a traditional rotary kiln – also used for PC production - or a flash calciner [18, 19]. Also, metakaolin is considered a very fine material in the concrete industry because the median particle diameter of PC is usually 10 times coarser than that of the metakaolin [20]. Owing to its great fineness and chemical reactivity, incorporation of metakaolin into concrete leads to denser microstructures and thus can improve the hardened properties of concrete such as compressive strength [20, 21]. However, metakaolin is an expensive material - can be as 5 times costly than PC - resulting from its processing and high demand by many industries despite limited availability [13, 17, 22]. Therefore, dependency on high metakaolin content can drive the cost of LC<sup>3</sup> production to undesirable levels. The solution could be to use low amounts of metakaolin or impure clays without compromising performance.

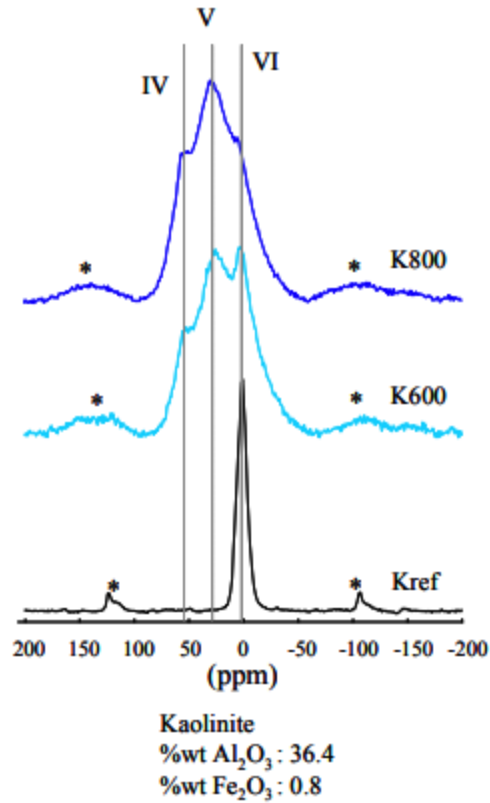


**Figure 1.2 - Varying  $^{27}\text{Al}$  NMR spectra of kaolinite with respect to calcination temperature (From [23])**

Limestone does not require any thermal treatment for its use in  $\text{LC}^3$ , which offsets the additional cost of calcining clay to some extent [13]. However, this does not mean that limestone requires no processing. In fact, it needs to be ground to a certain particle size distribution and fineness prior to its use in concrete, which are important variables for performance, cost, and sustainability of the binder. From an environmental and cost standpoint, incorporating relatively coarser limestone particle sizes and lower metakaolin fractions may be preferable, because this suggests less processing (i.e., less grinding required for relatively coarser limestone) needed to produce  $\text{LC}^3$ -based concrete [24]. What is critical to address here is the performance varied by these changes in the binder formulation. To illustrate, limestone can create “filler effect” (detailed in Section 2.1.2) when it is finer than PC. The filler effect can improve the packing in solid matrix and



modify the early hydration. As a result, strength development and durability may be benefited [7, 9, 25-27]. It should be noted that these beneficial impacts from fine limestone particles are mediated by their content in mixture design. Because limestone itself does not form space-filling hydration products, an excess amount of limestone is likely to reduce hydration products in a cementitious system independent of its particle size, decreasing concrete performance. Therefore, structure-property relationships, which represent the variations in the characteristics and proportioning of constituent materials, should be established to inform sustainability and performance-based mixture design with LC<sup>3</sup>. Independent of the potential modifications related to proportioning of PC, calcined clay and limestone components, proper sulfation - typically achieved by inclusion of a calcium sulfate carrier - will be the first step toward high performance.

Incorporation of a calcium sulfate carrier (i.e., gypsum) is a common practice to circumvent the undersulfation – sulfate addition less than optimal - due to the presence of calcined clay with high alumina content in LC<sup>3</sup>. The undersulfation may cause flash setting or delay in the silicate reaction, which reduces early strength (< 3 days) [28-31]. The early strength can be negatively impacted also by the oversulfation – sulfate addition more than optimal [32]. These results underline the significance of the sulfate balance toward satisfactory strength. However, an agreement could not be established between researchers as to whether alumina content of calcined clay impacts the sulfate balance of LC<sup>3</sup> [30, 31]. Further, the effects of w/s and superplasticizer content has been overlooked despite the fact that these parameters are commonly adjusted in mixture design for field applications. Reaching a complete understanding on this phenomenon is pivotal owing to great influence of sulfate content on the phase assemblage of LC<sup>3</sup> [33]. Apart from the incomplete

understanding on this phenomenon, a technical need exists in this domain to predict the sulfate balance of LC<sup>3</sup> based on a diverse set of compositional predictors not limited to variations in calcined clay characteristics.

It can be inferred that in multi-component cementitious systems like LC<sup>3</sup>, the size, reactivity and proportioning of constituent materials interplay a role for the property evolution, amplifying the difficulty of establishing the structure-property relationships. While many published studies investigated the properties of LC<sup>3</sup>, clear understanding of the structure-property linkages arising from the complex binder chemistry of LC<sup>3</sup> remain poorly defined. To contribute to the design guidance of LC<sup>3</sup> and facilitate its deployment, it is of paramount importance that property evolution of this binder is well understood based on its composition – used interchangeably with the word “structure”. In this dissertation, the properties of interest span the early hydration kinetics including sulfate balance, rheology, compressive strength development, and durability assessed by surface resistivity. The compositional space, on the other hand, considers variations in the constituent materials ratio (PC:MK:LS) and characteristics (i.e., limestone particle size), extra gypsum dosage, w/s, and superplasticizer content, which are understood to be the main design parameters of LC<sup>3</sup> based on the literature.

### **1.3 Objectives: Data Analytics Guided Design of LC<sup>3</sup>**

The ability to predict fresh and hardened properties is crucial for transitioning LC<sup>3</sup> from the laboratory into field placements. However, in contrast with the PC concrete where decades of data and experience relate compositional and environmental parameters to performance, empirical design approaches for LC<sup>3</sup> are lacking. By combining laboratory

data with data analytics approaches, this research aims to build composition-property linkages for sulfate balance, rheology, strength development and durability as illustrated in Figure 1.3.

It is hypothesized that the sulfate balance can significantly influence both the fresh and hardened properties such as rheology, strength and surface resistivity development given the synergy between the sulfate content and phase assemblage of LC<sup>3</sup> [33]. Therefore, the sulfate balance of LC<sup>3</sup> is addressed first in this research. Thereafter, to include the effects of sulfate balance in composition-property linkages for rheology, strength, and surface resistivity the composition is consistently varied by added gypsum content in the experimental matrix of these studies in addition to other variables such as PC:MK:LS and limestone particle size. Presumably, the empirical and analytical findings of this research can serve as an optimization basis towards globalization of LC<sup>3</sup> formulations, using regional materials, to achieve desired performance, and to facilitate the adaptation by industry of this emerging sustainable binder. Accordingly, the specific research aims are as follows:

- 1) Establish a methodology to quantify the early hydration kinetics (e.g., sulfate balance) and understand the relative importance of the compositional factors.
- 2) Identify significant system variables and develop predictive models for LC<sup>3</sup> rheology.
- 3) Understand the relationship between hydration kinetics and yield stress of paste.
- 4) Understand the influence of microstructural development on LC<sup>3</sup> compressive strength and surface resistivity development.

- 5) Explore the relationship between compressive strength and surface resistivity.
- 6) Develop a multi-objective design tool, which can optimize the performance and sustainability.

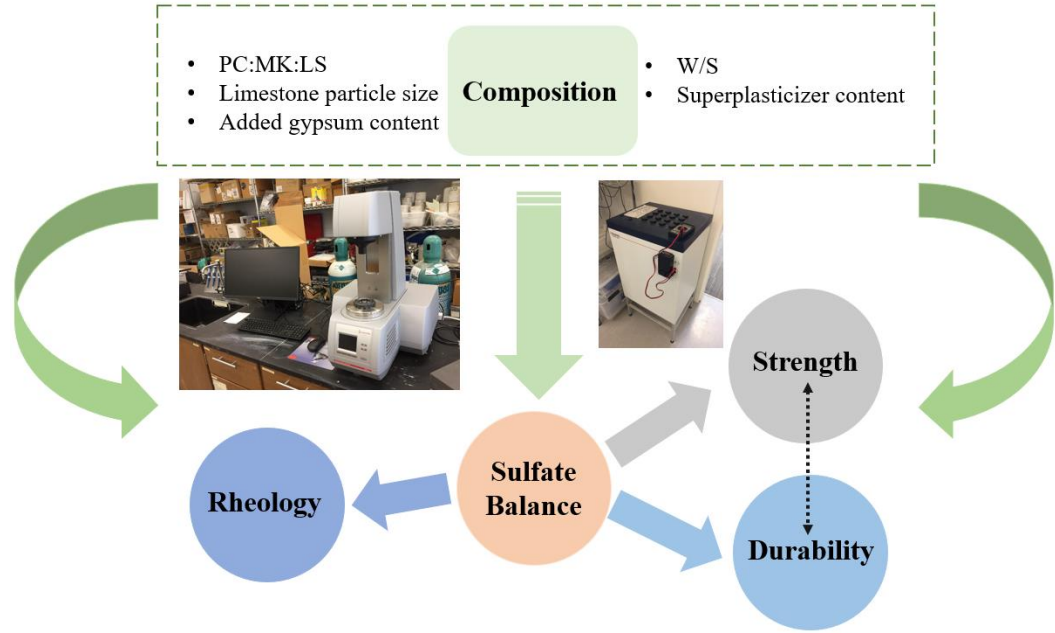


**Figure 1.3 – A schematic illustrating the research approach and objectives. Composition-property relationships are constructed separately for the sulfate balance, rheology, compressive strength, and durability (assessed by only surface resistivity). Also, the influence of sulfate balance on rheology, strength and durability are explored.**

## 1.4 Thesis Organization

This dissertation consists of seven chapters. First chapter is the introduction, which introduces the background, motivation, and research objectives. In Chapter 2, seminal works regarding LC<sup>3</sup> are critically reviewed. This chapter is divided to microstructural concepts, which will be discussed in further results sections, and the fresh and hardened properties of interest in this research. Chapter 3 investigates the sulfate balance of LC<sup>3</sup> and presents a methodology based on Kernel smoothing to parametrize the heat flow curves. This methodology is also used in Chapter 4, which examines the composition-rheology and

kinetics-rheology linkages. Further, a Machine learning model is introduced in this chapter to make predictions for LC<sup>3</sup>'s yield stress and plastic viscosity. The influence of microstructural development on strength and surface resistivity is given in Chapter 5, which also explores the relationship between resistivity and strength development. Chapter 6 demonstrates a proof-of-concept multi-objective design tool, which optimizes LC<sup>3</sup> formulations with respect to strength and global warming potential. Finally, the main conclusions and recommendations for future research and practices are summarized in Chapter 7.

## CHAPTER 2. LITERATURE REVIEW

First section is devoted to a background of kaolinite summarizing its physicochemical properties and atomic structure. Further sections present critical review of seminal works about LC<sup>3</sup>. Readers are also referred to some review papers published recently for additional background [8, 13, 34]. Per the focus of this dissertation on building structure-property relationships, microstructural development, and property evolution of LC<sup>3</sup> are reviewed. To dissect the microstructural development, three significant concepts are introduced as follows: carboaluminate phases, the filler effect, and sulfate optimization, respectively. These sections are followed by compressive strength development, durability, and rheological properties of LC<sup>3</sup>. Finally, the knowledge gaps and technical needs addressed in this dissertation are summarized.

### 2.1 Kaolinite

Kaolinite is one of the most abundant clay minerals on earth [14, 35]. Hydrothermal treatment or chemical weathering of aluminum silicate minerals such as feldspar are of the processes needed for its formation. For example, granitic rocks are considered as a significant kaolinite source because they abound with feldspar [36]. Kaolinite is mined in several countries such as Czech Republic, Germany, England, France, and the United States, mostly in Georgia.

Physicochemical characteristics of kaolinite can be summarized with color, shape, grain size and surface charge. Kaolinite is typically white to cream but depending on the impurities such as quartz or iron oxide, it might display different colors such as red or brown. Platelet-like (discoid) shape (Figure 2.1) was observed with kaolinite particles with an aspect ratio of approximately 10 and grain size of  $< 2 \mu\text{m}$  [37, 38]. Kaolinite is

heterogeneously charged due to negatively charged siloxane surfaces that are hydrophobic, and positively charged aluminol surfaces that are hydrophilic [38].

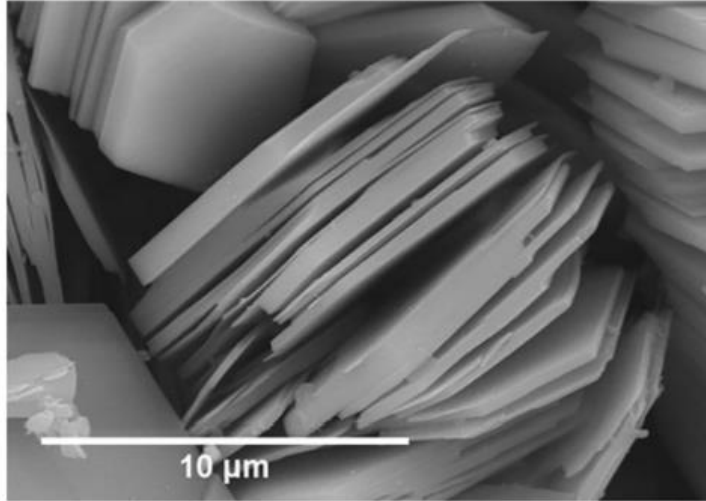


**Figure 2.1 – Scanning electron microscopy image for kaolinite (From [39])**

As a phyllosilicate mineral, kaolinite is also called a “layered silicate” due to its layered dioctahedral crystal structure with a chemical formula of  $\text{Al}_2\text{Si}_2\text{O}_5(\text{OH})_4$ . It belongs to a triclinic crystal system and is classified as a 1:1 type clay, which contains one tetrahedral sheet and one octahedral sheet (T:O), with a layer spacing of 7 Å. Aluminate and silicate groups form these layers, where the Al-incorporating octahedral sheets are bonded to Si-incorporating tetrahedral sheets by means of oxygen atoms at each tetrahedron (Figure 2.2) [15, 39].

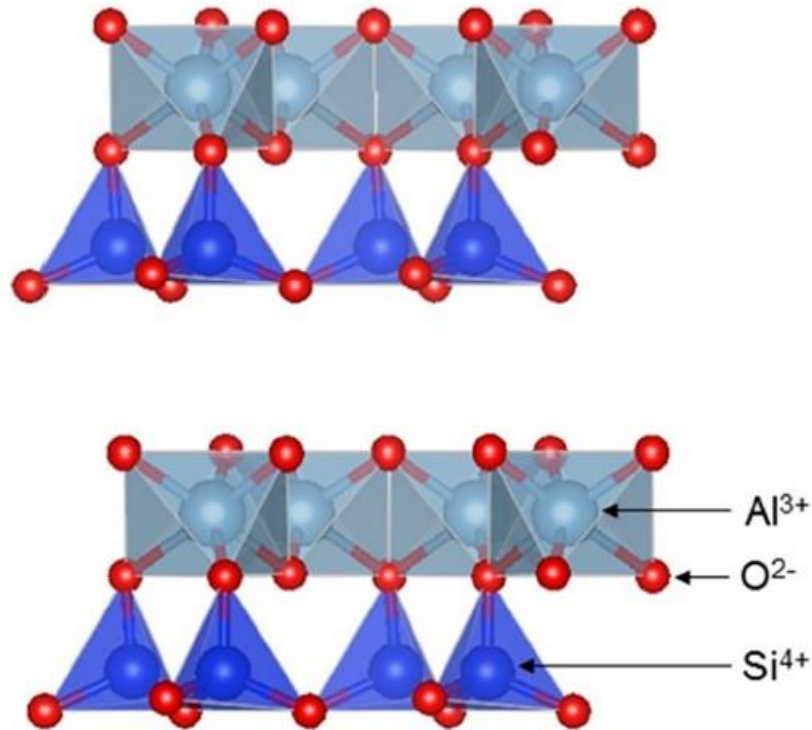


**Figure 2.2 – Atomic structure of kaolinite (From [39])**

Interlayer surface of Al-incorporating octahedral sheets also include most hydroxyl groups. These hydroxyl groups contribute to the hydrogen bonding between adjacent layers, reinforcing the dense layered structure of kaolinite [15]. Unlike some other clay minerals such as illite that contain interlayer cations to balance the electrical charge, kaolinite does not incorporate interlayer cations between the tetrahedral and octahedral sheets. Therefore, it does not carry a net electrical charge, and has a low cation exchange capacity. This lack of interlayer cations and the presence of hydrogen bonding forces between the adjacent layers consolidate the kaolinite's non-swelling nature, impeding the penetration of water between layers. Thanks to its non-swelling nature, kaolinite does not expand upon contact with water, which makes it appealing for the ceramic industry but not limited to. For example, it can be used for synthesizing zeolite [40] and as an excipient in the pharmaceutical industry [38].



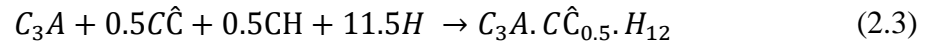
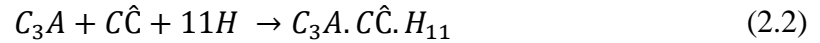
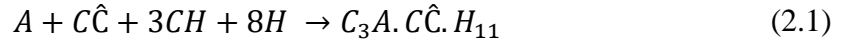
Kaolinite is an attractive material also for the concrete industry. The main reason is the capability of kaolinite to transform from a non-pozzolanic material to a pozzolanic material (called “calcined kaolinite” or “metakaolin”) after calcined between 600 and 800 °C as described in Section 1.2. Pozzolans (i.e., fly ash and silica fume) are blended with PC to improve the mechanical and durability properties of concrete. These improvements are achieved mainly in two ways: i) reaction between pozzolan and calcium hydroxide (CH) formed via PC hydration (called “pozzolanic reaction”), and ii) better particle packing in concrete matrix caused by fine pozzolan particles [7]. The former mechanism is the main motivation behind blending metakaolin with PC and limestone to produce LC<sup>3</sup> [15, 41].

## **2.2 Key Microstructural Concepts**

### *2.2.1 Virtue of LC<sup>3</sup>: Carboaluminate Phases*

As mentioned in the Section 1.2, a typical LC<sup>3</sup> formulation consists of 50% PC clinker, 30% calcined clay, 15% limestone, and 5% gypsum, by mass. This mixture design was established largely thanks to a research paper published in 2012 [41]. In this study, Antoni et al. [41] compared four PC-metakaolin-limestone ternary blends with PC substitution rates ranging from 15 to 60% by mass but with a constant metakaolin-to-limestone mass ratio (MK/LS) of 2. The mortar formulation with PC substitution range of 45% and MK/LS of 2, what has been later recognized as the typical LC<sup>3</sup> formulation, achieved ~15% higher compressive strength compared to plain PC-based mortar at 7 and 28 days of hydration. The MK/LS was selected by the authors on the basis of roughly ~50% alumina content in the oxide composition of metakaolin, which reacts with limestone – assumed as pure calcite - at 1:1 molar ratio to form 1 equivalent of monocarboaluminate (Equation 2.1). This hydrated phase not only contributes to strength by filling the empty

pores, but also stabilizes ettringite in the solid matrix by preventing its decomposition to monosulfate [42-44]. It is worth to mention that carboaluminates can also form through the reactions between limestone and calcium aluminate phases from PC (Equation 2.2 and 2.3) [33, 45]:



On the contrary, Kunther et al. [46] – by means of thermodynamic equilibrium calculations - showed that the monocarboaluminate formation can be maximized when MK/LS equals to 1. Also, as the MK/LS increased, calcite and portlandite decreased with an associated decrease of porosity filled by hydration products. Based on these studies, the MK/LS has been understood as a significant compositional representation of LC<sup>3</sup>, because it greatly impacts the phase evolution during hydration. However, further studies were still needed to elucidate the impacting factors of the carboaluminate formation given some contrary results mentioned above.

To have a better understanding on the carboaluminate formation, the influence of calcined kaolinite content in calcined clay have been studied extensively [33, 47-49]. For instance, Avet and Scrivener [48] sourced seven different calcined clays with varying calcined kaolinite contents for microstructural and strength tests. The authors found that the degree of hydration of clinker in LC<sup>3</sup> blends, containing calcined clay with  $\leq 65\%$  calcined kaolinite, could reach up to 90% at 90 days of hydration, whereas in the case of

calcined clays with > 65% calcined kaolinite, the degree of hydration did not increase beyond ~72% after 3 days due to the extensive pore refinement. This pore refinement, in other words too little pore sizes created (pore threshold radius in the order of several nanometers), suppressed the further precipitation of carboaluminate phases. In addition, Rietveld quantification displayed increasing total hemicarboaluminate and monocarboaluminate content up to 50% calcined kaolinite but decreasing beyond this level. At the same year, Maraghechi et al. [49] confirmed that the total amount of carboaluminate phases peaked at 50% calcined kaolinite. Similar to other findings mentioned previously, the authors also attributed the decreasing carboaluminate formation at > 50% calcined kaolinite to the pore refinement. Therefore, to promote carboaluminate formation, space availability in the solid matrix has been suggested as the main determinant, which could be achieved by simply increasing the w/b [33, 50].

The significance of the amount of carboaluminate formed on LC<sup>3</sup> durability and strength development has been detailed in [33, 49, 51]. [49] showed that the chloride binding of LC<sup>3</sup> was directly correlated to the amount of carboaluminates formed, important finding for corrosion resistance. On the other hand, the compressive strength development between 2 and 3 days of hydration was attributed to the nucleation of carboaluminates [33]. Beneficial impact of carboaluminates on strength was supported by also a numerical model established in [51]. In particular, the authors suggested using high metakaolin contents with low PC replacement levels, and low metakaolin contents with high PC replacement levels to achieve optimum carboaluminate formation.

Based on these studies, it is deduced that the strength development and durability can be improved by carboaluminates whose rate of formation can be tuned by the

metakaolin fraction in the mixture formulation. However, it should be kept in mind that accelerated capillary porosity refinement by increasing metakaolin fraction can impede the further precipitation of carboaluminates due to increasing saturation index beyond 3 days of hydration [48, 50]. In other words, mechanisms underlying relatively short ( $\leq 7$  days) and long-term performance ( $> 7$  days) of LC<sup>3</sup> are different, which add complexity to the structure-property linkages.

### 2.2.2 *The Filler Effect*

Scientific literature abounds with both the experimental and modelling studies examining the filler effect of SCMs [25, 30, 43, 52-55]. This phenomenon refers to substantial improvements achieved in the particle packing of cementitious materials by the inclusion of fine SCM particles [9, 26] as a partial replacement of relatively coarser PC (illustrated in Figure 2.3c and d). The filler effect is not limited to modifications in the particle packing, but it also bifurcates into the nucleation (Figure 2.3d and f) and dilution effects (Figure 2.3e and f). The nucleation effect means accelerated hydration reactions due to the additional surfaces provided by fine SCM particles. Some changes in the hydration kinetics originating from the replacement rate of PC by SCMs are known as the dilution effect. An example of this is the higher degree of hydration of clinker achieved when PC is replaced by SCMs at constant w/s, because more water would be percolating in concrete to hydrate the clinker particles [9, 26]. The filler effect can be created not only by the chemically “reactive” SCMs but also by some “inert” materials such as quartz depending on their particle size [25]. Because LC<sup>3</sup> incorporates metakaolin and limestone as the SCMs, the following discussion is centered on the filler effect of these two materials on LC<sup>3</sup> properties.

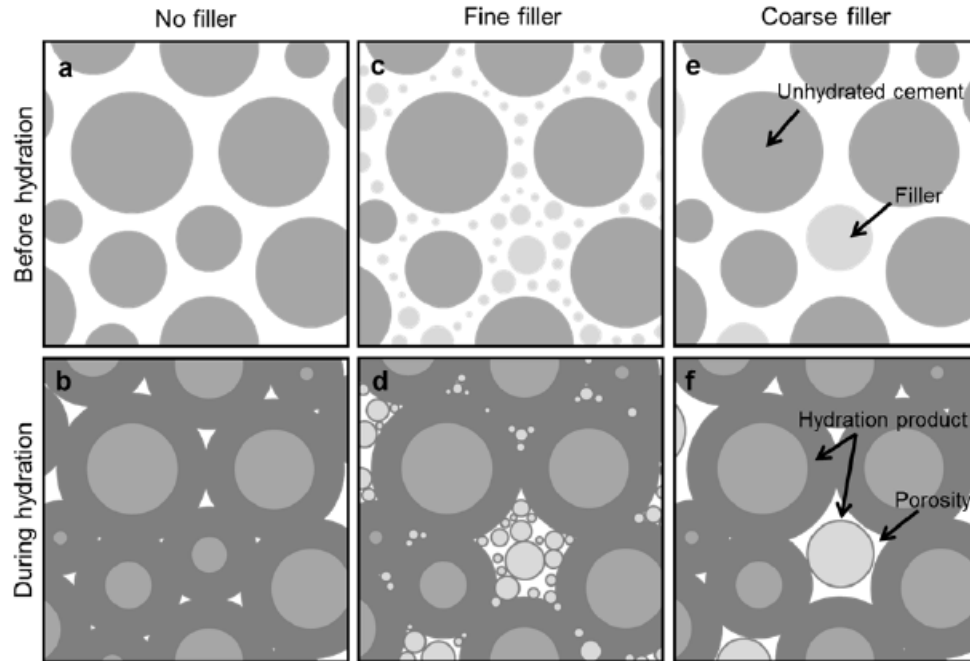


**Figure 2.3 - Illustration of the filler effect in cementitious systems (From [56]).**

The filler effect has proven to influence the sulfate requirement of  $LC^3$  [30]. The finer the calcined clay or limestone the faster the hydration reactions due to the filler effect, leading to a faster depletion of sulfate. Therefore, extra calcium sulfate source (i.e., gypsum) added into  $LC^3$  systems should be optimized accordingly so that the alumina reaction cannot delay the silicate reaction thus decrease the early strength [28]. In particular the filler effect of limestone was found more significant in this context compared to calcined clay because calcined clay particles tend to agglomerate [57].

Decoupling the significance of the filler effect for the sulfate requirement of  $LC^3$  is noteworthy because the influence of sulfate balance prevails among phase assemblage, porosity, and strength development of cementitious materials, as detailed in the next section. Apart from this relation between the filler effect and sulfate requirement, some studies showed that early compressive strength ( $\leq 3$  days) benefited from the filler effect by limestone [58]. However, no data investigating the role of the filler effect for  $LC^3$

durability exists in the literature. Further, none of the studies published in the literature quantified the importance of the filler effect relative to other impactful parameters such as the MK/LS or sulfate content in terms of flowability or strength. This quantification can be a meaningful contribution to the literature, especially from an engineer perspective, as the filler effect means finely ground materials and thus more energy requirements to produce LC<sup>3</sup>.

### 2.2.3 *Sulfate optimization*

Impact of sulfates on the properties of cementitious systems can be evaluated in the context of early C<sub>3</sub>A reaction, and C-S-H morphology. The principal function of gypsum – commonly used calcium sulfate carrier - in cementitious systems is to avoid flash set by controlling the rapid reaction of C<sub>3</sub>A, resulting in ettringite formation. Subsequently, when gypsum is depleted by participating in the hydration reactions, the sulfate concentration in the pore solution drops up to 60 times, and C-S-H morphology changes from divergent needles to an agglomerated structure [59]. Thereafter, sulfate ions desorb from C-S-H, followed by an increase in aluminum concentration, resulting in the precipitation of AFm phases such as monosulfoaluminate phases together with AFt phases such as ettringite [31]. However, adding extra gypsum more than required may decrease the degree of hydration of aluminate and alite phases, and increase the volume of capillary pores. Consequently, compressive strength diminishes as shown in Figure 2.4 for white Portland cement systems [59].

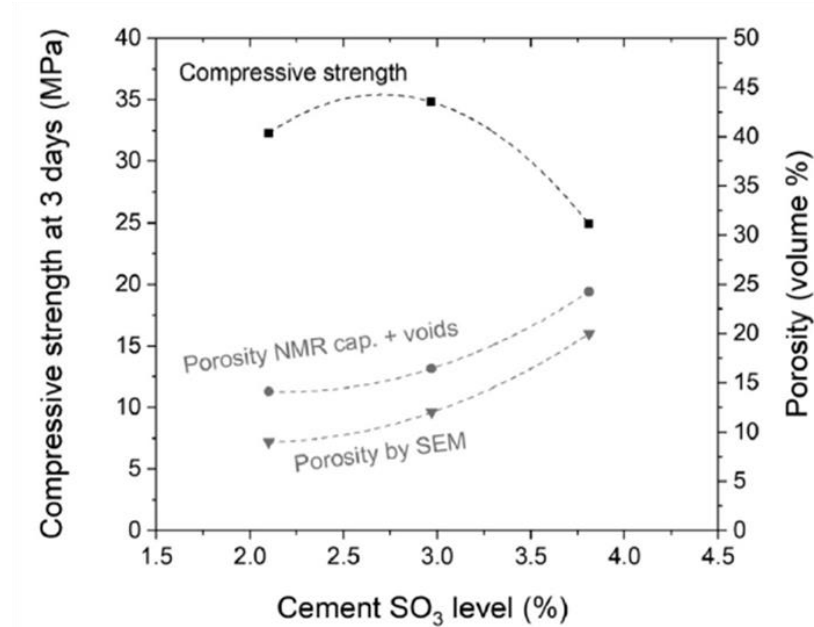


**Figure 2.4 - Original strength-SO<sub>3</sub>-porosity graphic for white Portland cement (From [59]).**

Sulfate optimization has been considered as a necessary step in designing LC<sup>3</sup> formulations due to its significance for early hydration kinetics and phase evolution [30, 33, 41]. Effect of increasing gypsum on the phase evolution of typical LC<sup>3</sup> formulation was studied systematically in [33]. The results showed increasing ettringite but decreasing portlandite and carboaluminate phases with increasing gypsum content. Similar trends were observed also in [32] but with hemihydrate used as the calcium sulfate source instead of gypsum (calcium sulfate dihydrate). The reason ettringite increased but carboaluminates decreased with increasing gypsum content was explained by the preferred ettringite formation to carboaluminates until gypsum was totally consumed. Considering the differences in the phase assemblages (i.e., ettringite and carboaluminates) created by added gypsum content, variations in macrostructural properties such as strength development and durability also need to be examined in this regard.

However, little published data are available in the literature investigating the influence of the sulfate content on compressive strength development and durability of LC<sup>3</sup> [32, 41]. Some studies suggested that an optimum level of sulfate exists to enhance the early strength ( $\leq 3\text{d}$ ), however, an increase of strength after 7 days was unlikely to be achieved solely by the sulfate addition. In fact, increasing added gypsum resulted in a lower strength beyond 7 days compared to companion mixes that did not incorporate any extra sulfate source [32, 41]. For instance, the data from [32] showed diminishing 28-d strength of LC<sup>3</sup> with added hemihydrate, which was attributed to the increasing capillary porosity in C-(A)-S-H similar to the observation from [59] for white PC. These results imply that a competition takes place between the two factors consisting of higher ettringite formation and increasing capillary porosity in the solid matrix of LC<sup>3</sup> with increasing sulfate level. Hence, LC<sup>3</sup> strength may be mediated by the net effect resulting from these two competing phenomena. On the other hand, understanding is lacking on how sulfate content controls the resistance of LC<sup>3</sup> against common durability mechanisms (i.e., freeze-thaw and alkali silica reaction). Nevertheless, autogenous shrinkage - a dimensional stability problem that can also cause cracking - was addressed in this context in [32]. This study concluded that ettringite is a major player for autogenous shrinkage – volumetric change in concrete due to hydration - which increased with hemihydrate addition. This increase in ettringite content corresponded to higher internal crystallization pressure within the pores and therefore decreased the autogenous shrinkage compared to control mixes.

Overall, more data and in-depth analyses are required to comprehend the significance of sulfate optimization for the microstructural and macrostructural development of LC<sup>3</sup>, in particular durability. It is, therefore, crucial to first understand the impacting factors of the



sulfate demand of LC<sup>3</sup> systems so that the optimum amount of extra gypsum can be estimated toward excellent performance. As mentioned in the previous section, the filler effect appears to be a significant factor in this regard. However, the importance of metakaolin content, w/s and superplasticizer dosage also need to be quantified.

## **2.3 Property Evolution**

### *2.3.1 Compressive Strength Development*

Compressive strength development of LC<sup>3</sup> can be affected by a myriad of factors such as composition and proportioning of constituent materials, added gypsum and alkali contents, and curing temperature [32-34, 41, 45, 48, 51, 58, 60-63]. Among these factors, much focus has been on the influence of calcined kaolinite content in calcined clay because of its significance not only for the property evolution but also for the sustainability and cost of LC<sup>3</sup> [33, 48, 49, 51, 58]. While increasing calcined kaolinite content in calcined clay has proven beneficial for compressive strength development until 3 days, it has been suggested that 40% calcined kaolinite content in calcined clay could be sufficient to achieve comparable strength to PC beyond 7 days [13]. The reason strength depended less on calcined kaolinite level after 7 days was roughly completed formation of carboaluminates until 7 days in all mixes including at least 40% calcined kaolinite [33, 47].

Overall, LC<sup>3</sup> has proven itself as a binder with a comparable strength to PC at both early and late ages of hydration. However, there is a lack of similarity between the results. For example, some studies reported lower compressive strength with LC<sup>3</sup> than PC (baseline samples) until 3 days [33, 41, 45, 49, 58, 61, 64], whereas relatively higher earlier strength with LC<sup>3</sup> was also observed [32, 62, 63]. These inconsistencies may be originating from

various reasons such as varying alkali content of PC clinker, limestone particle size or calcined clay reactivity, which can mediate the strength development through the modifications in the pozzolanic reactions and porosity refinement [51, 60].

While the relationship between calcined clay composition and strength has gained the most interest by researchers, the role of limestone in this regard was paid less attention. Nevertheless, small number of studies addressed the impact of the purity (i.e., calcite content) [65] and particle size [58] of limestone. However, the effect of limestone particle size on strength in comparison to other strength-impacting factors such as the PC replacement level or metakaolin fraction has not been quantified yet. Conceivably, this assessment can help design LC<sup>3</sup> concrete with respect to both sustainability and strength criteria. It is hypothesized that increasing the PC replacement level beyond 45% without compromising strength through the variations in particle sizes of calcined clay or limestone, may be favorable from the sustainable-design point of view. Additionally, the observation of continuous strength development of LC<sup>3</sup> after 28 days, when hydration reactions are extremely limited, also needs to be explained [34]. This new understanding can broaden the perspective to formulate LC<sup>3</sup> binders for continuous strength development.

### 2.3.2 *Durability*

Up to date durability studies for LC<sup>3</sup> span its resistance against chloride ingress, alkali-silica reaction (ASR) and carbonation [49, 62, 63, 66-69], on which further research is still encouraged [34]. Additionally, more data are needed to probe LC<sup>3</sup>'s performance against other common degradation mechanisms such as freeze-thaw, sulfate attack and fire

resistance [34]. Although carbonation seems to be a concern for LC<sup>3</sup> [67], it has still been manifested as a durable material against the chloride ingress and ASR.

LC<sup>3</sup> assures higher ASR resistance than PC owing to its pore solution with lower alkalinity and higher concentration of aluminum ions. The aluminum ions in the pore solution can restrict the dissolution rate of silica from aggregates by adsorbing on silicate surfaces [34, 70]. An initial study confirmed this prospect of LC<sup>3</sup> in alleviating ASR [68]. In this study, the authors used a flash calcined low-grade calcined clay including 50.9% amorphous and 49.1% quartz content in producing LC<sup>3</sup>-based mortars. Two types of LC<sup>3</sup> were designed consisting of: 20%, (LC<sup>3</sup>-20) and 30% (LC<sup>3</sup>-30) PC substitution levels by calcined clay and limestone at a constant mass ratio of 2:1. The LC<sup>3</sup>-20 and LC<sup>3</sup>-30 mortar bars suffered 33%, and 56% less ASR expansion, respectively, compared to the PC-based mortars at the end of testing period (100 days), measured based on an almost identical test method to ASTM C1260 [71]. This improvement in the ASR mitigation with LC<sup>3</sup> was attributed to its low alkali content in the pore solution, and formation of the ASR gels with less swelling capability.

Recent studies showed LC<sup>3</sup>'s greater resistance against the chloride ingress compared to PC and some other ACMs, mainly due to the great pore refinement [49, 62, 63, 69]. To illustrate, compared to plain PC or PC-fly ash binders, LC<sup>3</sup> displays a more tortuous pore structure, leading to a better resistance against the penetration of aggressive ions such as chloride [63]. This pore refinement in LC<sup>3</sup> – which can be achieved as early as 3 days – was mainly attributed to its calcined clay component rather than limestone. Because, calcined clays can accelerate greatly the hydration reactions due to their highly reactive nature and large specific surface area depending on their calcined kaolinite content

[48, 72]. Therefore, in the interest of optimizing the kaolinite component in calcined clay for the durability of LC<sup>3</sup>, various calcined clay sources with different kaolinite contents have been experimented [48, 49]. In [49], the chloride diffusion coefficient of LC<sup>3</sup> diminished with increasing calcined kaolinite, and was reported up to two orders of magnitude lower than that of PC due to the great porosity refinement. In addition, chloride binding of LC<sup>3</sup> was found significantly higher compared to PC for blends containing 40-80% kaolinite in calcined clay. The dependency on kaolinite content in the calcined clay was due to increasing Friedel's salt with increasing carboaluminates. Hence, not surprisingly reinforced concrete members such as a typical reinforced bridge pier and bridge girders were projected to achieve longer service life in the case of chloride exposure when they were LC<sup>3</sup>-based in comparison to PC [66].

A meaningful contribution to the understanding of composition versus durability such as chloride ion penetration can be achieved perhaps by also considering the potential variations in the microstructure of LC<sup>3</sup> originating from various particle sizes of constituent materials (i.e., limestone). Further, the role of sulfate adjustment is yet to be studied in this context as mentioned previously in Section 2.1.3. It is hypothesized that LC<sup>3</sup>'s resistance against the chloride ion ingress, can be modified by these compositional variables because both these parameters can mediate the tortuosity and phase assemblage.

### 2.3.3 Rheology

Several in-depth studies regarding the rheological properties of LC<sup>3</sup> have been published recently, which touched upon the composition-rheology linkages [73-76]. Among various compositional factors, calcined clay has proven itself as the central

determinant for the rheological properties of LC<sup>3</sup> from various reasons such as its high specific surface area, negative surface charge and layered molecular structure [73, 74]. These properties of calcined clay enhance the overall water demand of LC<sup>3</sup> and promote flocculation thus resulting in greater yield stress and plastic viscosity than PC [73-75]. It is therefore not surprising to notice in the literature that superplasticizers have been necessary for achieving proper dispersion with LC<sup>3</sup> binders (i.e., w/s ≤ 0.5) [77]. Moreover, it has been suggested that kaolinitic clays (1:1 type phyllosilicate) require more superplasticizer than other clays (i.e., 2:1 type) because superplasticizer molecules may be intercalated within the layered structure of calcined kaolinite [76]. In parallel, some research has been devoted to optimize the molecular design of chemical admixtures for LC<sup>3</sup>, especially polycarboxylate-ether (PCE) based, focusing on calcined clay-admixture compatibility [64, 78]. Per the scope of this dissertation, preliminary findings about the admixture design for LC<sup>3</sup> are not discussed in this section. Instead, up-to-date findings and the underlying mechanisms of the rheological properties of LC<sup>3</sup> are detailed in the following.

To illustrate the relatively high yield stress and plastic viscosity of LC<sup>3</sup> compared to PC, originating mainly from the inclusion of calcined clay, data from two recent studies can be discussed [73, 74]. [74] showed that the 55:30:15 paste, traditional formulation of LC<sup>3</sup>, achieved 222.8 Pa dynamic yield stress – the highest stress needed to stop the flow - within 10 minutes after mixing, which was about 930% higher than that achieved by the PC paste prepared with the same w/b of 0.45. Similarly, LC<sup>3</sup> exhibited a greater plastic viscosity than PC, approximately 600% higher. These strikingly large differences between two binders could be explained by the high water demand of calcined clay. [73] has contributed to this understanding on the calcined clay effects by displaying a correlation

between the zeta potential of the system and the static yield stress – the minimum stress needed to initiate the flow.

The zeta potential is the electrokinetic charge measured at the slipping/shear plane, which separates the particle from the mobile liquid (Figure 2.5) [79, 80]. The correlation between the zeta potential and yield stress across different formulations revealed that increasing calcined clay content reduces the zeta potential, which in turn diminishes the repulsion between cementitious particles. This decrease in the magnitude of zeta potential (shown as  $\phi$  in Eq. 2.4) was due to the negative surface charge of calcined clay balancing the positively charged limestone and PC. According to the DLVO theory, low absolute values of zeta potential corresponds with weak electrostatic repulsive forces (Eq. 2.4), which translates to flocculation (Figure 2.6) [73, 79]. Given this role of zeta potential, the impacting factors of the zeta potential of calcined clay was examined in [81]. This study showed that the zeta potential of calcined clay incorporating mixes decreases in magnitude with increasing kaolinite content in clay. Based on these findings, it has been understood that not only the particle structure or fineness of calcined clay prevails the rheology of LC<sup>3</sup>, but also its surface properties need to be considered.

$$W_{repulsive} = 2\pi\epsilon\epsilon_0 r \phi^2 \ln [1 + (-Kh)] \quad (2.4)$$

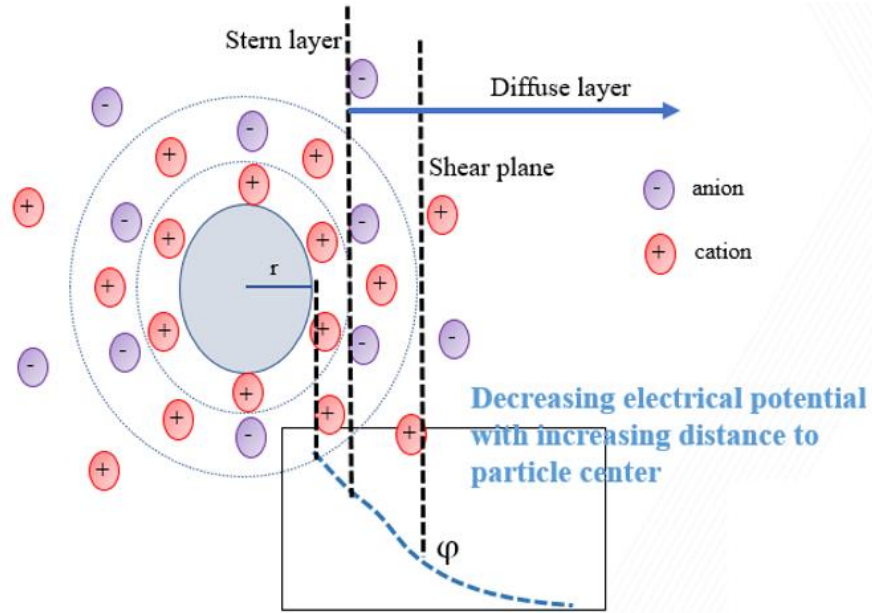


**Figure 2.5 – Zeta potential according to electrical double layer model**

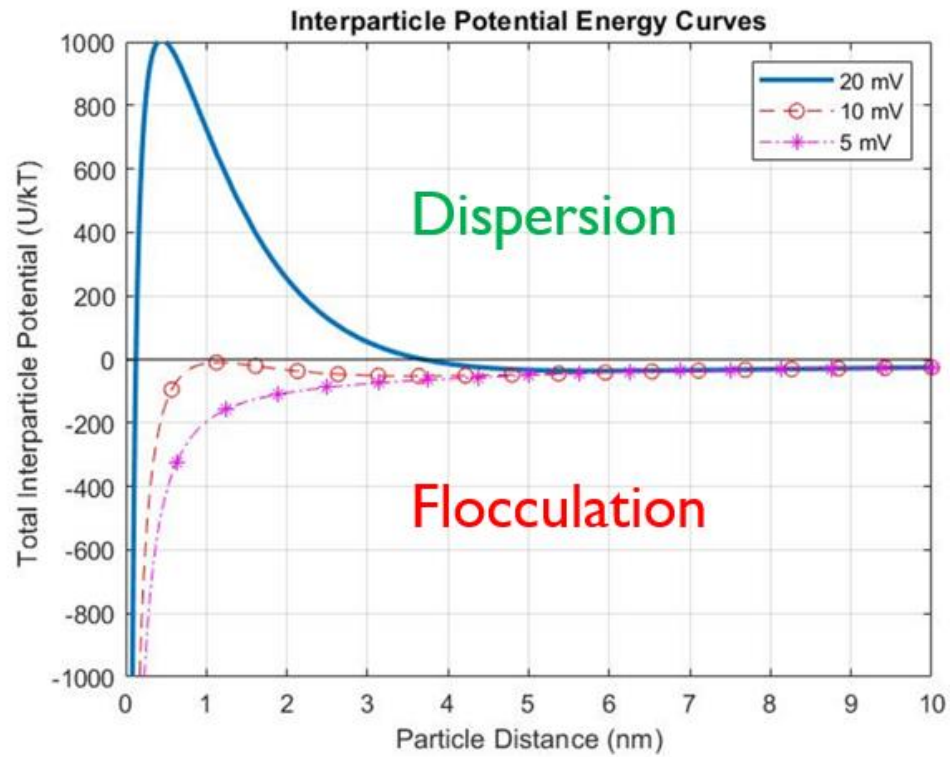


**Figure 2.6 - Interparticle potential energy curves for PC showing the significance of the zeta potential to achieve dispersion in the cement suspensions [79, 82].**

High initial static yield stress of  $LC^3$  due to the presence of calcined clay has also spurred researchers to investigate whether structures with satisfactory buildability can be

produced by 3D-printing using LC<sup>3</sup> as the binder [75, 83]. The motivation behind this endeavour is not limited to increase the use of ecologically beneficial LC<sup>3</sup>, but also to facilitate the adaptation of 3D-printing methods in the concrete industry if ACMs like LC<sup>3</sup> can be put at its disposal. Up to date findings recommended to improve the printability of LC<sup>3</sup> by incorporating silica fume to the mix design [75], using calcined clay that includes residual kaolinite [83] or adding viscosity-modifying admixtures [84]. Notwithstanding the lack of data and understanding on how other factors than calcined clay modifies the rheology of LC<sup>3</sup>, studies about the printability of LC<sup>3</sup> are important and expected to surge in the future.

Depending on the various sources across different geographies, the composition of calcined clay significantly varies such as its calcined kaolinite content and fineness, which can lead to different rheological properties. However, the literature concerning with the influence of varying calcined clay composition on LC<sup>3</sup> rheology is scarce. It is worth noting that LC<sup>3</sup> rheology is influenced not only by calcined clay but there are also other factors that can play a major role. For instance, particle packing can be modified through variations in limestone particle size used, which is significant for flowability of cement binders [85]. Further, the rheological behaviour of LC<sup>3</sup> may be altered by varying the added gypsum content because of its influence on early silicate and aluminate reactivity [30]. Understanding LC<sup>3</sup> rheology needs to be broadened by examining the contribution of other compositional factors than calcined clay.

## **2.4 Summary of the Knowledge Gaps and Technical Needs Addressed**



Achieving sulfate balance is of primary importance in the design of not only LC<sup>3</sup> but all cementitious binders including calcium aluminate phases (e.g., PC). However, as explained in Section 2.2.3, understanding of the influence of compositional factors on the sulfate balance of LC<sup>3</sup> is lacking. In addition, notwithstanding the considerable number of published studies regarding the sulfate balance of cementitious systems, a technical need exists to define the early hydration kinetics parameters including the sulfate balance in a quantitative and reproducible manner. Chapter 3 addresses this knowledge gap and technical need.

Rheological behaviour of LC<sup>3</sup> is relatively under-investigated. As discussed in Section 2.3.3, a small number of published studies have emphasized the governing role of calcined clay for the yield stress and plastic viscosity of LC<sup>3</sup>. However, these studies did not investigate the effects of varying particle sizes of limestone or added gypsum content that can *a priori* influence the rheological properties of LC<sup>3</sup> through the variations in particle packing or sulfate balance of the system, respectively. Chapter 4 addresses this knowledge gap by providing insights relying on empirical and statistical analyses. In addition, a ML model is introduced to predict the yield stress and plastic viscosity.

In contrast, the role of calcined clay composition and content on LC<sup>3</sup>'s bulk properties, such as compressive strength development, has been examined extensively by researchers. However, the influences of the filler effect and sulfate balance have not been well-examined in this context. Chapter 5 relates LC<sup>3</sup>'s microstructural development to bulk property development (i.e., compressive strength and surface resistivity), while quantifying the compositional effects on the strength and resistivity development. Strong correlations

established in this chapter (e.g., between compressive strength and surface resistivity development) can guide the mixture design of LC<sup>3</sup>.

The transition of LC<sup>3</sup> from the laboratory to field is highly dependent on the ability to formulate it with respect to performance and sustainability. This is an optimization problem because both the performance and sustainability are dependent on composition (e.g., PC fraction). Chapter 6 addresses this problem by providing a multi-objective optimization tool. As a proof-of-concept, this optimization tool develops various LC<sup>3</sup> formulations to achieve desired compressive strength and global warming potential criteria while simultaneously predicting these properties.

## **CHAPTER 3. A QUANTITATIVE APPROACH TO DETERMINING SULFATE BALANCE FOR LC<sup>3</sup>**

### **3.1 Introduction**

The consumption of sulfate ions in the first 24 h of hydration is mediated by C-S-H and ettringite formation in PC-based binders [29, 30, 86]. For instance, during the acceleration period of hydration sulfate ions can first be bound in C-S-H and ettringite and then released from C-S-H to react with calcium aluminate hydrates (e.g., C<sub>3</sub>A) to form ettringite again [29, 59]. If the amount of sulfates in the mix design is not enough to curb C<sub>3</sub>A dissolution, cement pastes rapidly harden due to rapid precipitation of aluminum hydrate phases (i.e., C<sub>2</sub>AH<sub>8</sub> or C<sub>4</sub>AH<sub>13</sub>) [87], which is also known as “flash set”. The undersulfation also delays the silicate reaction because the dissolution of C<sub>3</sub>S can be suppressed by a high concentration of aluminum ions in the pore solution [28, 29]. As a result, some early age properties such as compressive strength may diminish [28]. Based on the direct relationship between the capillary porosity and sulfate content [59], it can be deduced that the sulfate content is significant not only for early age properties like strength but also for durability.

The above-mentioned mechanism of the interaction between sulfate ions and cement hydrated phases brings about a myriad of factors influencing the sulfate balance of cementitious materials. These factors span the physical and chemical characteristics of constituent binder materials, fineness of C<sub>3</sub>A and calcium sulfate source (i.e., solubility) [30, 31, 88, 89]. Hence, the understanding of the sulfate balance of cement binders merely based on mix design or compositional variables is a challenging multi-faceted problem. This problem is aggravated in the case of blended cementitious materials, especially LC<sup>3</sup>.

Because, LC<sup>3</sup> incorporates two SCMs, limestone and calcined clay, onto which sulfate ions may be adsorbed through bridging with Ca<sup>2+</sup> [57]. Given these complexities, the sulfate balance of LC<sup>3</sup> could not be predicted *a priori* based on composition.

The sulfate balance of LC<sup>3</sup> has been evaluated as to whether aluminate peak occurs after the silicate peak in the heat flow curves obtained from isothermal calorimetry. The heat flow curves show that the alumina peak is delayed, therefore separated from the alite peak, with increasing sulfate content, which is typically provided by extra gypsum. In this context, a common practice to understand the sulfate balance based on heat flow curves has been to compare the time of occurrence of the sulfate depletion point, also called as the onset of aluminate peak, between various mixes [30]. The sulfate balance, however, addresses not only the sulfate depletion point, but its proximity with the silicate peak [90]. In other words, the sulfate balance is achieved not when the sulfate depletion point is delayed but is separated from the silicate peak. Therefore, identifying the heat flow parameters (i.e., time of maximum of silicate peak and sulfate depletion point) accurately can allow for quantification of the sulfate balance. With this approach, the impacting factors for the sulfate balance of LC<sup>3</sup> could be investigated in a quantitative and comparative manner.

It was recently shown that a significant factor for the sulfate balance of LC<sup>3</sup> is the rapidness of the silicate reaction, which can be accelerated via the filler effect of SCMs [30, 57]. This is due to the accelerated nucleation of C-S-H, which can adsorb the sulfate ions from the pore solution. Hence, the higher the C-S-H nucleation the earlier the sulfate depletion. However, a disagreement exists as to whether the alumina content of calcined clay affects the sulfate depletion point independent of its particle size or specific surface

area. Contrary to some previous studies [31, 41, 91], [30] suggested that the aluminate content of calcined clay does not modify the optimum sulfate level of LC<sup>3</sup>. Further, these studies were only concerned with the sulfate depletion point and did not quantify its proximity to the silicate peak for evaluating the overall sulfate balance. In addition to this controversy revolving around the alumina content, there is little published data available to understand the influence of w/s and superplasticizers on the sulfate balance of LC<sup>3</sup>.

### **3.2 Research Significance**

Determination of the correct sulfate need in limestone calcined clay cements (LC<sup>3</sup>) to control aluminate hydration is critical for early hydration and property development, but the role of the metakaolin fraction has not been previously well-explored. In addition, there is little published data available investigating the influence of water-to-solid ratio (w/s) and superplasticizers in this context. This study assesses the influence and quantifies the relative importances of compositional predictors on the sulfate balance and cumulative heat evolved by 24 h of LC<sup>3</sup> through a stepwise regression model. Moreover, a methodology is developed based on Kernel regression to precisely identify the heat flow parameters such as the sulfate depletion point and the slope of silicate peak. This approach allows the sulfate balance to be defined quantitatively.

### **3.3 Experimental**

#### *3.3.1 Materials*

Type I/II PC, a high purity ( $\geq 95\%$ ) metakaolin, and three different limestone powders were sourced from Argos Cement (Atlanta, GA), BASF (Gordon, GA) and Imerys

(Sylacauga, AL), respectively. Also, reagent-grade gypsum was used ( $\geq 98\%$  calcium sulfate dihydrate) in this study that was sourced from Acros Organics (Fair Lawn, NJ). Limestone powders ( $\geq 98\%$   $\text{CaCO}_3$  by mass, as determined with TGA) were selected based on their average particle diameters ( $D_{50}$ ) representing smaller-sized (L3), larger-sized (L25), and similar-sized (L15) to the PC used. The particle size distributions (Figure 3.1) were measured using ethanol as a dispersant (Malvern Mastersizer 3000E). Table 3.1 introduces the median particle diameter ( $D_{50}$ ) and specific surface area of all the materials calculated from their particle size distribution analyses. The oxide compositions of the materials determined by XRF analysis, and the phase composition of PC determined by Rietveld analysis with XRD under Cu-K $\alpha$  radiation are introduced in Table 3.2.

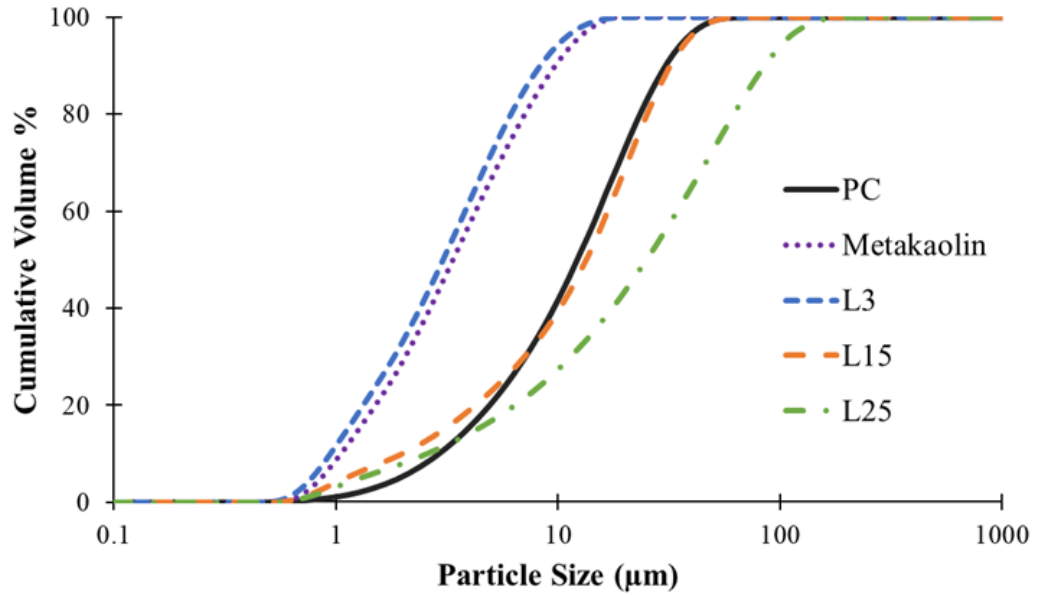


**Figure 3.1 - Particle size distribution of materials used**

**Table 3.1 - D<sub>50</sub>, specific surface area (SSA) and specific gravity of raw materials**

	PC	Metakaolin	L3	L15	L25
D <sub>10</sub> (μm)	2.90	1.05	0.94	1.98	2.56
D <sub>50</sub> (μm)	13.80	3.37	3.03	13.37	24.99
D <sub>90</sub> (μm)	30.50	9.74	8.32	32.04	85.00
SSA (m <sup>2</sup> /kg)	268.10	2211.00	2477.00	924.30	824.90
Specific gravity (g/cm <sup>3</sup> )	3.03	2.48	2.67	2.62	2.60

**Table 3.2 - Oxide and phase composition of the materials**

	PC	Metakaolin	Limestone
CaO	61.74	0.04	55.00
SiO <sub>2</sub>	20.48	51.41	0.80
Fe <sub>2</sub> O <sub>3</sub>	3.07	0.33	0.30
Al <sub>2</sub> O <sub>3</sub>	4.46	43.04	0.30
SO <sub>3</sub>	2.56	0.05	0.00
Na <sub>2</sub> O	0.09	0.20	0.00
K <sub>2</sub> O	0.43	0.10	0.00
MgO	3.20	0.00	1.80
TiO <sub>2</sub>	0.22	1.56	0.00
Loss on ignition (%)	2.10	1.43	41.80
C <sub>3</sub> S	57.60	-	-
C <sub>2</sub> S	34.10	-	-
C <sub>3</sub> A	1.90	-	-
C <sub>4</sub> AF	4.40	-	-
C\$	1.2		

### 3.3.2 Mix design

To build composition-sulfate balance linkages for LC<sup>3</sup>; metakaolin fraction, w/s, LS particle size, added gypsum content and superplasticizer (SP) content were varied as described in Table 3.3. Accordingly, the effects of w/s, LS particle size, added gypsum and SP could be investigated for each PC:MK:LS.

All the pastes prepared with w/s of 0.40 included 0.5% superplasticizer (BASF MasterGlenium 7920) by mass of solid (PC+MK+LS+Gypsum). SP content in each PC:MK:LS was varied only at w/s of 0.55. The effect of added gypsum content was explored at w/s of 0.40 for each PC:MK:LS, also at w/s of 0.75 for only the 55:30:15 paste. The pastes prepared with w/s of 0.55, 0.60 and 0.65 included constant 2% added gypsum for each PC:MK:LS. LS particle size varied in each PC:MK:LS paste at w/s of 0.40, 0.65, and 0.75, whereas the pastes prepared using w/s of 0.55 and 0.60 included only L15. As a result, 58 pastes were prepared for testing with isothermal calorimeter. Deionized water with a resistivity of 18.2 MΩ was utilized for all mixes.

**Table 3.3 - Experimental matrix based on mass ratio for isothermal calorimetry**

PC:MK:LS	Water-to-solid ratio (w/s)	LS particle size	Added gypsum (wt. %)	SP (wt. %)
55:30:15	0.40, 0.55, 0.6, 0.65, 0.75	L3, L15, L25	0, 2, 5	0, 0.1, 0.25, 0.5
55:22.5:22.5	0.40, 0.55, 0.6, 0.65, 0.75	L3, L15, L25	0, 2, 5	0, 0.25, 0.5
55:15:30	0.40, 0.55, 0.6, 0.65, 0.75	L3, L15, L25	0, 2, 5	0, 0.1, 0.5

### 3.3.3 Experimental



Paste samples for isothermal calorimetry were prepared using a 5-speed high shear blender. The mixing procedure was adapted from [92, 93] and can be summarized as follows: Only solids (PC+MK+LS+gypsum) were mixed for 30 s at low speed to achieve homogenization and then water was added. After, the paste was mixed for 30 s at low speed and then 60 s at medium setting. The paste was allowed to rest for 90 s and then the mixing was finalized with an additional 60 s medium-speed mixing.

Heat evolution of cement pastes was investigated using an isothermal calorimeter (TAM Air, TA Instruments). The samples were prepared outside the calorimeter at room temperature ( $23 \pm 2$  °C ( $73.4 \pm 3.6$  °F)) and then 10 g of pastes were loaded into the calorimeter. Rate of heat evolution and cumulative heat evolution of cement pastes were assessed at 23 °C (73.4 °F) up to 48 hours. To ensure reproducibility (i.e., coefficient of variation  $\leq 3\%$  cumulative heat evolved by 24 h), two replicates were prepared for the sample, and the average values were reported.

To understand the modifications in the evolution of hydrated phases caused by adding extra gypsum, in-situ XRD was performed on the pastes 55:22.5:22.5 including L3 prepared at w/s of 0.40 with SP addition of 0.5% by mass of solid. One paste was prepared without extra gypsum, whereas 5% extra gypsum was added to the other paste. The paste mixing procedure for in-situ X-ray diffraction (XRD) measurements was the same as isothermal calorimetry. Fresh cement pastes were cast into 27 mm diameter sample holders and covered with a 6  $\mu$ m polyester film made of stretched polyethylene terephthalate to prevent evaporation and carbonation [94]. The scans were taken up to first 24 h of hydration. XRD (Malvern PANalytical Empyrean) was performed at 45 kV and 40 mA with 0.154 nm Cu K $\alpha$  radiation. The scans were obtained between 5-60° 2 $\theta$  at room

temperature within 11 min. of mixing, with a step size of  $0.0313^\circ 2\theta$ . A  $1/8^\circ$  divergence slit and a 0.04 rad. soller slit were used. A qualitative approach was taken to track the evolution of hydrated phases (i.e., ettringite and hemicarboaluminate) based on the non-overlapped peak heights similar to the approaches reported in [94, 95].

### 3.4 Computational methods

#### 3.4.1 Regression model for predicting the sulfate balance of $LC^3$

Five compositional predictors were identified, which are hypothesized to influence the sulfate balance of  $LC^3$ :

- Superplasticizer (SP) content (by mass of solid),
- Solid volume concentration ( $\Phi$ ),
- MK fraction (wt.% of solid),
- Average particle size of the total cementitious solid (APS), and
- $SO_3$  (%) of total cementitious solid (by mass percentage) based on XRF (Table 3.2).

In this study, same commercial PCE-based superplasticizer was used across mixes, but the dosage varied. The literature shows that these polymers can adsorb on  $C_3S$  and impede its dissolution [96]. This implies that the sulfate balance of mixes can be significantly altered by varying dosages of PCE-based superplasticizers because it is directly related with initial C-S-H formation. Therefore, regression model incorporates superplasticizer content as a predictor.

The aluminate peak of LC<sup>3</sup> can be modified by w/s [33]. To capture these variations, solid volume concentration (Eq. 3.1) was introduced into the model. Instead of w/s solid volume concentration was introduced because it is a more generalizable predictor than w/s. That is, unlike w/s the specific gravity of constituent materials was considered in the solid volume concentration.

$$\Phi = (1 + \frac{(SG_{OPC} \times m_{OPC} + SG_{MK} \times m_{MK} + SG_{LS} \times m_{LS} + SG_G \times m_G) \times w/s}{SG_W})^{-1} \quad (3.1)$$

MK fraction has proven to influence both the silicate and aluminate peaks [48]. Therefore, the predictor MK was defined based on the percentage of metakaolin in total solid by mass. It is also worth mentioning that combining MK and limestone fractions at different mass ratios while keeping the PC content constant can mimic different clay grades and thus enable interpretations to be made in that regard [30, 33].

The filler effect of fine MK or LS particles corresponds with accelerated C-S-H formation. This can alter the sulfate balance of LC<sup>3</sup> because of the ability of C-S-H to adsorb sulfates as mentioned earlier. To capture these changes in the sulfate balance caused by the inclusion of fine particles (e.g., the filler effect), average particle size of the total cementitious solid (APS) was calculated for each mixture based on the D<sub>50</sub> of constituent materials measured (Table 3.1). For example, the finer the limestone particle size (L3 versus L25) in a mix the lower the APS defined in Equation 3.2:

$$APS = \phi_{OPC} \times d_{OPC} + \phi_{MK} \times d_{MK} + \phi_{LS} \times d_{LS} \quad (3.2)$$

Because the sulfate addition is adjusted on a mass basis for cementitious mixtures, the predictor  $\text{SO}_3$  (%) was defined also on a mass basis.

A stepwise regression model was implemented to predict the sulfate balance of  $\text{LC}^3$  while comparing the relative importance of five compositional predictors defined above. This regression algorithm is preferred because it can perform predictor selection based on the minimized Akaike information criterion (AIC) while making predictions (please see Section 4.4 for a detailed description of the stepwise algorithm) [97]. The five predictors were also used to predict the cumulative heat evolved by 24 h. The reason for predicting the cumulative heat evolution was to understand the different mechanisms underlying the sulfate balance and total amount of hydrated phases formed until 24 h, estimated by cumulative heat evolution [98]. The response (dependent) variable sulfate balance was taken as the time difference, represented with hours, between the sulfate depletion point (h) and the time of maximum of silicate peak (h). The longer this time difference the higher the sulfate balance is informed (Figure 3.2). This approach of relating the times of maximum of silicate peak and that of sulfate depletion to calculate the sulfate balance was inspired by [90].

Before implementing the regression models, the original dataset of 58 observations was preprocessed. This step consisted of removing some observations where the aluminate peak was superimposed on the silicate peak (no extra gypsum added pastes). Hence, the original dataset was reduced to 46 observations for the regression models. After this preprocessing, all the predictors were standardized by subtracting each data point from its mean and dividing by its standard deviation, and then the dataset was split randomly to training (75%) and testing (25%) sets. Using Monte Carlo Cross-Validation algorithm with 100

computations, the model performance metric root mean squared error (RMSE) (Eq. 3.3) was calculated from the average of the 100 computations, by:

$$\text{RMSE} = \sqrt{\frac{\sum_{i=1}^n (Y_i^{\text{actual}} - Y_i^{\text{model}})^2}{n}} \quad (3.3)$$

In these equations,  $n$  represents the number of data points,  $k$  is the number of variables,  $Y^{\text{actual}}$  is the actual (measured) strength and  $Y^{\text{model}}$  is the predicted strength by the model.

### 3.4.2 Kernel smoothing for parametrizing heat flow curves

The technical literature lacks an established method to precisely identify the early hydration kinetics parameters (i.e., time of maximum of silicate peak, sulfate depletion point, slope of silicate peak). Without taking the time derivatives of heat flow curves, determination of these parameters can be a cumbersome procedure with high variability. Kernel regression technique based on the Nadaraya-Watson (NW) estimator allows to take the time derivatives of heat flow curves and therefore can be used to determine these parameters (Figure 3.2). The NW predictions of the heat flow were constructed based on the equations shown below (3.4 to 3.6) using the Epanechnikov kernel (Equation 3.6):

$$\hat{y}(t) = \frac{\sum_{j=1}^n K_h(t - t_j) y(t_j)}{\sum_{j=1}^n K_h(t - t_j)} \quad (3.4)$$

$$K_h(t - t_j) = \frac{1}{h} K\left(\frac{t - t_j}{h}\right) \quad (3.5)$$

$$K(u) = \frac{3}{4} (1 - u^2) I(|u| < 1) \quad (3.6)$$

In these equations,  $t$  is time,  $y(t_j)$  is the actual heat rate at any time  $t_j$ , and  $\hat{y}(t)$  is the predicted heat flow at time  $t$ . The bandwidth ( $h$ ), which greatly affects the shape of the kernel, was chosen through leave-one-out cross validation [97]. Thereafter, the time derivatives of the NW predictions were calculated. All of the computations were performed in R. The heat flow predictions calculated for the first 24 hours of hydration - the time period of interest in this research – resulted in RMSE of less than 0.82 mW/g.

As Figure 3.2 illustrates, in a properly sulfated mixture, the time of maximum of silicate peak is the second time when the time derivative equals zero, whereas the sulfate depletion point is the third time when the time derivative equals zero. The slope of silicate peak can be calculated by taking the average of derivatives in the acceleration period until the time of max. of silicate peak.

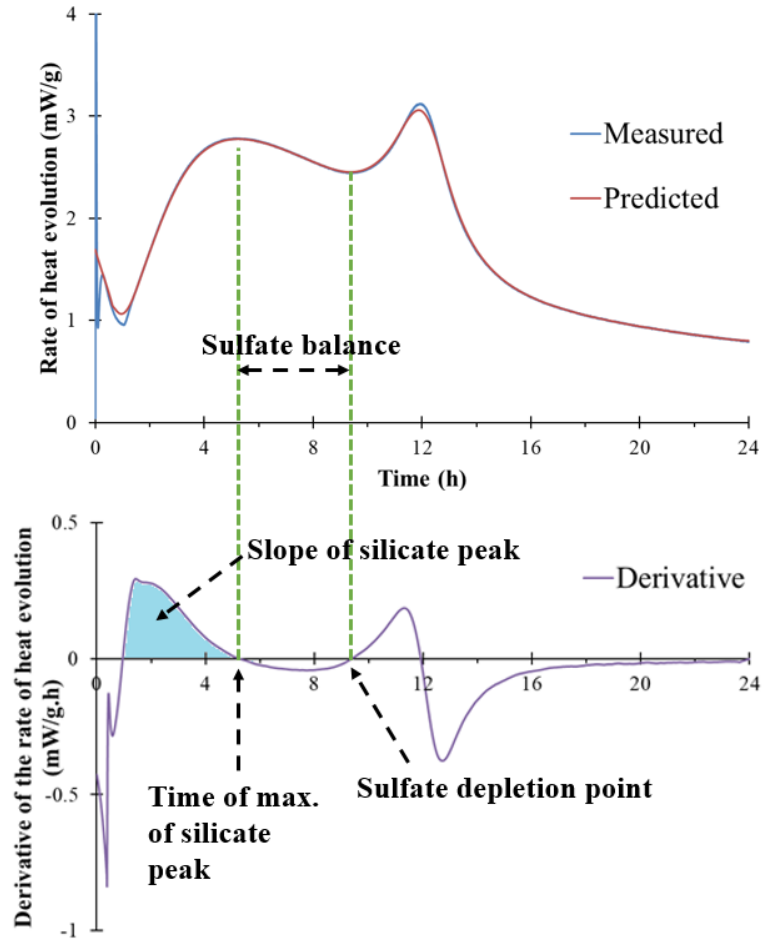


**Figure 3.2 - The time of max. of silicate peak and the sulfate depletion point determined by NW Kernel estimate.**

### 3.5 Experimental Results

#### 3.5.1 Influence of Metakaolin Fraction

It is hypothesized that when all other variables such as limestone particle size are constant, increasing MK fraction leads to earlier sulfate depletion point. Because, increasing MK fraction means more surfaces available onto which calcium-sulfate ion complexes can adsorb [99, 100]. This is the trend observed in Figure 3.3a, which shows earlier appearance of the maximum heat release of the silicate peak and the sulfate depletion point in LC<sup>3</sup> pastes with higher metakaolin fractions. The slope of silicate peak

is also higher in these pastes (Table 3.4), which implies an intensified silicate reactivity with increasing metakaolin contents, resulting in a higher rate of C-S-H and ettringite precipitation and thus earlier sulfate depletion [25, 30]. Figure 3.3b shows the competition between the metakaolin fraction and the fineness of the system in determining the sulfate depletion point. For instance, medium metakaolin mix (55:22.5:22.5) incorporating finest limestone L3 shows earlier sulfate depletion point than highest metakaolin mix (55:30:15) incorporating medium size limestone L15, highlighting the significance of the fineness of the system. However, the lowest metakaolin mix (55:15:30) including L3 still shows a later sulfate depletion point than the 55:30:15 paste despite the fact that it is a finer formulation than the 55:30:15 paste including L15. These outcomes suggest that the sulfate demand of LC<sup>3</sup> is a complex phenomenon mediated not only by the fineness of the system but also by the MK fraction.

It is noted that the sulfate balance decreases with increasing metakaolin content. Remarkably, doubling the fraction of metakaolin in the mixture corresponded with approximately halving the sulfate balance (55:30:15 versus 55:15:30 displayed in Table 3.4), which suggests direct relationship between the metakaolin fraction and sulfate requirement of LC<sup>3</sup>. The reason sulfate balance decreases with increasing MK fraction is the higher influence of MK fraction on the sulfate depletion point relative to the time of max. of silicate peak. For instance, Table 3.4 shows that when MK fraction decreases from 30 to 15% at constant w/s, the largest delay in the time of max. of silicate peak is observed as 25%, whereas the sulfate depletion point is delayed at least 36%. This difference also supports the idea that sulfate ions may be adsorbed on metakaolin particles, and that



decreasing MK fraction translate to greater changes in the sulfate depletion point compared to the time of max. of silicate peak.

Besides, more hydrated phases such as C-S-H and ettringite have likely formed with increasing metakaolin shown by the trends of cumulative heat evolved by 24 h without superplasticizer. However, in the presence of superplasticizer at w/s of 0.40 (Table 3.4), cumulative heat is not linearly correlated with metakaolin fraction. In this case, the LC<sup>3</sup> paste with highest metakaolin content (55:30:15) achieved the lowest cumulative heat. This implies a non-monotonic relationship between the degree of hydration of PC clinker and metakaolin content in the blend as shown in [48]. Further, it can be deduced that the degree of hydration of PC clinker reduced most in the paste 55:30:15 with decreasing w/s, which can be attributed to the high water demand of metakaolin [74].

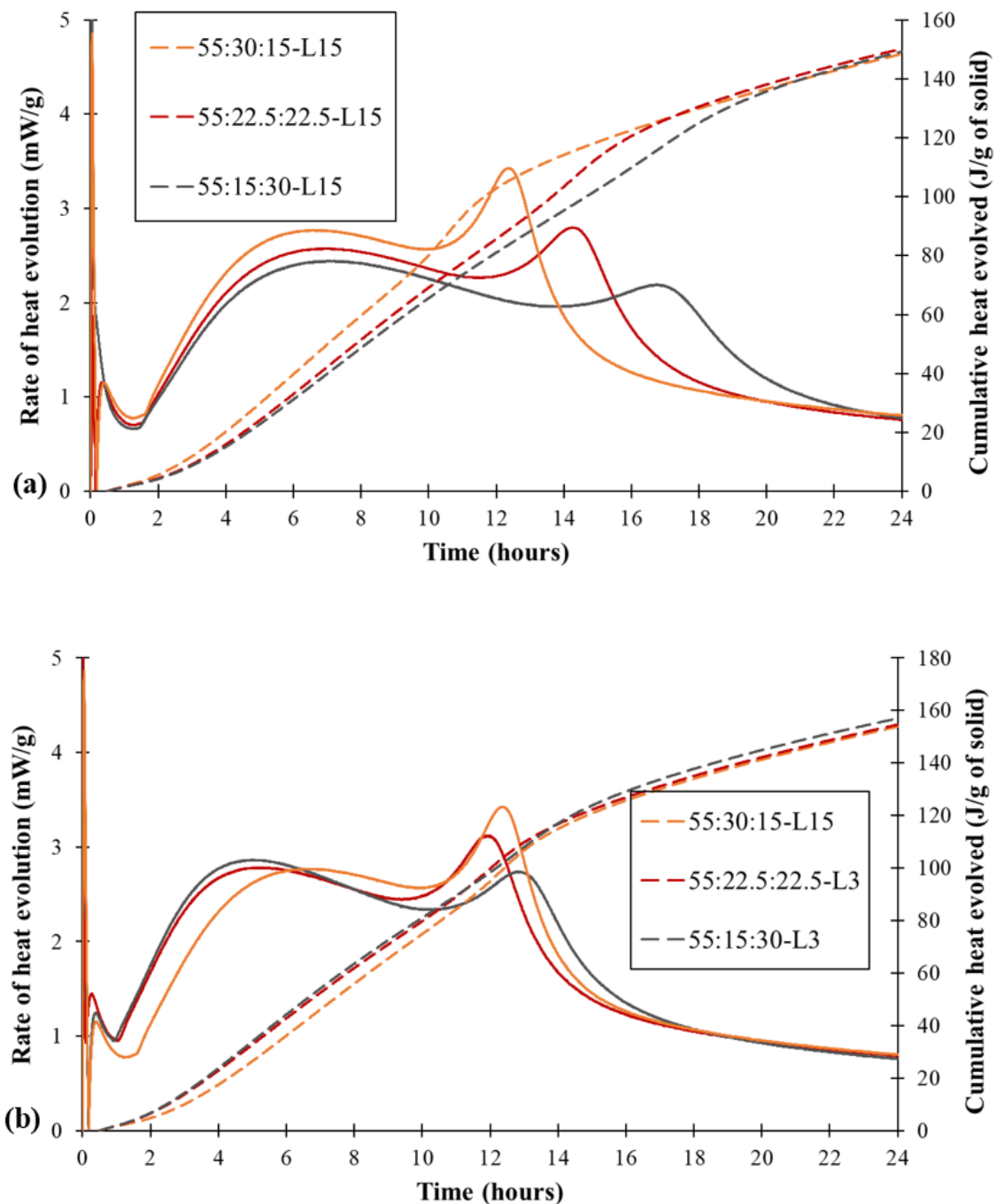


**Figure 3.3 - Heat evolution of LC<sup>3</sup> pastes during first 24 h influenced by metakaolin fraction (w/s = 0.75, SP = 0%, added gypsum content = 2%): (a) constant limestone**

particle size (L15) used in each mix, (b) the 55:30:15 paste includes L15 while the pastes 55:22.5:22.5 and 55:15:30 include L3)

**Table 3.4 - Heat flow parameters of LC<sup>3</sup> pastes including L15 influenced by metakaolin fraction (w/s = 0.40, 0.55, 0.60, 0.65, 0.75, SP = 0%, 0.5%, added gypsum content = 2%)**

PC:MK:LS	w/s	SP (wt.%)	Time of max. of silicate peak (h)	Sulfate depletion point (h)	Sulfate balance (h)	Slope of silicate peak (mW/g solid.h)	Cumulative heat evolved by 24 h (J/g)
55:30:15	0.75	0	6.7	9.9	3.2	0.14	153.7
55:22.5:22.5	0.75	0	6.9	11.4	4.5	0.12	151.4
55:15:30	0.75	0	7.1	13.8	6.7	0.11	149.9
55:30:15	0.65	0	6.6	9.2	2.6	0.14	151.4
55:22.5:22.5	0.65	0	7.0	10.7	3.7	0.12	151.9
55:15:30	0.65	0	7.3	13.1	5.8	0.11	148.7
55:30:15	0.60	0	6.4	9.0	2.6	0.14	148.8
55:22.5:22.5	0.60	0	6.8	10.2	3.4	0.12	148.3
55:15:30	0.60	0	7.2	12.2	5.0	0.11	148.2
55:30:15	0.55	0	6.1	8.3	2.2	0.15	149.5
55:22.5:22.5	0.55	0	6.6	9.8	3.2	0.12	145.8
55:15:30	0.55	0	6.9	11.5	4.6	0.11	142.1
55:30:15	0.40	0.5	6.9	8.3	1.4	0.12	124.5
55:22.5:22.5	0.40	0.5	8.3	10.0	1.7	0.10	128.7
55:15:30	0.40	0.5	8.6	12.1	3.5	0.10	126.9

### 3.5.2 Influence of Limestone Particle Size

Figure 3.4 shows the heat evolution of the 55:30:15 pastes including different limestone particle sizes. The slope of silicate reaction is linearly dependent on limestone particle size, suggesting that higher rate of C-S-H precipitation can be achieved by incorporating finer limestone particle sizes. The increase in the slope of silicate peak with L3 is likely to have resulted from the filler effect increasing the shearing between particles in the solid network [25]. Also, the time to reach the peak heat release of silicate peak and the induction period is shorter with L3 compared to L15 and L25, confirming the accelerated formation of hydration products such as C-S-H as a result of this filler effect by L3 (Table 3.5). As anticipated, sulfate depletion also occurs earlier with all the pastes incorporating L3 without superplasticizers. This phenomenon could be explained by the tendency of C-S-H – whose formation is accelerated by the filler effect of L3 - to adsorb sulfates from the pore solution [29, 30, 59]. Due to the tendency of C-S-H to adsorb sulfates from the pore solution, a correlation between the slope of silicate peak and the sulfate depletion point seems plausible as observed in Table 3.5, when variations in limestone particle size are considered. This means the higher the slope of silicate peak - achieved by using L3 - the higher the rate of C-S-H formation and the earlier the sulfate depletion. This hypothesis will be revisited in a separate section.

Moreover, Table 3.5 shows that the sulfate balance could be modified from 9 to 25% depending on the limestone content– always lower with the fine limestone (L3) in the absence of superplasticizer. The higher the limestone content the higher the modifications in the sulfate balance originating from different limestone particle sizes. In the context of modelling in this study, the effects relating fineness to the sulfate balance could be captured by the variable (APS), which will be presented later.

On the contrary, in the presence of superplasticizer the correlation between limestone particle size and sulfate balance is not systematic. For instance, L3 does not always correspond with the lowest sulfate balance as observed with the pastes 55:30:15 and 55:22.5:22.5 prepared using w/s of 0.40. In fact, the sulfate balance is highest with L3 in these pastes. These results show that when limestone content is not higher than metakaolin, using relatively coarser limestone size (e.g., L15 or L25) thus decreasing the fineness of the system does not guarantee higher sulfate balance. This observation also proposes that earlier sulfate depletion point does not always mean lower sulfate balance. As mentioned above, when L3 is used instead of L15 or L25, rate of C-S-H precipitation increases, which adsorbs sulfates and thus accelerates the sulfate depletion. It is hypothesized that this mechanism results in two types of sulfates in the system; sulfates adsorbed by hydration products such as C-S-H and ettringite, and some sulfates still available in the pore solution. This translates to decreasing sulfate concentration in the pore solution with increasing C-S-H (L3 versus L15 or L25) until the maximum of silicate peak heat release. Therefore, earlier consumption of sulfates observed with L15 and L25 compared to L3 after the maximum of silicate peak heat release implies that sulfate concentration dropped quicker in the pore solution of these pastes despite less C-S-H formed. This might be due to potential interactions between the non-adsorbed sulfate ions with PCE molecules and/or competition between the sulfate ions and PCE molecules to adsorb on cement particle surfaces [101], and it requires further investigation.

Similar to the sulfate balance, variations in the cumulative heat evolved by 24 h by limestone particle size is also dependent on the limestone content as shown by Table 3.5. While L3 could not greatly increase the cumulative heat compared to L15 or L25 in the

55:30:15 paste prepared without superplasticizer, the cumulative heat of the paste incorporating the highest limestone (55:15:30) is 5 to 6% higher with L3 compared to L15 and L25, respectively. These increases in the cumulative heat by using L3 is even higher in the presence of superplasticizer. In this case for example, L3 increases the cumulative heat of the 55:15:30 paste from 8 to 13% compared to L15 and L25, respectively. This is likely due to better dispersion of L3 in the matrix owing to the superplasticizer, providing additional nucleation sites for C-S-H. Hence, it can be deduced that the early hydration of  $LC^3$  can be modified considerably by the fineness of the mixture mediated by the limestone particle size especially in the presence of superplasticizer. These modifications brought about by the limestone particle size is strongest for the pastes containing higher limestone than metakaolin (55:15:30).

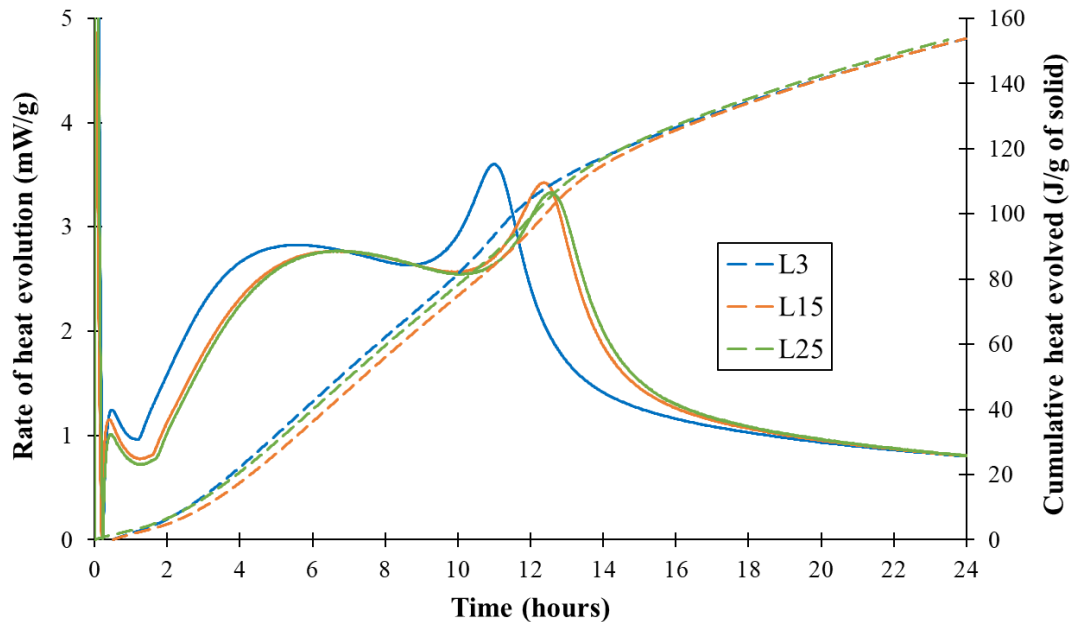


**Figure 3.4 - Heat evolution of the 55:30:15 pastes during first 24 h influenced by limestone particle size (w/s = 0.75, without SP, added gypsum content = 2%)**

**Table 3.5 - Heat flow parameters of LC<sup>3</sup> pastes influenced by limestone particle size  
(w/s = 0.40, 0.75, SP = 0%, 0.5%, added gypsum content = 2%)**

PC:MK:LS	w/s	SP (wt.% )	LS particle size	Time of max. of silicate peak (h)	Sulfate depletion point (h)	Sulfate balance (h)	Slope of silicate peak (mW/g solid.h)	Cumulative heat evolved by 24 h (J/g)
55:30:15	0.75	0	L3	5.6	8.7	3.1	0.15	154.1
55:30:15	0.75	0	L15	6.7	9.9	3.2	0.14	153.7
55:30:15	0.75	0	L25	6.7	10.1	3.4	0.14	153.6
55:22.5:22. 5	0.75	0	L3	5.2	9.3	4.1	0.16	154.6
55:22.5:22. 5	0.75	0	L15	6.9	11.4	4.5	0.12	151.4
55:22.5:22. 5	0.75	0	L25	7.1	11.8	4.7	0.12	151.2
55:15:30	0.75	0	L3	5.0	10.2	5.2	0.16	156.6
55:15:30	0.75	0	L15	7.1	13.8	6.7	0.11	149.9
55:15:30	0.75	0	L25	7.5	14.4	6.9	0.11	147.8
55:30:15	0.40	0.5	L3	5.2	7.1	1.8	0.15	127.1
55:30:15	0.40	0.5	L15	6.9	8.3	1.4	0.12	124.1
55:30:15	0.40	0.5	L25	7.3	8.8	1.5	0.11	125.0
55:22.5:22. 5	0.40	0.5	L3	6.0	7.9	1.9	0.14	135.5
55:22.5:22. 5	0.40	0.5	L15	8.3	10.0	1.7	0.10	128.7
55:22.5:22. 5	0.40	0.5	L25	9.0	10.6	1.6	0.09	130.6
55:15:30	0.40	0.5	L3	5.8	8.3	2.5	0.16	136.5
55:15:30	0.40	0.5	L15	8.6	12.1	3.5	0.10	126.9
55:15:30	0.40	0.5	L25	9.6	14.0	4.3	0.09	120.7

### 3.5.3 *Influence of Added Gypsum Amount*

Both the appearance of maximum of silicate peak and the sulfate depletion point are delayed with increasing added gypsum, whereas the slope of silicate peak decreases (Figure 3.5). However, the rate of delay in the sulfate depletion point is greatly higher compared to the changes in other two parameters. For instance, when gypsum content is increased from 2 to 5% for the 55:30:15 pastes prepared without superplasticizers, the sulfate depletion is delayed by 88%, whereas the maximum silicate peak heat release is delayed only by 4%. In addition, the slope of silicate peak decreases only by 7%. Similarly, in the presence of superplasticizer, when gypsum content is increased from 2 to 5%, the sulfate depletion is delayed by 77% while the time of maximum of silicate peak is delayed by 13% and the slope of silicate peak is decreased by 17%. Much larger influence on the sulfate depletion point caused by gypsum addition emphasizes the availability of sulfate ions in the pore solution in retarding the aluminate peak, with a lesser influence on the silicate reaction. As a result, the largest increase in the sulfate balance is achieved with adding gypsum considering all the compositional variables investigated in this study.

It is worth noting that the optimal sulfate balance is not always achieved with the highest gypsum content investigated in experimental designs; rather being cross-examined by early compressive strength ( $\leq 3$  days) or cumulative heat evolution [30, 31, 59, 102, 103]. For example, among the pastes introduced in Table 3.6, the 55:30:15 pastes including 5% gypsum prepared with and without superplasticizer achieves the highest cumulative heat evolved by 24 h, implying that 5% is the optimal extra gypsum amount that can achieve the highest 1-day strength.



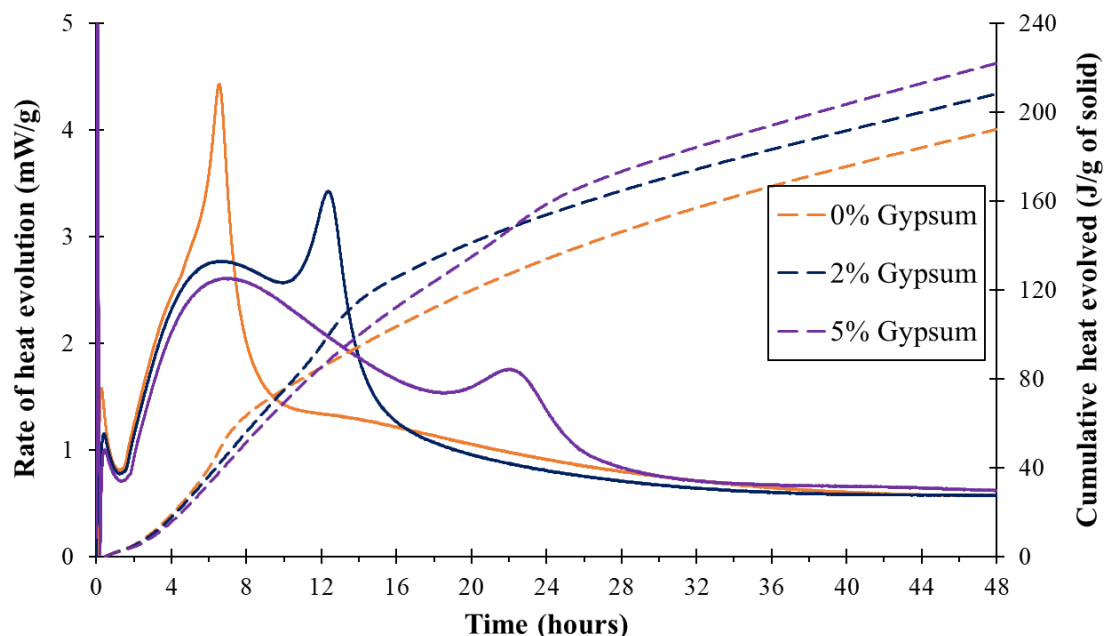


**Figure 3.5 - Heat evolution of the 55:30:15 pastes including L15 during first 24 h influenced by added gypsum content ( $w/s = 0.75$ , without SP). First 48 h of hydration was given in this figure to show the full shape of the alumina peak observed in 5% added gypsum paste.**

**Table 3.6 - Heat flow parameters of the 55:30:15 pastes including L15 influenced by added gypsum content ( $w/s = 0.75$ ,  $SP = 0\%$ )**

PC:MK:LS	w/s	SP (wt.%)	Added gypsum content (wt.%)	Time of max. of silicate peak (h)	Sulfate depletion point (h)	Sulfate balance (h)	Slope of silicate peak (mW/g solid.h)	Cumulative heat evolved by 24 h (J/g)
55:30:15*	0.75	0	0	6.5	NA	NA	0.21	132.5
55:30:15	0.75	0	2	6.7	9.9	3.2	0.14	153.7
55:30:15	0.75	0	5	7.0	18.6	11.6	0.13	159.1
55:30:15*	0.40	0.5	0	7.0	4.7	NA	0.20	115.7
55:30:15	0.40	0.5	2	6.9	8.3	1.4	0.12	124.5
55:30:15	0.40	0.5	5	7.8	12.9	5.0	0.10	135.7

\*Because the silicate peak and aluminate peak were not separated, time of max. of silicate peak and slope of silicate peak of these sample were calculated based on the peak heat release during the acceleration period.

#### 3.5.4 *Influence of W/S*

Higher w/s corresponds with longer time to reach the maximum silicate peak heat release and sulfate depletion with a lesser influence on the slope of silicate peak (Figure 3.6 and Table 3.7). These delays in the maximum silicate peak appearance and sulfate depletion might be due to reduced alkali concentration and shearing between particles with increasing w/s [31, 98]. In fact, variations in w/s influence the time of maximum of silicate peak not systematically and to a lesser extent compared to the sulfate depletion point. For example, Table 3.7 shows that the appearance of silicate peak heat release is not consistently delayed with an increase in w/s. This inconsistency was exhibited by the 55:22.5:22.5 and 55:15:30 pastes where increasing w/s from 0.65 to 0.75 slightly accelerated the appearance of the maximum of the silicate peak. Small changes in the silicate reaction parameters such as the time of maximum of silicate peak and the slope of silicate peak with respect to w/s beyond 0.65 agrees with the findings of [104], which shows similar C-S-H nucleation density despite varying w/s based on pBNG simulations. Notwithstanding the small changes in the silicate peak, the sulfate depletion is consistently delayed with increasing w/s for all the pastes investigated, leading to higher sulfate balances. This can be due to  $C_3A$ , whose reaction is delayed with increasing w/s [88, 89]. It is worth mentioning that increasing w/s did not correspond with higher aluminate peak, which may suggest similar amount of ettringite have likely precipitated independent of the variations in w/s of the system [30].

In LC<sup>3</sup> systems, the effect of w/s on the cumulative heat evolution is more pronounced typically after 48 hours in parallel with carboaluminate peak appearance [33], which is beyond the measurement period in this study. Nevertheless, Table 3.7 exhibits modest increases, between 3 and 6% depending on PC:MK:LS, in the cumulative heat evolved by 24 h by increasing w/s from 0.55 to 0.75. The increases in the cumulative heat evolution are highest with the paste incorporating lowest metakaolin content (55:15:30). In other words, decreasing MK fraction renders LC<sup>3</sup> pastes more sensitive to changes not only in limestone particle size (Section 3.5.2) but also in w/s. The reason for this trend can be explained by the tendency of metakaolin particles to flocculate by entrapping water and thus render some of the mixing water unavailable for hydration.

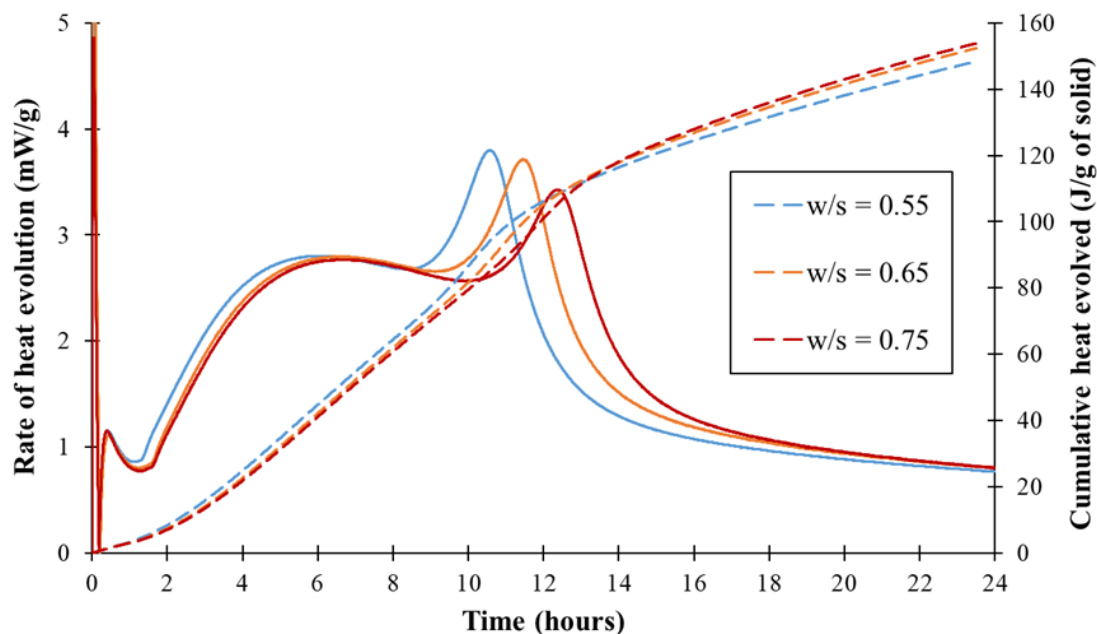


**Figure 3.6 - Heat evolution of the 55:30:15 pastes including L15 during first 24 h influenced by w/s (without SP, added gypsum content = 2%)**

**Table 3.7 - Heat flow parameters of LC<sup>3</sup> pastes including L15 influenced by w/s (without SP, added gypsum content = 2%)**

PC:MK:LS	w/s	Time of max. of silicate peak (h)	Sulfate depletion point (h)	Sulfate balance (h)	Slope of silicate peak (mW/g solid.h)	Cumulative heat evolved by 24 h (J/g)
55:30:15	0.55	6.1	8.3	2.2	0.15	149.5
55:30:15	0.65	6.6	9.2	2.6	0.14	151.4
55:30:15	0.75	6.7	9.9	3.2	0.14	153.7
55:22.5:22.5	0.55	6.6	9.8	3.2	0.12	145.8
55:22.5:22.5	0.65	7.0	10.7	3.7	0.11	151.9
55:22.5:22.5	0.75	6.9	11.4	4.5	0.12	151.4
55:15:30	0.55	6.9	11.5	4.6	0.11	142.1
55:15:30	0.65	7.3	13.1	5.8	0.11	148.7
55:15:30	0.75	7.1	13.8	6.7	0.11	149.9

### 3.5.5 Influence of Superplasticizer Content

The higher the superplasticizer added in LC<sup>3</sup> pastes the longer it takes to reach the maximum of the silicate peak and the sulfate depletion point, implying decreasing reactivity of silicate and aluminate phases with increasing superplasticizer in the first 24 h (Figure 3.7). This might be due to the steric interactions of superplasticizers, which retard the hydration reactions [105]. Accordingly, the cumulative heat evolved by 24 h and the slope of silicate peak also decrease with superplasticizer addition. In particular, the slope of silicate peak decreases by 27% when superplasticizer content is increased from 0 to 5%, indicating the diminishing effect of superplasticizer on the precipitation rate of C-S-H. It should be noted that the effect of superplasticizer dosage on the sulfate balance is smaller than other compositional variables investigated such as MK fraction or gypsum content. For instance, when superplasticizer content is doubled (0.25% versus 0.5%) in the 55:30:15 paste the increase in the sulfate balance is only 7%, whereas doubling the MK content (15% versus 30%) decreased the sulfate balance by 52%, which was discussed in Section 3.1.1.

Furthermore, the relationship between the sulfate balance and superplasticizer content is modified by the metakaolin fraction. For instance, when superplasticizer content is increased from 0 to 0.1% the sulfate balance of the 55:30:15 paste increases by 9%, whereas it increases by 20% in the 55:15:30 paste due to the changes in the time of max. of silicate peak to varying degrees. For instance, adding 0.1% superplasticizer delayed the sulfate depletion point by approximately 10% in both mixes, whereas the delay in the silicate peak appearance is smaller in the 55:15:30 paste (4%) compared to the 55:30:15 paste (11%). To explain these trends competitive adsorption between sulfates and PCE molecules should be considered. For instance, the affinity of sulfate ions was found higher

than PCE molecules to adsorb on cement particles [101]. In addition, the sulfate ions are able to adsorb on metakaolin particles like PCE molecules [57]. These trends, therefore, may imply that the adsorption-desorption kinetics between sulfate ions and PCE molecules resulted in a higher amount of PCE molecules remained to adsorb on C<sub>3</sub>S surfaces in the higher metakaolin mix (55:30:15) because the sulfate ions occupied the metakaolin surface. This phenomenon can also explain the larger changes observed in the time of max. of silicate peak and slope of silicate peak of the 55:30:15 paste compared to the variability observed in these parameters with the lowest metakaolin mix (55:15:30).

It is worth noting that some studies displayed lower sulfate balance in the presence of PCE-based superplasticizers, similar to the commercial superplasticizer used herein, for the PC systems [31]. Different hypotheses have been introduced for this trend, summarized in [31], which span increased ettringite formation and reduced rate of sulfate dissolution when PCE-based superplasticizers are added. The reason for the discrepancy between the findings in literature and the results from this study could be related to some differences in the chemistry of admixtures or binders (PC versus LC<sup>3</sup>). Therefore, more research is required to fully understand this phenomenon.

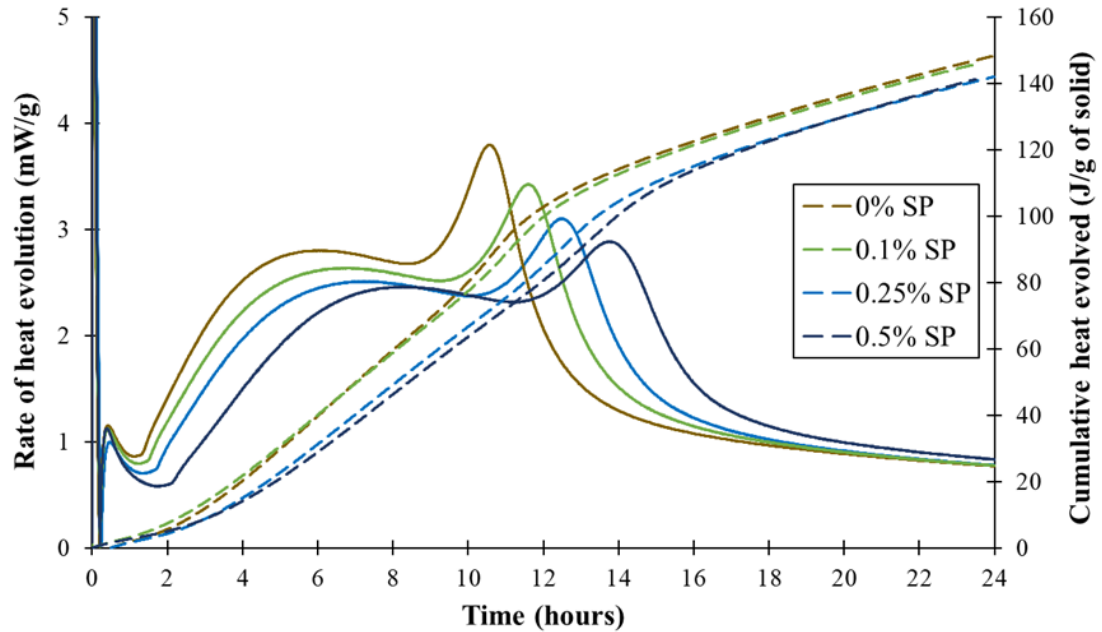


**Figure 3.7 - Heat evolution of the 55:30:15 pastes including L15 during first 24 h influenced by SP content (w/s = 0.55, added gypsum content = 2%)**

**Table 3.8 - Heat flow parameters of the LC<sup>3</sup> pastes including L15 influenced by SP content (w/s = 0.55, SP = 0%, added gypsum content = 2%)**

PC:MK:LS	SP (wt.%)	Time of max. of silicate peak (h)	Sulfate depletion point (h)	Sulfate balance (h)	Slope of silicate peak (mW/g solid.h)	Cumulative heat evolved by 24 h (J/g)
55:30:15	0	6.1	8.3	2.2	0.15	149.5
55:30:15	0.1	6.8	9.2	2.4	0.12	145.5
55:30:15	0.25	7.3	10.0	2.7	0.11	142.6
55:30:15	0.5	8.3	11.2	2.9	0.11	139.8
55:22.5:22.5	0	6.6	9.8	3.2	0.12	145.8
55:22.5:22.5	0.25	8.0	12.0	4.0	0.10	140.6
55:15:30	0	6.9	11.5	4.5	0.11	142.1
55:15:30	0.1	7.2	12.6	5.4	0.11	145.1

### 3.5.6 Relationship between the slope of silicate peak and sulfate depletion point

The slope of silicate peak and sulfate depletion point have a moderate correlation for LC<sup>3</sup> pastes including constant added gypsum content (2%) provided that the pastes prepared with and without superplasticizer are considered separately (Figure 3.8). When a differentiation was not made with respect to superplasticizer content and all data was considered as one group,  $R^2$  decreased to 0.47. Also, variations in added gypsum content were not considered in this figure (3.8) due to much higher influence of increasing sulfate content on the aluminate peak compared to its influence on the silicate peak, which was discussed in the previous section 3.5.3.

Based on the results presented previously, a causality between these two heat flow parameters was anticipated especially when variations in the limestone particle size are considered. For example, the filler effect of L3 increased the slope of silicate peak due to accelerated formation of C-S-H, which resulted in earlier sulfate depletion point (Table 3.5). Similarly, increasing MK fraction at constant limestone particle size and w/s (Figure 3.3) increases the fineness of the system, corresponding to higher slope of silicate peak and thus earlier sulfate depletion point. However, this relationship is limited for other compositional variables such as w/s. As discussed in Section 3.5.4, in this case the sulfate depletion point may be modified through the variations in C<sub>3</sub>A reaction kinetics, not because of higher or lower C-S-H formation. Another reason pertaining to the limitations of this relationship is the adsorption of sulfate ions on metakaolin particles, which modifies the sulfate depletion point independent of the changes in the slope of silicate peak. Overall, it is understood that the causality between slope of silicate peak and sulfate depletion point is not global but rather limited to the filler effect by limestone or metakaolin in LC<sup>3</sup> systems.



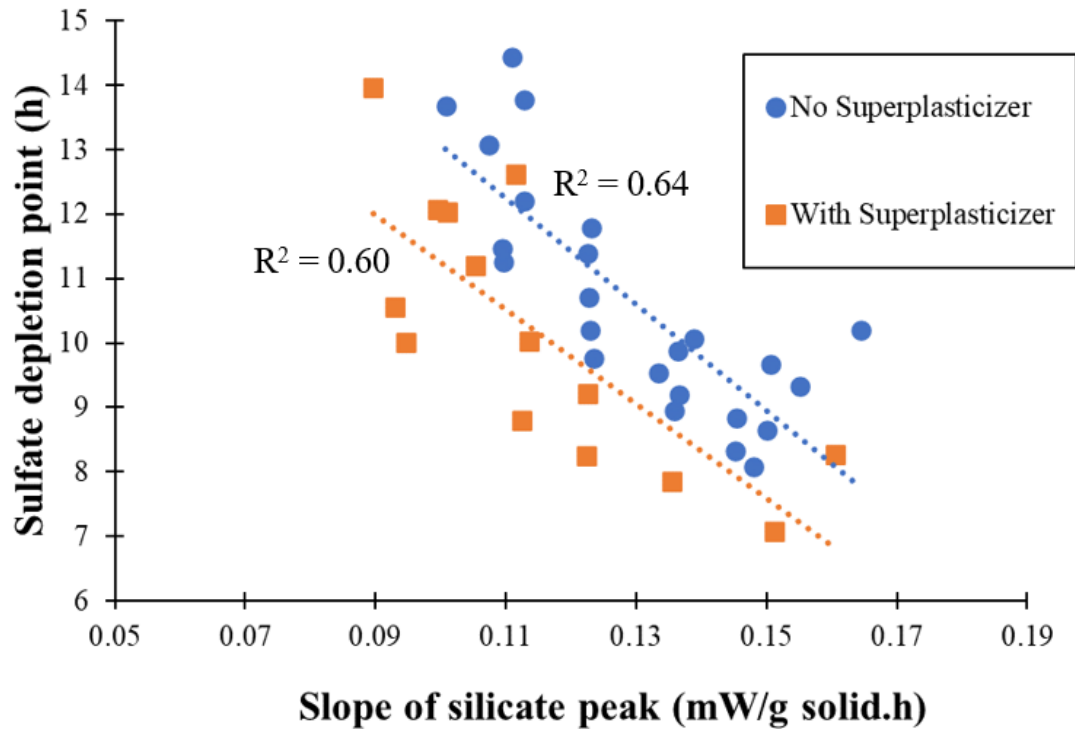


**Figure 3.8 – Relationship between the slope of silicate peak and sulfate depletion point with and without superplasticizer for LC<sup>3</sup> pastes including constant added gypsum content 2%.**

### 3.5.7 *In-situ XRD to understand the sulfate balance*

Two LC<sup>3</sup> systems shown in Figures 3.9 and 3.10 were chosen to track the differences in the evolution of hydrated phases caused by adding extra gypsum and to observe the sulfate balance period from the perspective of microstructural development. In both systems, ettringite forms rapidly at the beginning of hydration (Figure 3.9 and 3.10) similar to other studies. While a significant growth of ettringite peak could not be observed without extra gypsum, ettringite forms continuously in the presence of extra gypsum. The reason ettringite peak intensity could not grow in the absence of gypsum is the undersulfation. When the system is undersulfated (Figure 3.9a and 3.10a), increasing C-S-H precipitation via the hydration of C<sub>3</sub>S does not translate to later ettringite precipitation

like in a properly sulfated system because the amount of sulfates adsorbed by C-S-H is mediated by the initial concentration of sulfate ions in the pore solution [106]. An undersulfated system does not contain enough sulfates – limited to PC here (Table 3.2) - to be adsorbed which then can be released from C-S-H to contribute to ettringite precipitation after sulfate depletion point. This can be confirmed by increasing portlandite peak intensity, an indicator of increasing C-S-H precipitation through the hydration of  $C_3S$ , while the ettringite peak intensity is not significantly changing. Moreover, hemicarboaluminate peak intensity increases after the peak heat release in the acceleration period when the ettringite peak intensity plateaus out [30].

On the other hand, ettringite precipitates continuously in the presence of gypsum while hemicarboaluminate could not be identified in the first 24 h of hydration (Figure 3.9b and 3.10b). Remarkably, gypsum is not completely consumed in the 55:22.5:22.5 paste including 5% added gypsum even after the sulfate depletion point. Instead, gypsum depletion point is noted where the rate of increase in ettringite peak intensity significantly slows down. For instance, until the sulfate depletion point ettringite peak intensity increases by 130%, whereas after the sulfate depletion point it increases only by 13%. Similarly, the peak intensity of gypsum decreases by 61% until the sulfate depletion point and then it decreases by 32%. Sulfate balance period (between the maximum of silicate peak and sulfate depletion point) can then be summarized as a phase where ettringite precipitation is still favored. This also means that the longer the sulfate balance the longer it takes to form carboaluminate phases.

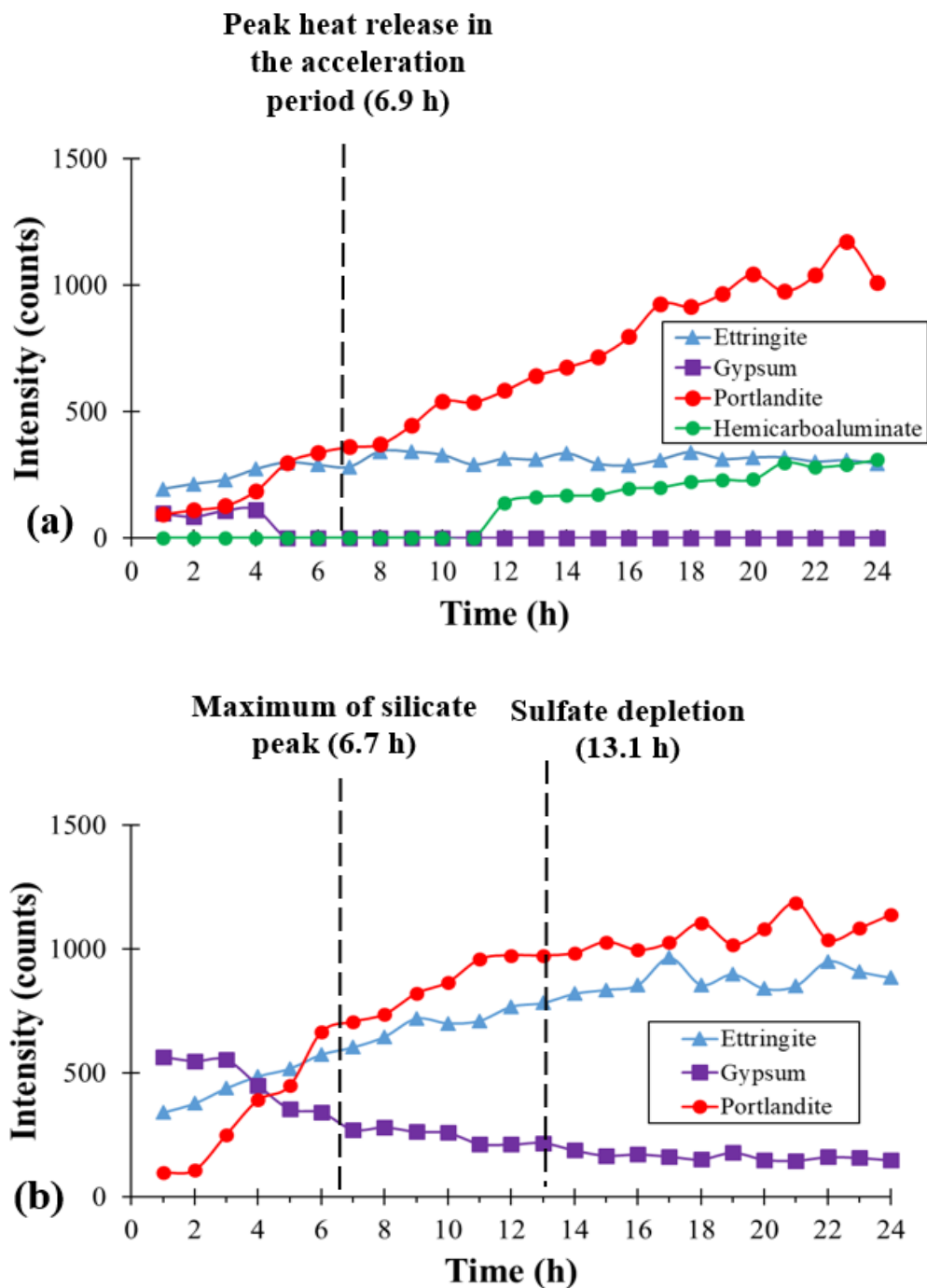


**Figure 3.9 - Evolution of hydrated phases identified in the 55:22.5:22.5 pastes including L3 by in-situ XRD: (a) 0% added gypsum, (b) 5% added gypsum. These**

pastes were prepared at w/s of 0.4 and contain 0.5% superplasticizer by mass of solid.

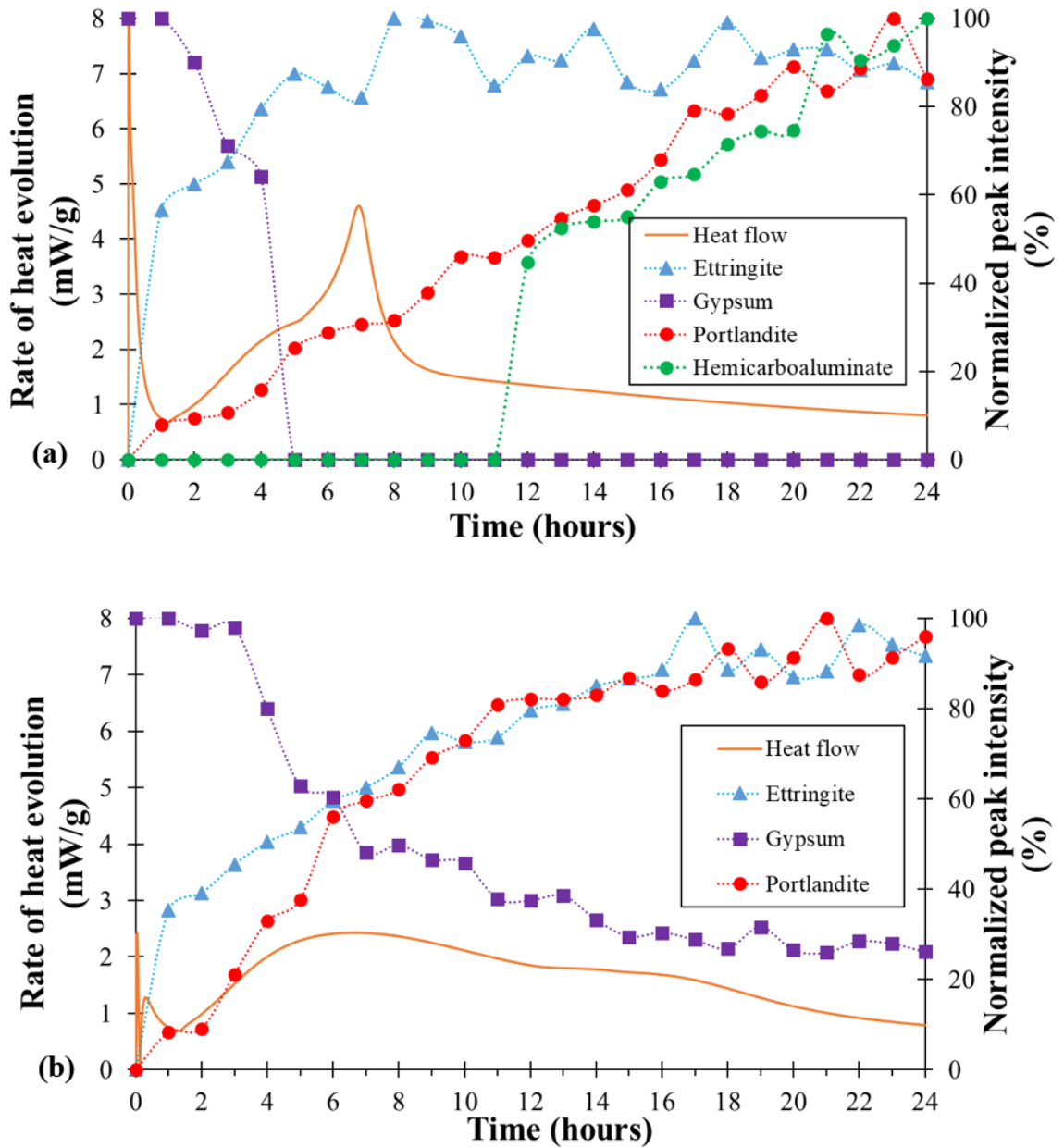
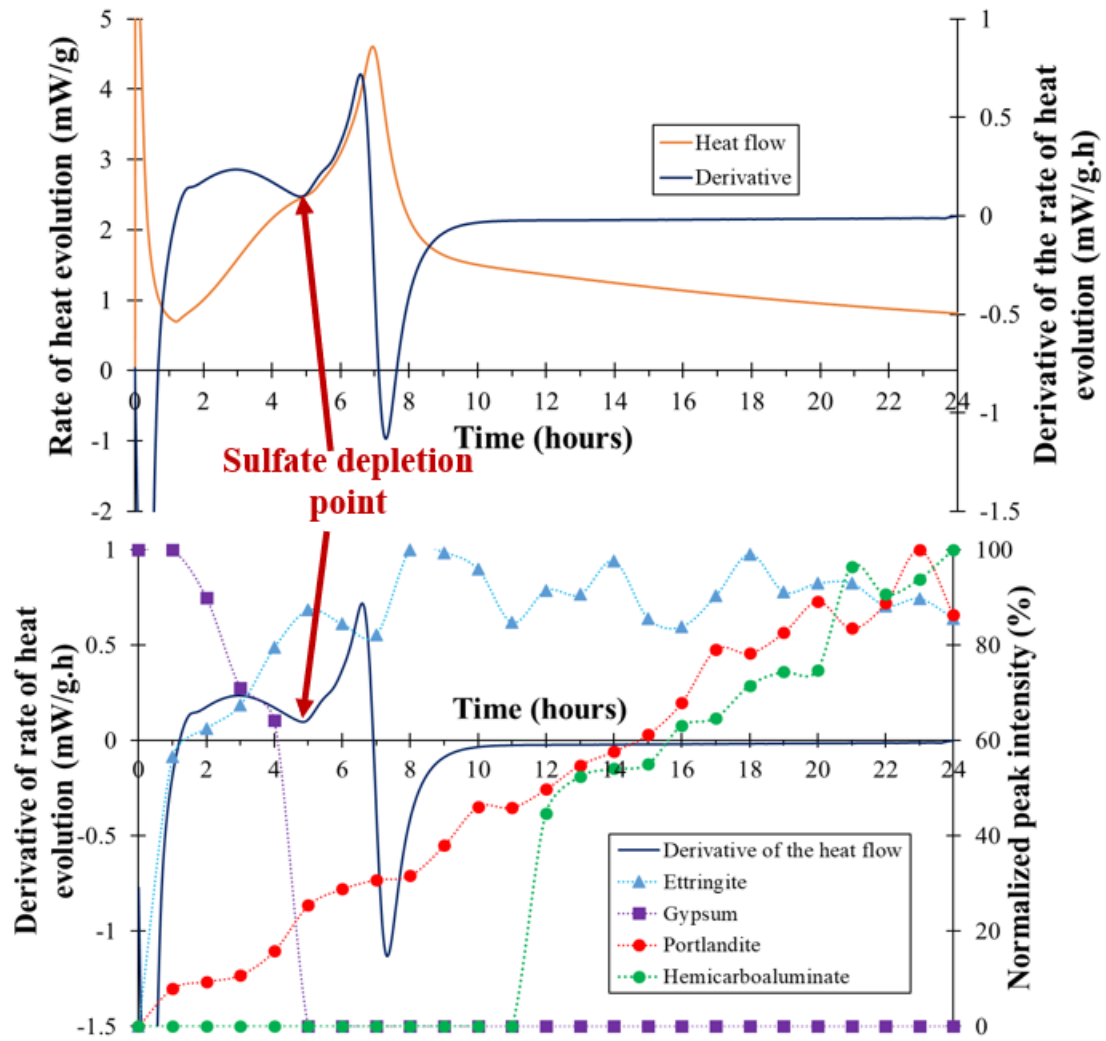


Figure 3.10 – Heat evolution and in-situ XRD results of the 55:22.5:22.5 pastes including L3: (a) 0% added gypsum, (b) 5% added gypsum. These pastes were prepared at w/s of 0.4 and contain 0.5% superplasticizer by mass of solid.

### 3.6 Identification of the sulfate depletion point in undersulfated LC<sup>3</sup> systems

The NW kernel estimator is a promising technique also to estimate the sulfate depletion point of the undersulfated systems where the aluminate and silicate peaks overlap. Figure 3.11 shows that sulfate depletion point can be distinguished at where the derivative of the heat flow curve reaches a local minimum but not zero prior to the aluminate peak. This point is also associated with the consumption of gypsum in the LC<sup>3</sup> system. Further experiments should be performed with other cement binders to prove the validity of this approach to identify the sulfate depletion point in undersulfated systems.



**Figure 3.11 - The derivative of the heat evolution curve and in-situ XRD results of the 55:22.5:22.5 paste including L3 without added gypsum.**

### 3.7 Statistical Results

Satisfactory fits are observed with sulfate balance and cumulative heat evolution models with RMSE of 0.841 h and 2.877 J/g, respectively (Table 3.9 and Table 3.10). The only predictor not selected by the stepwise algorithm for sulfate balance is the superplasticizer content (Table 3.9). This supports the idea that (presented in Section 3.1.5) superplasticizer content is not a major player for LC<sup>3</sup> sulfate balance when varied from 0 to 0.5% by mass of solid compared to other compositional variations. Contrarily, it is the

most significant predictor for the cumulative heat evolved by 24 h (Table 3.10). According to this model the cumulative heat evolved by 24 h decreases with increasing superplasticizer content. This could be attributed to decreasing rate of precipitation of C-S-H (slope of silicate peak in Table 3.8) and the delay in hydration reactions caused by the steric hindrance of PCE molecules [105].

The most significant predictor for the sulfate balance of LC<sup>3</sup> is SO<sub>3</sub>, which was expected based on the results in Section 3.1.3. It is also a significant predictor for the cumulative heat as shown in Table 3.10. Based on these results, it is confirmed that optimizing the sulfate content in LC<sup>3</sup> is important not only for the sulfate balance but also for space-filling until 24 h with hydrated phases.

Sulfate balance of LC<sup>3</sup> is also significantly influenced by the metakaolin fraction, solid volume concentration and the fineness of limestone particles. Table 3.9 suggests that increasing solid volume concentration (decreasing w/s) and metakaolin fraction decreases the sulfate balance of LC<sup>3</sup>. The sulfate balance increases significantly with increasing APS – which means decreasing fineness. Among these variables, only metakaolin fraction is not considered as a significant predictor for the cumulative heat, likely because of the trends observed with mixes including superplasticizers (Table 3.4).

Overall, it is recommended to consider relatively higher amounts of extra gypsum for mixtures including high metakaolin fractions because of the capability of metakaolin to bind sulfates. In the mix design of LC<sup>3</sup> it should also be kept in mind that increasing metakaolin fraction does not significantly increase the total amount of hydrated phases formed until 24 h, especially in the presence of superplasticizer (Section 3.1.1). To increase

the total amount of hydrated phases by 24 h, using finer limestone particle size or optimizing the sulfate content should be considered for a given water content.

**Table 3.9 - The stepwise regression model variables, standardized coefficients, and p-values for the sulfate balance ( $R^2 = 0.811$  and RMSE = 0.841 h)**

Model variables	Standardized coefficient	p-value
$\Phi$	-1.2	$1.3 \times 10^{-9}$
MK	-0.8	$1.9 \times 10^{-7}$
APS	0.3	$7.1 \times 10^{-3}$
SO <sub>3</sub>	2.1	$3.6 \times 10^{-15}$

**Table 3.10 - The stepwise regression model variables, standardized coefficients, and p-values for the cumulative heat evolved by 24 h ( $R^2 = 0.907$ , RMSE = 2.877 J/g)**

Model variables	Standardized coefficient	p-value
SP	-5.7	$3.9 \times 10^{-5}$
$\Phi$	-4.7	$4.0 \times 10^{-4}$
APS	-2.5	$6.6 \times 10^{-7}$
SO <sub>3</sub>	2.1	$1.7 \times 10^{-4}$

### 3.8 Conclusions

Composition versus sulfate balance linkages for LC<sup>3</sup> was investigated in this study. The effects of various compositional-modifications originating from the changes in PC:MK:LS, limestone particle size, added gypsum content, w/s and superplasticizer content were quantified. Metakaolin fraction, particularly, is not a trivial factor for the sulfate balance of LC<sup>3</sup> because it also mediates the extent of the influence of other compositional variables such as limestone particle size. A methodology based on Kernel regression was used to parametrize the heat evolution curves focusing on the determination of slope of silicate



peak, the time of maximum of silicate peak and the sulfate depletion point. This methodology also appeared promising to identify the sulfate depletion point in undersulfated systems where the aluminate and silicate peaks overlap. In-situ XRD helped to differentiate the phase evolution of undersulfated and properly sulfated systems. To compare the relative importances of the compositional predictors on the sulfate balance, stepwise regression was performed, which suggested that metakaolin fraction is a significant factor for the sulfate balance of  $LC^3$  but not for the cumulative heat evolved by 24h. Some key conclusions can be summarized as follows:

- Sulfate balance of  $LC^3$  decreases with increasing metakaolin fractions. This could be explained by the tendency of sulfate ions to adsorb on metakaolin particles. Therefore, required amount of added gypsum increases with increasing metakaolin fractions to satisfy the sulfate demand.
- Using fine limestone particle size (L3) decreases the sulfate balance of  $LC^3$ . This effect is strongest in mixes including highest limestone content (55:15:30). Also, incorporation of L3 results in relatively stronger increases in the cumulative heat evolved by 24 h in the presence of superplasticizer due to the better dispersion of fine limestone particles.
- Added gypsum amount has the strongest influence on the sulfate balance of  $LC^3$ , because increasing sulfate content greatly retards the aluminate reaction.
- Increasing w/s increases the sulfate balance of  $LC^3$ , which might be due to delayed reaction of  $C_3A$ . It also increases the cumulative heat evolved by 24 h. This rate of increase is the highest for pastes including lowest metakaolin (55:15:30) because

increasing metakaolin content corresponds with increasing flocculation and therefore more entrapped water unavailable for hydration.

- Variations in the superplasticizer dosage from 0 to 0.5% is not as significant as other compositional variables investigated for the sulfate balance of LC<sup>3</sup>. However, it is the most significant predictor for the cumulative heat evolved by 24 h.
- Sulfate balance period is accompanied by increasing ettringite and portlandite content. Sulfate depletion point corresponds to a notable decrease in the rate of ettringite precipitation and does not always mean that gypsum is completely consumed.

## **CHAPTER 4.     STRUCTURE-PROPERTY RELATIONSHIP FOR LC<sup>3</sup> RHEOLOGY**

### **4.1   Introduction**

Among the alternative cementitious materials compositions, limestone calcined clay cements (LC<sup>3</sup>) are identified as one of the most promising alternatives to portland cement (PC). LC<sup>3</sup> can be readily produced globally and can halve the CO<sub>2</sub> emissions compared with PC production, while offering excellent mechanical and durability performance [8, 13, 34]. LC<sup>3</sup> is a ternary binder most commonly composed of 50% PC clinker, 30% calcined clay, 15% limestone and 5% gypsum, by mass [13, 60]. However, LC<sup>3</sup> binders can suffer from poor flowability and premature setting due to the highly reactive nature and fineness of the calcined clay [77]. As a result, challenges with workability can limit their translation into the concrete industry.

While concrete workability in the field is most often characterized through slump of fresh concrete [28], rheological measurements can offer more descriptive performance metrics which can be related to field performance. For example, ASTM C1749 [71] defines the yield stress, measured in Pascal (Pa), as the stress required to initiate flow, which can be measured via rheometer. In practice, yield stress is of paramount importance during casting as it determines if fresh concrete can fill the formwork under an applied shear stress. Plastic viscosity, on the other hand, dictates the time it takes to fill the formwork during flow [107].

Calcined clay characteristics are dominant factors affecting the rheological properties of cementitious binders incorporating them - such as LC<sup>3</sup> - due to their highly

reactive nature, high surface area and high surface charge density (e.g., zeta potential) [73, 74, 81, 108]. These largely depend on the kaolinite content of the calcined clay. For example, Lorentz et al. [81] showed that the kaolinite content in the clay source, which transforms to metakaolin when calcined at 600-800 °C, is directly proportional to the zeta potential of PC-calcined clay binary systems, which is then highly correlated to the yield stress ( $R^2 = 0.9149$ ) and plastic viscosity ( $R^2 = 0.876$ ). A similar relationship was observed by Hou et al. [73] for three ternary cementitious binders containing PC, calcined clay and limestone at different ratios, including LC<sup>3</sup> proportions. The authors found a strong relationship between the zeta potential and yield stress for all formulations examined.

However, LC<sup>3</sup> composition can be modified not only by calcined clay content but also by varying the particle sizes of the constituent materials, the rate of gypsum addition and the water content. In multi-component mineral systems, like LC<sup>3</sup>, zeta potential can be complicated to predict *a priori* since calcined clays are net negatively charged and PC and limestone are net positively charged. However, the physical packing and particle size distributions of the LC<sup>3</sup> binder constituents also greatly influence yield stress and viscosity [75]. While identifying a single force, such as zeta potential, that determines the yield stress and plastic viscosity forms the basis for a simplified design principle, the properties of LC<sup>3</sup> appear to be driven by a broader range of forces and interactions, thus creating a multi-dimensional problem in materials design.

## **4.2 Research Significance**

This research addresses the challenge of predicting yield stress and plastic viscosity for LC<sup>3</sup> using a Machine Learning (ML) model with a set of diverse compositional

variables that represent the changes in water-to-solid ratio (w/s), constituent mass ratios (PC:Metakaolin:Limestone), limestone particle size and gypsum content while quantifying the relative importance of these variables. It is hypothesized that ML can lead to high fidelity in the yield stress and plastic viscosity predictions while bringing new understanding about composition-rheology linkages, which can be useful for the mixture design of LC<sup>3</sup>.

Moreover, this research also addresses developing a methodology to parametrize the hydration kinetics that was shown to correlate with the yield stress of cementitious materials [109, 110]. This methodology is based on kernel smoothing method applied on the heat flow data obtained from calorimetric measurements. The motivation of this effort is to investigate whether the rate of heat release at the onset of acceleration period can be used to estimate the yield stress measured during the induction period, while decoupling the hydration kinetics effects from the yield stress. Accordingly, varying significance of the compositional variables on hydration kinetics and yield stress is demonstrated that can be considered toward optimizing the mixture formulations for LC<sup>3</sup>.

## **4.3 Experimental**

### *4.3.1 Materials*

PC, metakaolin, three limestone powders and gypsum used for this study were introduced in previous chapter (Section 3.3.1).

### *4.3.2 Mix design*

To understand the linkages between cement composition and rheological parameters, LC<sup>3</sup> compositional variables were modified in the mix design (Table 4.1), including PC:MK:LS, water-to-solid ratio (w/s), limestone particle size, and added gypsum level (wt.% of binder). This experimental design was motivated by the purpose of covering a wide range of solid volume fraction – altered mainly by w/s – while also decoupling the significance of the gypsum dosage on the rheological properties of LC<sup>3</sup>, which has been shown to mediate the early silicate and aluminate reactivity (e.g., avoiding flash set) [30]. Accordingly, each of the PC:MK:LS pastes were prepared with six w/s (0.55, 0.60, 0.65, 0.70, 0.75 and 0.80) and three limestone particle sizes (L3, L15, L25) with a constant added gypsum dosage of 2%, by mass. In addition, the influence of added gypsum content on the yield stress and plastic viscosity was investigated only on 55:30:15, including L15 by varying gypsum dosages as 0%, 2%, 5% and 7% at a constant w/s of 0.75. In total, this experimental design corresponds to 57 pastes. However, some mixes could not be tested due to their stiffness, such as some mixes prepared with 55:30:15 using w/s of 0.55 and 0.60 (see the footnote under Table 4.1). Therefore, the total number of measured data are fewer (i.e., 48 pastes).

Samples are identified by abbreviations defining these varying compositional parameters, as: PC:MK:LS-w/s-LS size-added gypsum %. For example, a sample identified as “55:30:15-0.70-L25-G5” represents a paste that was prepared using PC:MK:LS at mass ratio of 55:30:15 including L25 as the limestone size and 5% added gypsum (by mass of solids) and mixed at w/s of 0.70. No superplasticizer was used in this research to avoid its impact on the rheological properties and to focus on the influence of

compositional variables. Deionized water with a resistivity of 18.2 MΩ was utilized for all mixes.

**Table 4.1 - Experimental matrix**

<b>PC:MK:LS</b>	<b>Water-to-solid ratio (w/s)</b>	<b>Limestone particle size</b>	<b>Added gypsum (wt. %)</b>
55:30:15*	0.55, 0.60, 0.65, 0.70, 0.75, 0.80	L3, L15, L25	0, 2, 5, 7
55:22.5:22.5**	0.55, 0.60, 0.65, 0.70, 0.75, 0.80	L3, L15, L25	2
55:15:30	0.55, 0.60, 0.65, 0.70, 0.75, 0.80	L3, L15, L25	2

\* 55:30:15 pastes prepared with w/s of 0.55 and 0.60 could not be tested at any limestone particle size and added gypsum content due to the great stiffness of pastes. In addition, 55:30:15 could not be tested at w/s of 0.65 and 0.70 only when L3 was used.

\*\* 55:22.5:22.5 could not be tested only at w/s of 0.55 when L3 was included.

#### *4.3.3 Tests and Analytical Methods*

To achieve a consistent shearing history among pastes tested with the rheometer and calorimeter, a constant mixing procedure was applied on the pastes containing predetermined amount of solids (300 g) mixed with various water contents that were determined according to the mix design (Table 4.1). Cement paste samples for each experiment were prepared using a 5-speed high shear blender. The mixing procedure was adapted from [92, 93] and can be summarized as follows: Only solids (PC+MK+LS+gypsum) were mixed for 30 s at low speed to achieve homogenization and then water was added. After, the paste was mixed for 30 s at low speed and then 60 s at medium setting. The paste was allowed to rest for 90 s and then the mixing was finalized with an additional 60 s medium-speed mixing.

For the rheological characterization, strain-controlled flow curve experiments were conducted with Anton Paar MCR102 at 23 °C. A helical stirrer measuring system (double helical spiral, ST24-2HR-37/120) was utilized. Selection of the measuring system was motivated by [111], which suggests that slippage and sedimentation can be avoided using a helical stirrer. The rheological protocol to calculate the dynamic yield stress and plastic viscosity was inspired by [74]. Accordingly, the paste was first pre-sheared from 0 to 100 s<sup>-1</sup> for 60 seconds to obtain a reference flocculation stage [112], followed by 30 seconds resting period and then a three step measurement protocol was applied that consists of: shearing from 0 to 100 s<sup>-1</sup>, rest for 5 s at 100 s<sup>-1</sup>, and then shearing back to 0 s<sup>-1</sup>. As specified in ASTM C1749 [71], each reading was recorded either when the torque is stable or after 20 s while the paste have been continuously being stirred, and at least five readings – as required by [71] - were taken in both the ascending and descending ramps. The (dynamic) yield stress and plastic viscosity were calculated from the descending shear stress versus shear strain flow curves based on the Bingham rheological model (Equation 4.1), as suggested in literature for LC<sup>3</sup> [9,10].

$$\tau = \tau_0 + \eta \dot{\gamma} \quad (4.1)$$

In Equation 1,  $\tau$  is the shear stress (Pa),  $\tau_0$  is the yield stress (Pa),  $\eta$  is the plastic viscosity (Pa.s) and  $\dot{\gamma}$  is the shear rate (1/s). Any nonlinearity may imply shear thickening or shear-thinning, but neither was observed.

All rheological measurements were completed within the first 30 minutes of hydration thus so-called “the induction or dormant period”, where the rheological properties are governed by the initial interparticle forces [113] along with C-S-H nucleation



creating a network between cement particles in both PC and LC<sup>3</sup> systems [73, 114]. The flow curve experiments were performed at least twice to ensure reproducibility, and the average values were reported as the yield stress and plastic viscosity.

Heat evolution of blended cement pastes was measured using an isothermal calorimeter (TAM Air, TA Instruments). Accordingly, 10 g of paste samples were prepared outside the calorimeter at room temperature (23±2 °C) and then loaded into the calorimeter. Among the pastes tested with the rheometer and calorimeter, calorimetry was performed only the pastes prepared using w/s of 0.65 and 0.75. Because the effects of all compositional variables on the yield stress including added gypsum level could be evaluated at w/s of 0.75, it was selected for testing with calorimeter. Pastes were also tested with w/s of 0.65 to assess the influence of w/s on each PC:MK:LS. Two replicates were prepared for each paste. Rate of heat evolution and cumulative heat evolution of cement pastes, normalized to total solid content, were assessed at 23 °C for 2 days.

## **4.4 Computational Methods**

### *4.4.1 Machine learning approach*

To build an accurate ML model for yield stress and plastic viscosity, LC<sup>3</sup> composition needs to be represented comprehensively by various predictor variables based on constituent materials with various size and reactivity. This premise is reinforced by the findings from [108] that recently showed the inability of single physical parameters to explain solely the rheological properties of PC-calcined clay binders. Therefore, an assemblage of variables has been defined. Accordingly, five predictors were defined herein for the Machine Learning model:

- $\text{Al}_2\text{O}_3/\text{SO}_3$  (%) of total cementitious solid (by mass percentage) based on XRF (Table 3.2),
- Volumetric proportion of MK/LS (Equation 4.2),
- Solid volume concentration (shown as  $\Phi$  in Equation 4.3),
- Estimated total particle density (number/100  $\mu\text{m}^3$ ) representing the total number of cementitious particles per unit volume of the binder (abbreviated as TPD in Equation 4.4) according to [115], and
- Packing index (K), obtained from the compressible packing model [116].

The predictor  $\text{Al}_2\text{O}_3/\text{SO}_3$  (%) represents the sulfate balance of the system, which was defined based on the findings from [117] that showed variations in the yield stress of PC-calcined clay binders with different addition rates of gypsum. It is based on mass percentage because in literature the gypsum addition rates for LC<sup>3</sup> have been typically determined on a mass basis [30, 33, 41].

The variable (MK/LS) was introduced with the purpose of capturing the yield stress and plastic viscosity differences stemming from the proportionality between metakaolin and limestone, which have opposite impacts on the adhesive properties [74]. Equation 4.2 defines MK/LS based on the masses (m) of the constituents and their specific gravities (SG):

$$\frac{\text{MK}}{\text{LS}} = \frac{m_{\text{MK}}/\text{SG}_{\text{MK}}}{m_{\text{LS}}/\text{SG}_{\text{LS}}} \quad (4.2)$$

A volumetric proportion was chosen, instead of mass, to compare the importance of this variable with solid volume concentration.

The solid volume concentration ( $\Phi$ ) and the total particle density (TPD) were incorporated into the model as they have been understood to be of paramount importance for mediating the extent of particle-particle interactions. Consequently, they govern the early yield stress of cementitious materials [114, 118]. TPD was estimated based on  $\Phi$  and average particle size ( $d$ ) of the mineral components (Table 3.1).

$$\Phi = \left(1 + \frac{(SG_{OPC} \times m_{OPC} + SG_{MK} \times m_{MK} + SG_{LS} \times m_{LS} + SG_G \times m_G) \times w/s}{SG_W}\right)^{-1} \quad (4.3)$$

$$TPD = \Phi \times d^{-3} = \Phi \times (\phi_{OPC} \times d_{OPC} + \phi_{MK} \times d_{MK} + \phi_{LS} \times d_{LS})^{-3} \quad (4.4)$$

Finally,  $K$  was used to represent the packing of each mixture, which influences the rheology of cementitious materials [75, 119, 120].  $K$  is a unitless parameter, and it was used to represent initial (unhydrated) particle packing in the ML model. It was calculated according to Equation 4.5 as a function of volume of each grain class ( $y_i$ ), packing density of each class ( $\beta_i$ ), virtual packing density of each grain class ( $\gamma_i$ ) and  $\Phi$  [120]:

$$K = \sum_{i=1}^n \frac{y_i/\beta_i}{\frac{1}{\Phi} - \frac{1}{\gamma_i}} \quad (4.5)$$

In calculations,  $\beta_i$  was kept constant at 0.74 [121]. Accordingly, a higher  $K$  corresponds with a stiffer mixture [116, 119, 122, 123]. A Python script was used to calculate the value of  $K$  [119, 122], which varied with respect to changes in  $w/s$ , PC:MK:LS

and limestone particle size. The influence of added gypsum content - from 0 to 7% - on packing and TPD were neglected owing to its relatively low proportion (variation in  $\Phi < 1\%$  by added gypsum) and chemical significance rather than contribution to packing for LC<sup>3</sup> [30, 33, 41, 86].

To quantify the relative importance of these five predictors for the rheological properties of LC<sup>3</sup>, stepwise linear regression was implemented. In estimating the amount of information loss by a model, the stepwise algorithm deals with the trade-off between the fitting of training dataset and the complexity of the model. This algorithm performs a greedy search over candidate models to make feature selection while trying to minimize the information loss, in other words, AIC criterion (Eq. 4.6) [97]:

$$AIC = n \log \sum_{i=1}^n (Y_i^{actual} - Y_i^{model})^2 - n \log n + 2k \quad (4.6)$$

After determining the significant predictors for the LC<sup>3</sup> yield stress and plastic viscosity based on the stepwise regression, a Support Vector Regression (SVR) model was built using gaussian kernel, which maps the data to an infinite-dimensional space to make accurate predictions (Eq. 4.7). The choice of SVR was motivated by its ability to capture nonlinearity while achieving excellent generalizability [124]. The cost (C) and gamma ( $\gamma$ ) hyperparameters were tuned with cross-validation on the training set to avoid overfitting. Also, to overcome overfitting only the statistically significant predictors identified by stepwise regression were used in the SVR model. RMSE was reported as the SVR model performance based on the testing set. It should be noted that prior to building stepwise regression and SVR models, all variables were standardized to achieve comparable scales,

meaning that each data point was subtracted from its mean and divided by its standard deviation.

$$K(x, x') = \exp(-\gamma \|x - x'\|^2) \quad (4.7)$$

The original dataset of 48 yield stress and plastic viscosity observations (i.e., the response variable) was split to training (75%) and testing (25%) sets. Using Monte Carlo Cross-Validation algorithm with 100 computations, the model performance metric root mean squared error (RMSE) (Eq. 3.3) was calculated from the average of the 100 computations.

Recently, the predictive capability of SVR algorithm for predicting the compressive strength of concrete and the hydration product stiffness was demonstrated in [125] and [126], respectively. These references also provide an overview about machine learning algorithms, including SVR, which the reader is referred to for further detail on this methodology.

#### 4.4.2 *Kernel smoothing for isothermal calorimetry data*

Recently, it was shown [110] that the yield stress of cement pastes can be related to their time-dependent heat flow, measured by isothermal calorimetry. Mantellato et al. [110] demonstrated that the yield stress of PC pastes is nearly constant during the induction period but exponentially increases during the acceleration period which is associated with an increase in the rate of heat release. The moment of this transition from the induction period to the acceleration period is called the “onset of acceleration.” This moment of transition was also observed in [127], where this feature was attributed to the initial setting

time of the PC studied. Because of these observed correlations between yield stress and heat release in PC, in this research it is hypothesized that the initial yield stress of LC<sup>3</sup>, a PC-based binder, measured prior to acceleration period can be estimated by the heat release at the onset of acceleration period. This heat release will be referred as “onset heat”, and its time of occurrence will be referred as “onset time”.

However, the variability in duration of the induction period of plain cement pastes (i.e., those not including any retarders or superplasticizers) is quite narrow due to the stagnant chemical reactivity of the system [128], and the exact time when the acceleration begins is not easy to define precisely. For instance, the approach in [110] required time-dependent spread diameter measurements in addition to calorimetry data to estimate the onset heat. The authors did not attempt to identify the onset heat only from the calorimeter data because it could not be distinguished from the portlandite precipitation around the onset time, which was observed as a small hump.

To simplify the experimental approach (avoiding time-dependent spread diameter measurements) for identifying the onset heat and onset time, this research proposes a kernel smoothing method to determine these parameters only based on calorimetry data. The approach uses the Nadaraya-Watson estimator (NW) [97], which enables derivatives to be calculated. This is helpful for assessing time-dependent change, such as in calorimetry. The NW predictions of the heat flow for the first 24 hours of hydration were constructed following the methodology described in previous chapter.

From the time derivatives of the NW heat flow predictions, the onset time was considered as the earliest time when the time derivative equals zero before the acceleration

starts (Figure 4.1). The onset heat is the (measured) rate of heat release corresponding to this onset time. A small hump related to portlandite precipitation can be distinguished as a spike in the time derivative data [129] around the onset, but this feature was not observed in any of the LC<sup>3</sup> formulations tested. Based on two replicates for each mixture, averages of the onset heat and onset time were reported. Considering all the mixtures, the RMSE of heat flow predictions by the NW was found to be less than 0.82 mW/g. The coefficients of variation for the onset heat and onset time were less than 6.9% and 4.9%, respectively.

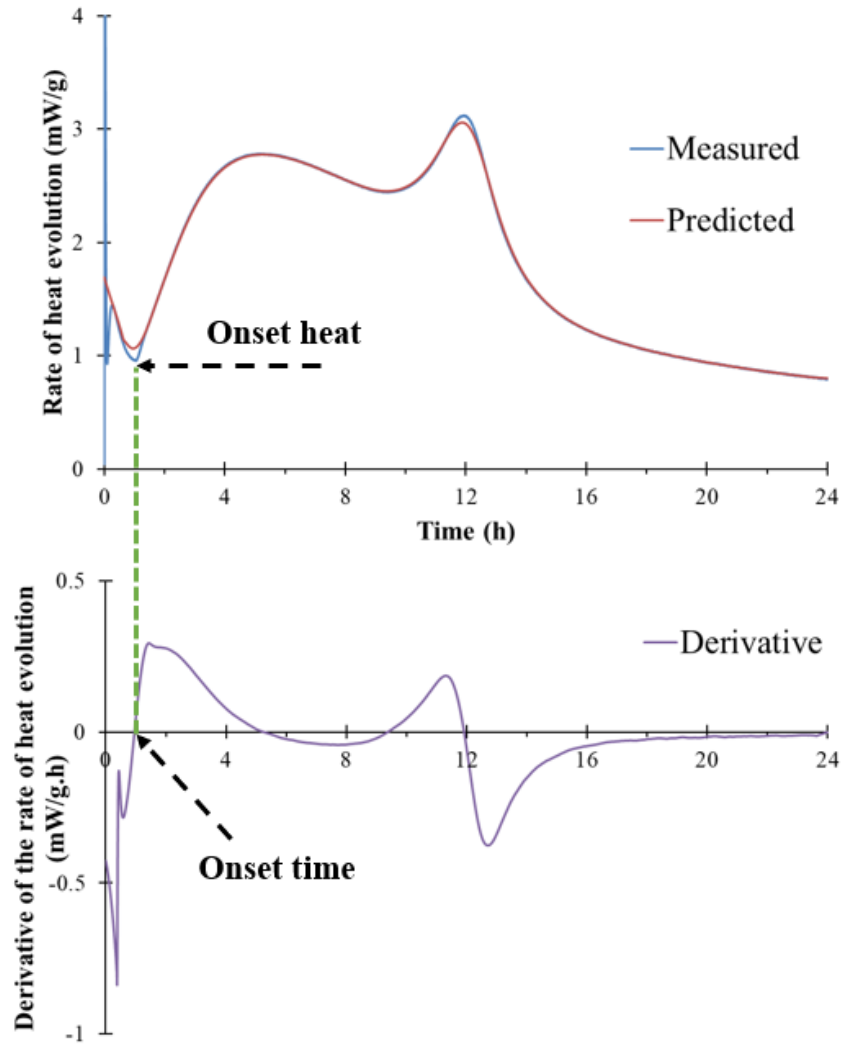


**Figure 4.1 - Illustration of the Nadaraya-Watson kernel estimate used to predict the heat flow parameters for 55:22.5:22.5-0.75-L3-G2 such as rate of heat release during the induction period. Top figure shows the predicted heat flow, and the bottom figure shows the time derivative of the heat flow.**

#### **4.5 Results and Discussion**

Composition versus yield stress and plastic viscosity linkages were established for each compositional variable investigated (i.e., PC:MK:LS, limestone particle size, w/s, added gypsum content). Significant variables related to composition were identified through a stepwise regression algorithm, and then the yield stress and plastic viscosity were



modeled with SVR. The influence of the LC<sup>3</sup> composition on the hydration kinetics was explored through the variations in the onset heat, which was determined via the NW kernel smoothing method, as previously described. The correlation between the onset heat and the yield stress of LC<sup>3</sup> are established; those results and limitations in this correlation will be discussed herein.

#### *4.5.1 Composition- rheology linkages*

##### 4.5.1.1 Solid volume concentration

The influence of compositional variables on the rheological properties of LC<sup>3</sup> can be examined in Figure 4.2, showing the relationship between the solid volume concentration and the yield stress (Figure 4.2a) and the plastic viscosity (Figure 4.2b). Red dashed circle on Figure 4.2 indicates the pastes including L15 with varying added gypsum content. Conventionally, yield stress and viscosity increase with solid volume concentration, not only for cement suspensions but also for other suspensions composed of alumina and chocolate, for example [130-133]. Likewise, here, yield stress and plastic viscosity increase with decreasing w/s, for each PC:MK:LS examined at a given limestone particle size. These paste yield stresses and plastic viscosities range from 41 Pa to 799 Pa and from 0.1 Pa.s to 3.3 Pa.s, respectively. The only exception to this trend is the 3% higher yield stress – within the standard deviation – achieved with 55:22.5:22.5 including L25 at w/s of 0.60 (solid volume concentration of ~0.37) than the yield stress of the same formulation prepared with w/s of 0.55 (solid volume concentration of ~0.39).

Moreover, at constant solid volume concentrations, a higher yield stress and plastic viscosity are observed with finer limestone (L3), compared to L15 or L25. Remarkably,

the greater yield stress and plastic viscosity measured in systems incorporating higher metakaolin contents can be counteracted by using a coarser limestone particle size. For instance, at constant w/s of 0.75 (solid volume concentration of  $\sim 0.32$ ), the LC<sup>3</sup> formulation with the lowest MK content (55:15:30) but including the finest limestone (L3) achieves 27% higher yield stress and 29% plastic viscosity than a higher MK mix, with coarser limestone (i.e., 55:22.5:22.5 including L25). This emphasizes the interplay between various compositional parameters, which complicates the predictions of rheological parameters for LC<sup>3</sup>.

While the rheological properties of PC-based blends such as PC-fly ash or PC-limestone binders are well-predicted with one compositional variable such as particle number density [113, 133], predicting the yield stress or plastic viscosity of LC<sup>3</sup> successfully with a similar approach is not possible. The complex mineral components of LC<sup>3</sup> with their disparate characteristics complicate the intuitive development of such relationships [74, 133]. This challenge motivates the data analytics approach (discussed Section 4.5.2), which uses a multitude of compositional variables in predicting the rheological properties of LC<sup>3</sup>.

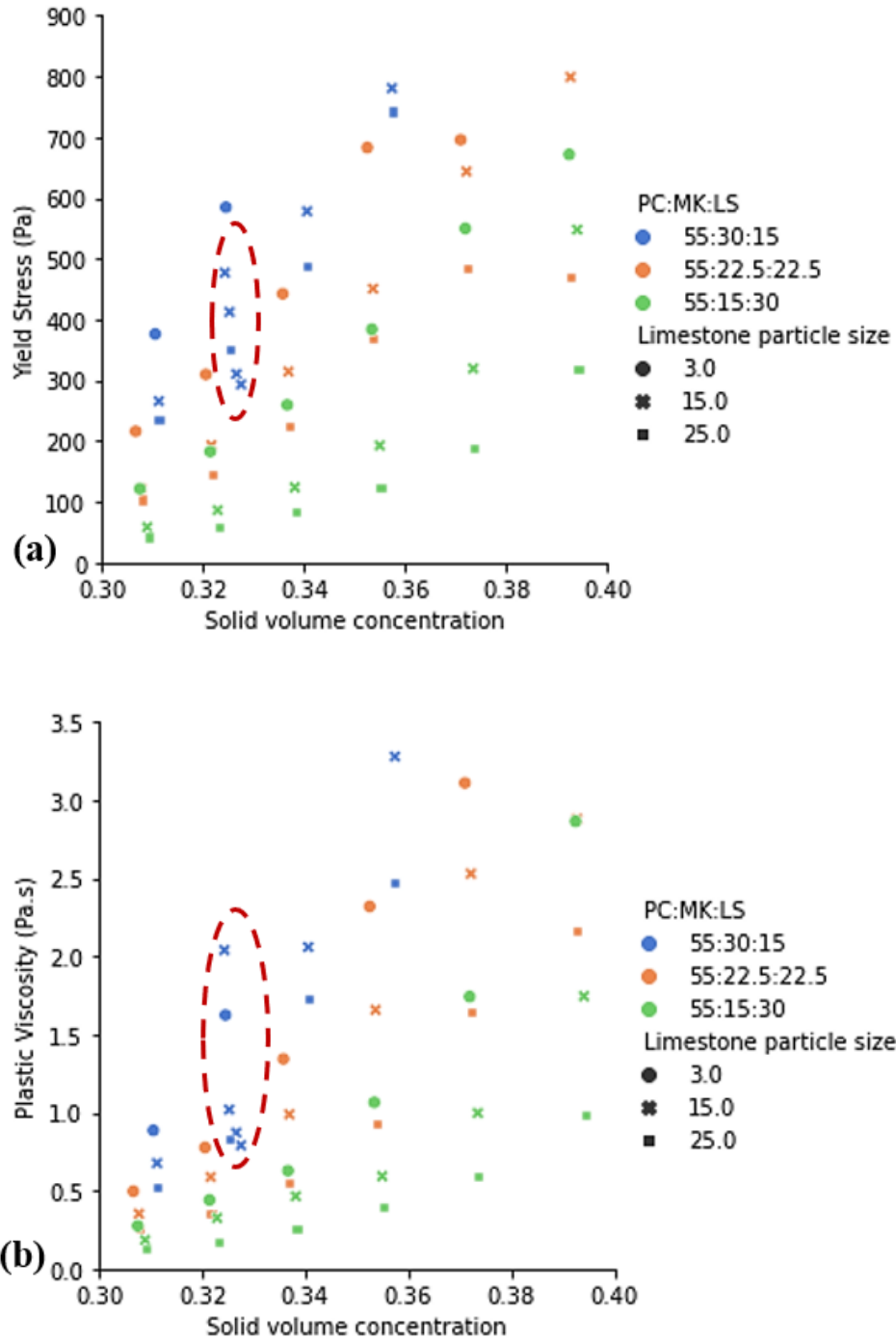


**Figure 4.2 - Relationship between the solid volume concentration and the yield stress (a) and plastic viscosity (b) of LC<sup>3</sup> formulations. Varying PC:MK:LS and limestone particle sizes are represented with different colors and marker styles. The influence of the added gypsum content on the yield stress and plastic viscosity of 55:30:15 including L15 is indicated by the red dashed circle.**

#### 4.5.1.2 Importance of metakaolin content

As expected, the metakaolin fraction in the LC<sup>3</sup> formulation has a significant influence on the yield stress and plastic viscosity. At constant w/s, increasing metakaolin fraction results in greater yield stresses and plastic viscosities (Figure 4.3). For instance, at a constant w/s of 0.70 (solid volume concentration of ~0.34) and constant limestone particle size of L15, the yield stress of the 55:30:15 paste is 578 Pa, which is 84% higher than 55:22.5:22.5 and 367% higher than 55:15:30. Even larger increases in yield stress with increasing MK fraction are observed at higher w/s. For example, for w/s of 0.75, the yield stress of the 55:30:15 paste is 412 Pa, or 114% higher than that of 55:22.5:22.5. In fact, this effect of MK content on yield stress is greatest for the highest w/s investigated (0.80) with a 119% increase compared with 55:22.5:22.5 at that w/s. However, this trend for yield stress was not systematic with other limestone particle sizes (i.e., L3 or L25) and for plastic viscosity.

The influence of the metakaolin fraction on yield stress at these relatively higher w/s may be due to the variations in zeta potential of the system, which is dominated by the calcined kaolinite content in LC<sup>3</sup> systems [73]. On the other hand, interparticle contacts, another main driving force for the yield stress, diminish with increasing water content due to increasing distance between particles. To examine trends with interparticle contact, Table 4.2 summarizes packing index for each paste and shows a decreasing packing index with increasing w/s. Therefore, the role of electrostatic interactions on LC<sup>3</sup> yield stress could be more significant at relatively higher w/s than it was at relatively lower w/s, where yield stress is likely to be governed more by the interparticle contacts [132]. In the context of the ML model presented in this study, this hypothesis implies increasing significance of the MK/LS with increasing water content.

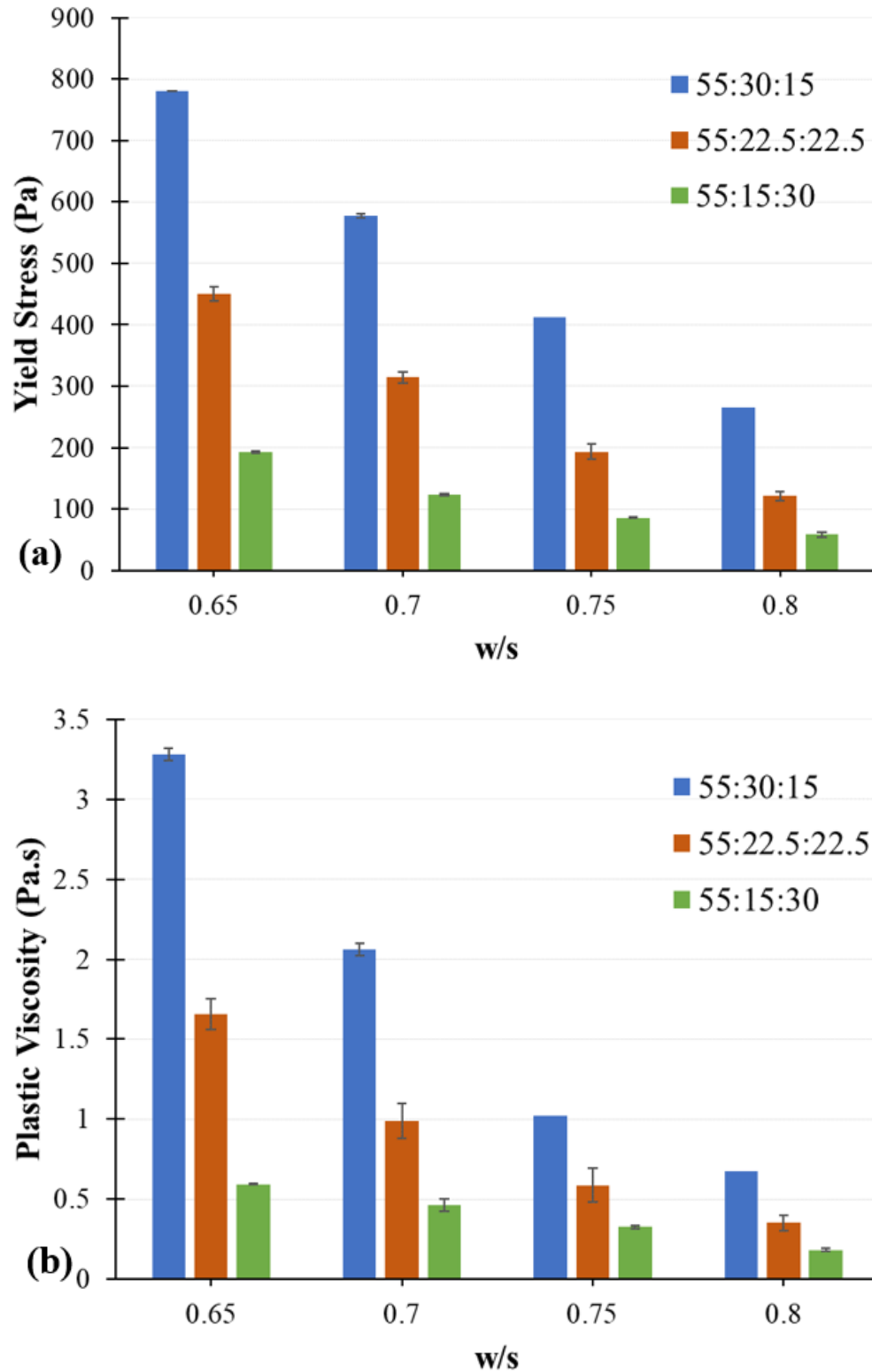


**Figure 4.3 - Influence of the metakaolin fraction on the yield stress (a), and plastic viscosity (b) of LC<sup>3</sup> pastes at different w/s ratios. Limestone particle size (L15) and**

added gypsum content (2% by mass of total solid) are constant in these pastes.  
Error bars indicate one standard deviation measured for each formulation.

**Table 4.2 - Packing indexes (K) calculated for LC<sup>3</sup> pastes with varying PC:MK:LS at different w/s ratios.**

PC:MK:LS	Limestone particle size	Added gypsum (wt. %)	w/s	K
55:30:15	L15	2	0.65	0.82
55:22.5:22.5	L15	2	0.65	0.83
55:15:30	L15	2	0.65	0.84
55:30:15	L15	2	0.70	0.75
55:22.5:22.5	L15	2	0.70	0.76
55:15:30	L15	2	0.70	0.77
55:30:15	L15	2	0.75	0.70
55:22.5:22.5	L15	2	0.75	0.71
55:15:30	L15	2	0.75	0.72
55:30:15	L15	2	0.80	0.65
55:22.5:22.5	L15	2	0.80	0.66
55:15:30	L15	2	0.80	0.67

#### 4.5.1.3 Importance of limestone particle size

Yield stress and plastic viscosity increase with decreasing limestone particle size, when other compositional variables, such as added gypsum content and w/s, are constant. That is, for each PC:MK:LS, LC<sup>3</sup> yield stress and plastic viscosity values follow this trend: L3 > L15 > L25 (Figure 4.4). Intuitively, this is related to increased packing due to the ‘filler effect,’ induced by substituting larger cement grains with smaller and substantially less reactive L3 [9, 26]. However, when the K values (Table 4.3) are compared, it is

observed that the variations in yield stress with limestone particle size ( $> 42\%$ ) and in plastic viscosity ( $> 32\%$ ) are much greater than the variations in  $K$  ( $< 6\%$ ), suggesting that a different mechanism than packing – the fineness or surface area of the limestone – also plays a role in determining the rheological properties.

Another key observation from Table 4.3 is slightly higher  $K$  is achieved with L15, compared to L3 and L25, for a constant PC:MK:LS. Nevertheless, the yield stress and plastic viscosity are higher for each paste composition when L3 is used, relative to these parameters for pastes containing L15 or L25. This trend suggests that the impact of increasing fineness prevails over changes in packing, for a given water content and paste composition. This relationship agrees with other studies that relate the higher yield stresses and plastic viscosities achieved with finer particles to increasing specific surface area and water demand of the system, dominating the influence of packing [85, 113, 133, 134].

It is also worth noting that the increase in the yield stress when L3 substitutes for L15 or L25 is stronger for mixes incorporating relatively higher limestone contents. To illustrate, at w/s of 0.75, the 55:30:15 paste including L3 achieves a 585 Pa yield stress, which is 42% higher than the same paste with L15 and 67% higher than the one with L25. On the other hand, at a higher limestone content paste with 55:22.5:22.5 proportionality, the yield stress is 310 Pa with L3, which is 60% higher than L15 and 115% higher than L25. In the paste with the highest limestone fraction (i.e., 55:15:30) with L3, the yield stress is 112% and 214% higher than with L15 and L25, respectively. The increasingly higher yield stresses achieved with L3 in comparison to L15 and L25 with increasing limestone content suggests that the extent of the effect of the limestone particle size on the

yield stress is mediated by its content and is more pronounced for higher limestone formulations.

The joint influence of limestone content and particle size observed for the yield stress is not effective for the plastic viscosity. For instance, the 55:30:15 paste including L3 at w/s of 0.75 achieves a 1.6 Pa.s plastic viscosity, which is 60% higher than the one with L15. However, in the paste with the highest limestone content (55:15:30), L3 achieves only 38% higher plastic viscosity than L15. Therefore, it can be concluded that while the MK/LS and limestone particle size can jointly influence the yield stress, this combined effect does not exist for the plastic viscosity.



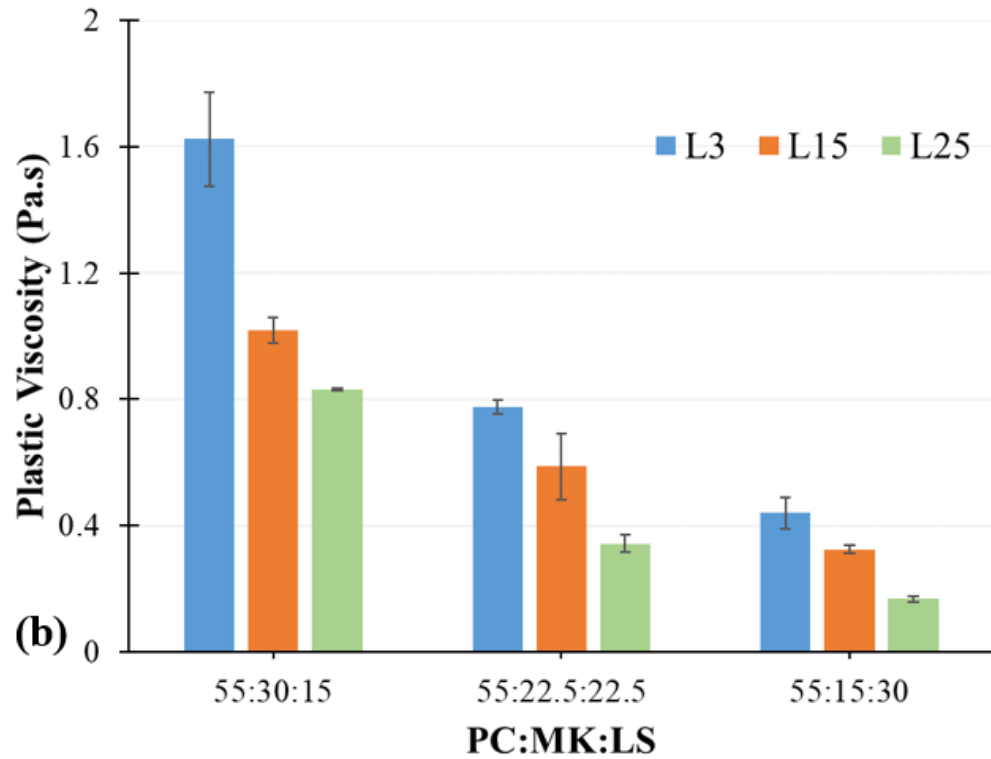
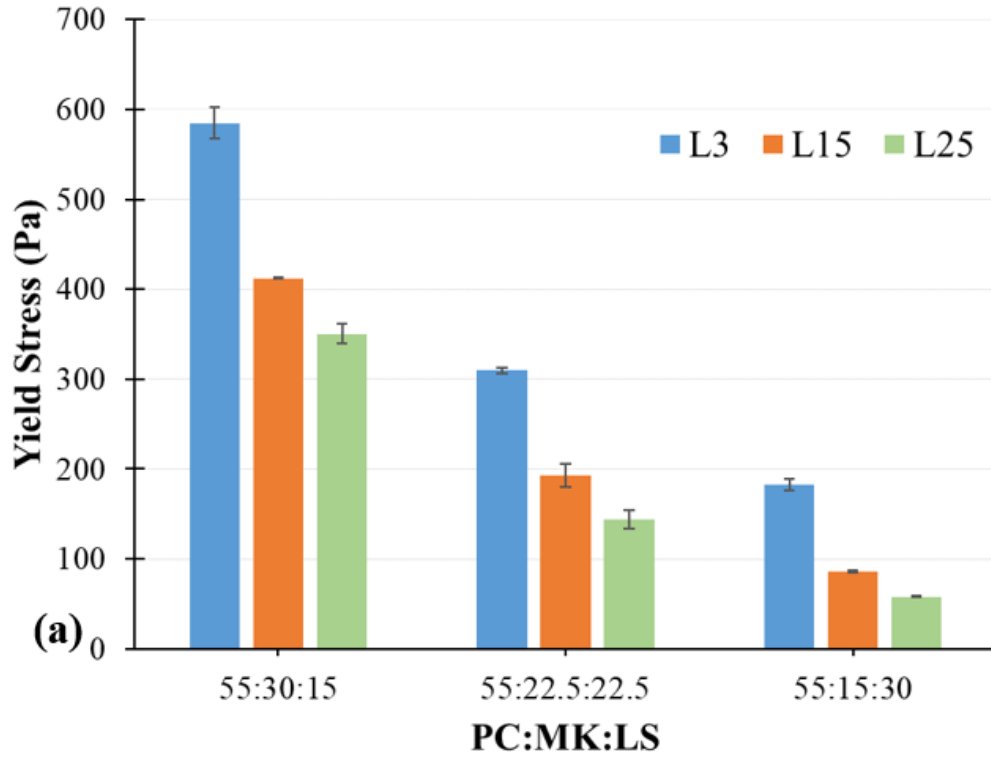


**Figure 4.4 - Influence of the limestone particle size on the yield stress (a) and plastic viscosity (b) of LC<sup>3</sup> pastes with varying PC:MK:LS. These pastes were prepared at**

constant w/s of 0.75. Error bars indicate one standard deviation measured for each formulation.

**Table 4.3 - Packing indexes (K) calculated for LC<sup>3</sup> pastes influenced by PC:MK:LS and limestone particle size at constant w/s of 0.75.**

PC:MK:LS	Limestone particle size	Added gypsum (wt. %)	w/s	K
55:30:15	L3	2	0.75	0.69
55:30:15	L15	2	0.75	0.70
55:30:15	L25	2	0.75	0.68
55:22.5:22.5	L3	2	0.75	0.69
55:22.5:22.5	L15	2	0.75	0.71
55:22.5:22.5	L25	2	0.75	0.68
55:15:30	L3	2	0.75	0.68
55:15:30	L15	2	0.75	0.72
55:15:30	L25	2	0.75	0.69

#### 4.5.1.4 Importance of added gypsum content

Figure 4.5 shows that the added gypsum content is a major determinant of LC<sup>3</sup> yield stress and plastic viscosity. Notwithstanding the early age of hydration; the effect of gypsum on the rheological properties of LC<sup>3</sup> has not been previously examined. Yield stress and plastic viscosity decrease with increasing gypsum content, from 0 to 5% added gypsum. These results are statistically significant, since both the yield stress and plastic viscosity differences are outside the standard deviation range. For instance, when no gypsum is added, the yield stress of the 55:30:15 paste including L15 at w/s of 0.75 is 477 Pa, which is 54% higher than that achieved with 5% added gypsum. However, increasing

the added gypsum content from 5% to 7% does not create a statistically significant difference – within the standard deviation – on the yield stress.

This effect of the added gypsum on the rheological properties of LC<sup>3</sup> can be explained by the influence of gypsum on early hydration. First, there is a minor effect of decreasing PC and metakaolin fractions. More importantly, the early reaction of alumina from metakaolin and calcium aluminate phases present in PC (such as C<sub>3</sub>A) are more controlled in the presence of gypsum. These reactions lead to ettringite precipitation instead of rapid formation of calcium aluminate hydrates, which occurs when there is not enough gypsum in the system [30, 86]. It should be noted that the plastic viscosity is more sensitive to the changes in added gypsum content than the yield stress. For instance, increasing the added gypsum content from 0 to 5% decreases the plastic viscosity 57%, whereas the yield stress decreases by 35%. The diminishing effect observed with further additions of gypsum (i.e., beyond 5% by mass) on both the yield stress and plastic viscosity implies that this optimal sulfate balance is reached at approximately 5% added gypsum content, for the LC<sup>3</sup> systems examined. However, for Al<sub>2</sub>O<sub>3</sub>/SO<sub>3</sub> between 11% and 4%, yield stress and plastic viscosity of LC<sup>3</sup> vary significantly.

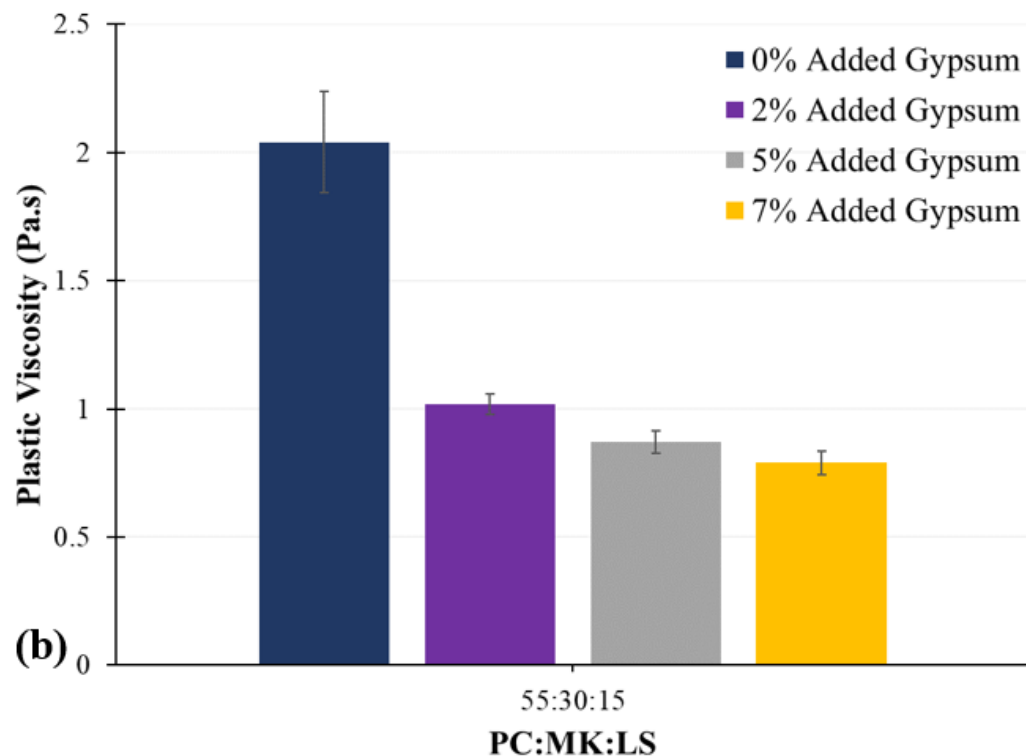
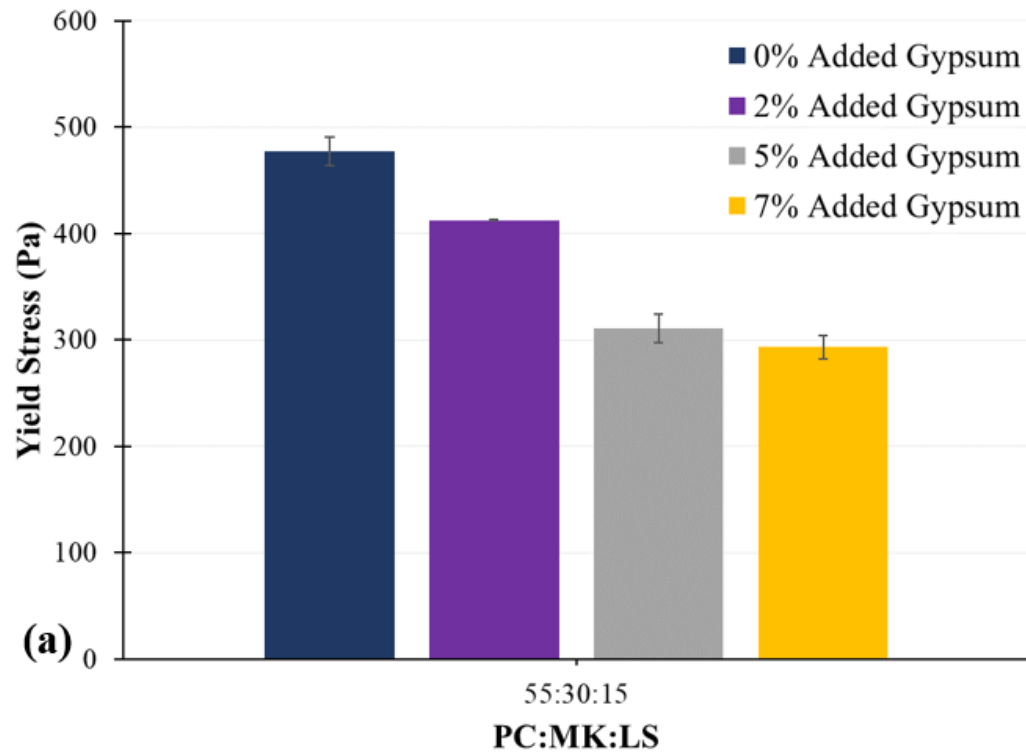


**Figure 4.5 - Influence of the added gypsum content on the yield stress (a) and plastic viscosity (b) of 55:30:15 including L15. These pastes were prepared at constant w/s of 0.75. Error bars indicate one standard deviation measured for each formulation.**

#### 4.5.2 Statistical Analysis and Modelling Results

The stepwise regression algorithm is preferred for this investigation because it can perform variable selection and can produce interpretable models [97]. Stepwise regression predicted the yield stress and plastic viscosity with RMSE of 97.66 Pa and 0.472 Pa.s, respectively. Using the variables chosen by the stepwise regression, SVR significantly improved the accuracy and predicted these properties on testing set with RMSE of 59.14 Pa and 0.278 Pa.s, respectively. By achieving significantly better accuracy with this machine learning model, the importance of SVR to make accurate predictions for LC<sup>3</sup> rheological properties is evident.

The regression models demonstrate that both the yield stress and plastic viscosity of LC<sup>3</sup> increases with increasing packing index (K), Al<sub>2</sub>O<sub>3</sub>/SO<sub>3</sub>, total number of particles per unit volume of the binder (TPD). However, solid volume concentration is not chosen by the algorithm. This demonstrates that solid volume concentration alone is an oversimplified representation of the microstructure. Because solid volume concentration does not account for variations in the solid skeleton originating from the various sizes and reactivity of mineral components, the complexities in the mineral system most influencing yield stress are not considered in simplified approaches relying on quantifications of solid content alone.

It should be noted that variations in w/s did produce a wide range in packing indices for the LC<sup>3</sup> formulations examined. These were calculated to be between 0.63 and 1.02, with relatively more dilute pastes characterized by lower K [120]. However, for a given w/s, K differs only up to 6% with different limestone particle sizes or PC:MK:LS, as

illustrated in Table 4.3. The ML model specifies that to modify the yield stress for a given water content, LC<sup>3</sup> composition should be varied by its TPD, Al<sub>2</sub>O<sub>3</sub>/SO<sub>3</sub> and/or MK/LS.

Both LC<sup>3</sup> paste yield stress and plastic viscosity increase with increasing K, Al<sub>2</sub>O<sub>3</sub>/SO<sub>3</sub> and TPD (Table 4.4 and 4.5). The most significant variable affecting both properties is K, deduced from its highest standardized coefficient. Packing index K increases with decreasing w/s, resulting in stiffer pastes with higher yield stress and plastic viscosity. The reason for the solids fraction not being selected by the models can be explained by its inability to represent the variations in the solid skeleton, which derive from the various sizes and reactivity of mineral components present in LC<sup>3</sup>. However, the variations in rheological properties for a given water content could not be explained by K because it varied only up to 6% by various LS particle sizes and PC:MK:LS. These variations could be captured, instead, by other model variables such as Al<sub>2</sub>O<sub>3</sub>/SO<sub>3</sub> and TPD, which increase with increasing MK fraction and LS fineness. On the other hand, decreases in yield stress and plastic viscosity achieved with increasing gypsum may be due to improvements in the sulfate balance of the system (i.e., decreasing Al<sub>2</sub>O<sub>3</sub>/SO<sub>3</sub>), avoiding the rapid precipitation of calcium aluminate hydrates. This ML models elucidates the diversity of mechanisms through which the MK component dominates the rheological behavior of LC<sup>3</sup>, both directly and through its interactions with the other mineral constituents.

**Table 4.4 - The selected model variables, standardized coefficients, and p-values for yield stress**

<b>Model variables</b>	<b>Standardized coefficient</b>	<b>p-value</b>
K	163.7	$7.2 \times 10^{-15}$
Al <sub>2</sub> O <sub>3</sub> /SO <sub>3</sub>	89.5	0.01
TPD	81.2	$1.0 \times 10^{-6}$
MK/LS	68.8	0.01

**Table 4.5 - The selected model variables, standardized coefficients, and p-values for plastic viscosity**

<b>Model variables</b>	<b>Standardized coefficient</b>	<b>p-value</b>
K	0.7	$1.9 \times 10^{-11}$
Al <sub>2</sub> O <sub>3</sub> /SO <sub>3</sub>	0.6	$3.3 \times 10^{-7}$
TPD	0.3	$5 \times 10^{-4}$

#### *4.5.3 Relationship between heat release and yield stress*

To further explore the mechanisms relating LC<sup>3</sup> composition to yield stress, calorimetry was performed on the same paste compositions. Relationships between composition and onset heat and onset time, as described in Section 4.4.2, are examined. Different from [110], where yield stress evolution of PC-based pastes over a period of time was correlated to their time-dependent heat flow, this study focuses on the relationship between the onset heat at the end of the dormant period and the initial yield stress within the dormant period.

##### 4.5.3.1 Composition-onset heat linkages

Increasing metakaolin fraction increases the onset heat (Figure 4.6a). This direct proportionality indicates intensified chemical reactivity, related to early formation of hydrated phases such as nanoscale C-(A)-S-H [21, 135, 136]. However, this effect of MK on the onset heat is not as pronounced as its effect on yield stress. To illustrate, increasing the metakaolin fraction from 15 to 30% by mass in the w/s of 0.65 LC<sup>3</sup> formulation corresponds to a maximum increase of ~19% in the onset heat, whereas the yield stress increases by ~305%. As discussed previously (Section 4.5.1.2), flocculation with increasing metakaolin evidently has greater influence on the yield stress than the onset heat.

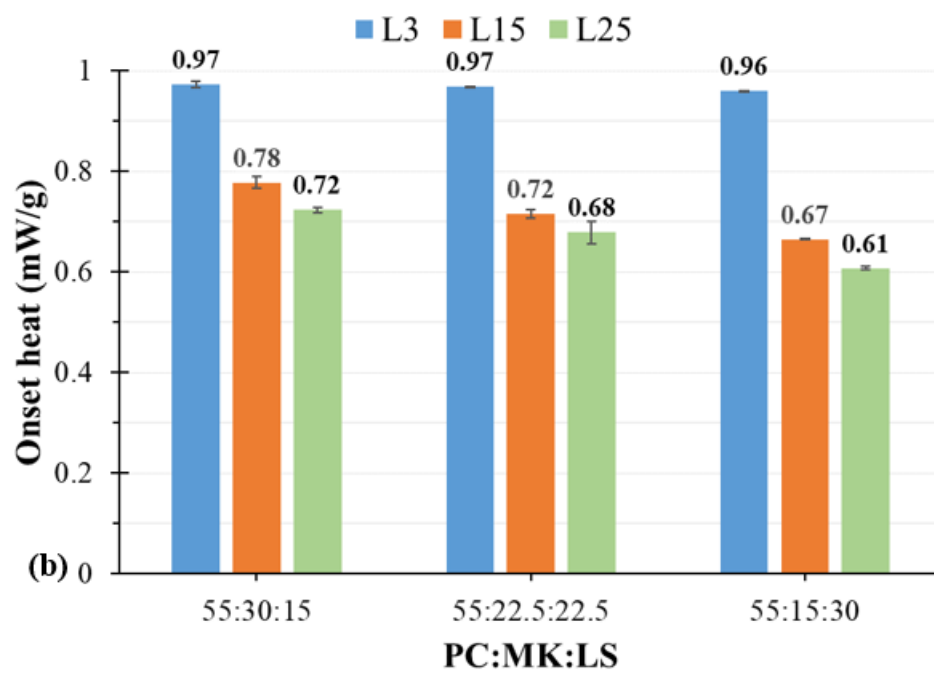
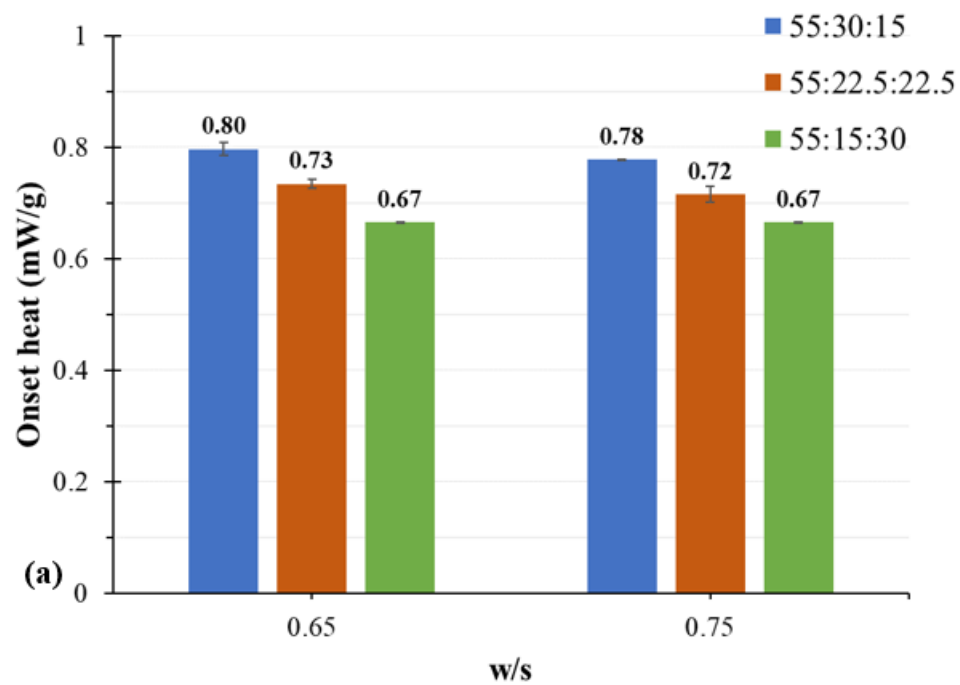
Conversely, variation in w/s between 0.65 and 0.75 did not influence the onset heat, particularly in comparison to changes in the yield stress. For instance, decreasing w/s from 0.75 to 0.65 does not bring about a significant change in the onset heat of 55:15:30, whereas the yield stress is enhanced by ~123%. A reduction in water content translates to a higher K (Table 4.2), which is the most significant variable identified by the stepwise model for LC<sup>3</sup> yield stress. Therefore, these results show that LC<sup>3</sup> packing within w/s range between 0.65 and 0.75 does not strongly relate to onset heat.

However, incorporating a finer limestone particle size (L3) greatly increases the onset heat, as observed from Figure 4.6b. This is likely due to the accelerated and enhanced nucleation of hydration products on the additional surface area provided [9, 26]. This increase in the onset heat by replacing L25 with L3 is the greatest (~57%) for the paste with the highest limestone fraction, 55:15:30, showing similar dependency on limestone content observed with the yield stress (Section 4.5.1.3). Furthermore, among all compositional modifications considered in Figure 4.6, the onset heat is most impacted by



the incorporation of L3, producing increases of ~35% to ~57% compared to mixtures with L15 or L25 (for all proportions, w/s, and gypsum content), suggesting the significance of accelerated early product nucleation on onset heat. This is supported by the relationship in Figure 4.7, where an excellent linear fit ( $R^2$  of 0.916) is found between the estimated TPD and the onset heat.

Increasing gypsum addition produced decreases in the onset heat, ranging from ~3% to ~18% with increasing additions of gypsum up to 7% by mass (Figure 4.6c). The effect on onset heat occurs to a relatively lesser extent than the similar trend for changes in yield stress (which ranged from ~14% to ~39%). These results also contrasts with the findings from [33] that demonstrated increasing heat release around the onset time, with added gypsum for LC<sup>3</sup> pastes. However, diminishing heat release during the induction period by adding gypsum was observed for alite samples tested in the same research group [29]. On the basis of these observations, it is proposed that decreasing PC content, thus decreasing alite, and metakaolin fractions with increasing added gypsum content in the binder results in less chemical reactivity during the induction period for the LC<sup>3</sup> pastes. The discrepancy between these results and those from [33] could be due to the differences in PC and gypsum compositions, and the w/s used. Therefore, further investigation is needed to reconcile these variations, but these results further highlight the complexities in the extension of working knowledge from PC directly to LC<sup>3</sup> systems, as well as the inherent increased complexity of LC<sup>3</sup> systems.



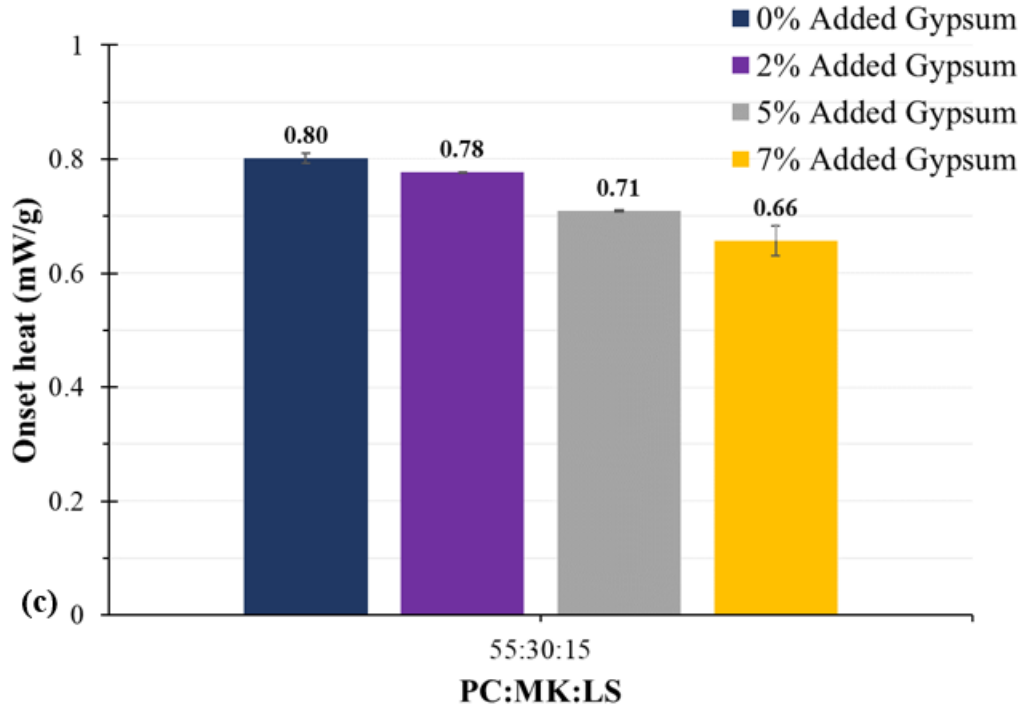


Figure 4.6 - (a) Influence of the PC:MK:LS on the onset heat of pastes including L15 and 2% added gypsum; (b) Influence of the limestone particle size on the onset heat of pastes with varying PC:MK:LS at w/s of 0.75; (c) Influence of the added gypsum content on the onset heat of 55:30:15 pastes including L15. Error bars indicate one standard deviation calculated for each formulation.

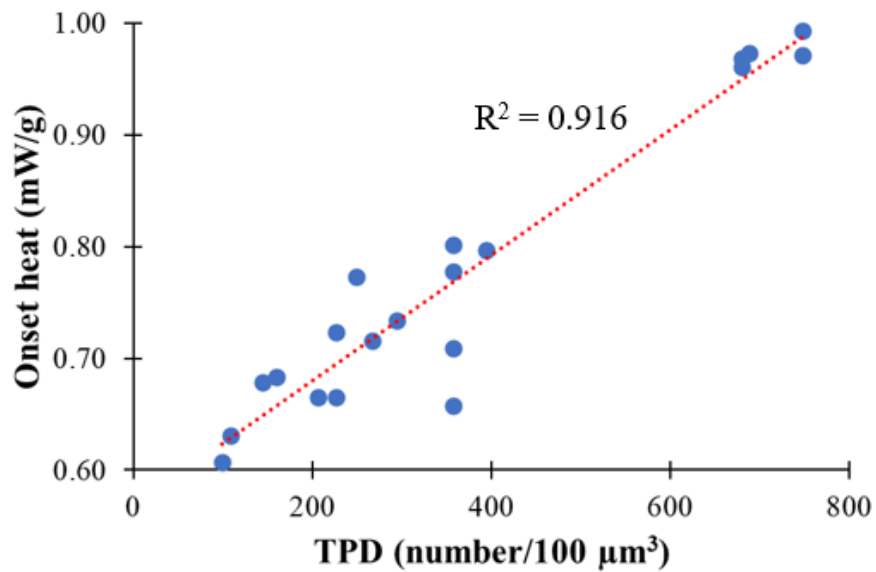


Figure 4.7 - Relationship between the estimated TPD and the onset heat for all pastes examined.

#### 4.5.3.2 Onset heat-yield stress linkages

Figure 4.8 shows a correlation between LC<sup>3</sup> yield stress and onset heat for pastes with L15 and L25, suggesting that the nucleation effect observed for the finest limestone particles (L3) significantly influences this relationship. That is, while no meaningful fit is found for all LC<sup>3</sup> pastes examined, a linear fit for LC<sup>3</sup> pastes including only the L15 and L25 limestones achieves an R<sup>2</sup> of 0.712. A separate linear fit with the LC<sup>3</sup> pastes including L3 achieves an R<sup>2</sup> of 0.809.

This difference between the two trends mainly results from the greater impact on the onset heat by the acceleratory and nucleation effect of L3, as discussed previously in Section 4.5.3.1. However, the influence of limestone particle size is less on the yield stress compared to onset heat. In the context of ML model, the extent of the L3 nucleation effect on LC<sup>3</sup> yield stress is proportional to the increase in TPD, which is only one of the four predictors identified by the stepwise regression (Table 4.4). However, variables other than limestone particle size that are relatively less impactful for onset heat can be relatively more impactful for LC<sup>3</sup> yield stress. For example, variations in the MK fraction influence yield stress by changing not only TPD, but also changing Al<sub>2</sub>O<sub>3</sub>/SO<sub>3</sub> and MK/LS. This can be further illustrated by considering the yield stress and onset heat variations observed in the 55:15:30 paste including L15, when L15 is replaced by L3 or when MK fraction is increased from 15% to 22.5% at w/s of 0.75. For instance, replacing L15 by L3 increases the onset heat and yield stress by 43% and 112%, respectively. However, when the MK fraction is increased from 15% to 22.5%, the yield stress increases by 124% where the onset heat increases only by 8%. Notably, this increase in yield stress is even more than the increase observed when replacing L25 by L3 associated with a much lower increase in

the onset heat. Thus, these observations demonstrate that yield stress is significantly more sensitive to variations in LC<sup>3</sup> composition than onset heat.

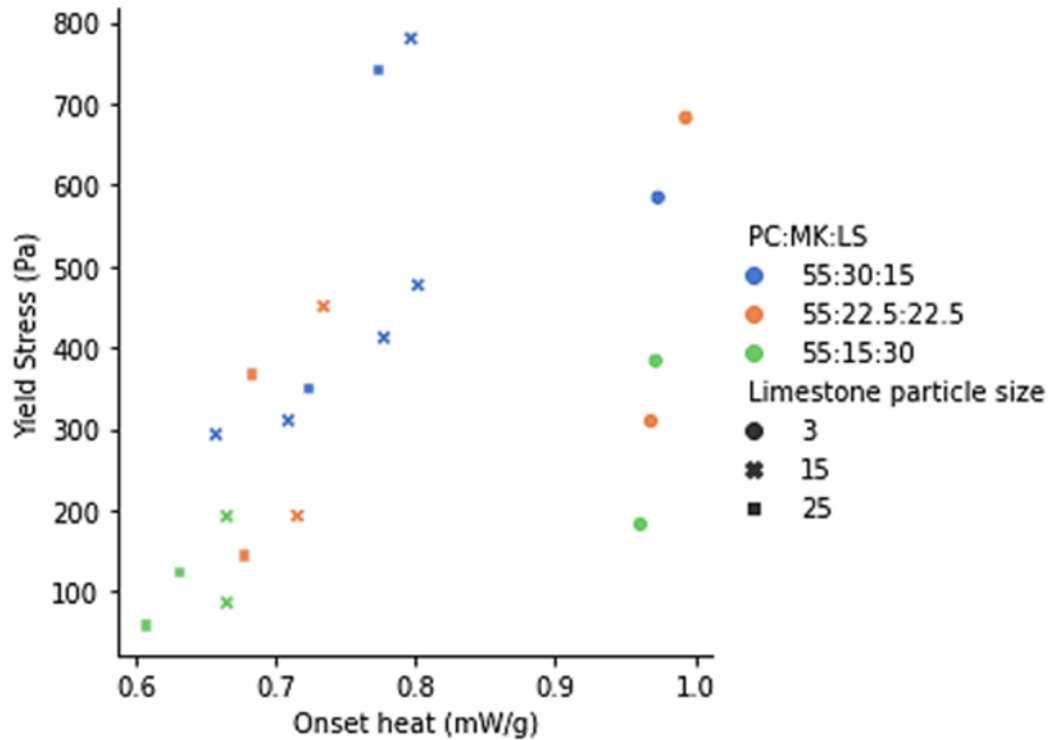


**Figure 4.8 – Correlation between the onset heat and yield stress**

#### 4.6 Conclusions

This study quantified the influence of changes in w/s, metakaolin fraction, limestone particle size and added gypsum content on LC<sup>3</sup> yield stress, plastic viscosity and onset heat. Stepwise regression demonstrated that unlike in other PC-based binders (e.g., neat portland, PC-limestone, PC-fly ash cements) where a single compositional variable can largely capture variations on the rheological properties, with LC<sup>3</sup> four predictors – K, Al<sub>2</sub>O<sub>3</sub>/SO<sub>3</sub>, TPD and MK/LS – are needed to make accurate predictions of yield stress and plastic viscosity. This was accomplished through SVR. Also, the NW kernel smoothing method was utilized to parametrize hydration kinetics obtained by isothermal calorimetry,

which were then correlated to LC<sup>3</sup> yield stress via the onset heat. However, yield stress was more sensitive to LC<sup>3</sup> composition than onset heat.

Some key conclusions include regarding compositional effects on yield stress include:

- Increasing metakaolin fraction increases the yield stress and plastic viscosity of LC<sup>3</sup> and can result in greater variations on the yield stress at relatively higher w/s. This suggests that electrostatic interactions are significant, especially for diluted cementitious suspensions.
- Use of fine limestone (L3) leads to higher yield stresses and plastic viscosities than coarser limestone (L15 and L25) for each PC:MK:LS. As the limestone content increases this effect is exacerbated for the yield stress but not for plastic viscosity.
- As the added gypsum increases, yield stress and plastic viscosity decrease. This is attributed primarily to changes in the sulfate balance of the system, where higher gypsum contents inhibit the rapid formation of calcium aluminum hydrates. Also, plastic viscosity is more sensitive to changes in sulfate balance than yield stress.

From the machine learning approach, these conclusions can be made:

- The ML models (SVR) elucidated the diversity of mechanisms through which the MK component dominates the rheological behavior of LC<sup>3</sup>, both directly and through its interactions with the other mineral constituents. Accurate predictions could be achieved with SVR for both the yield stress (RMSE = 59.14 Pa) and plastic viscosity (RMSE = 0.278 Pa.s) of LC<sup>3</sup>.

- The NW kernel smoothing method can be used to identify the heat flow parameters such as the onset heat and onset time, as it enables time derivatives of the heat flow data from the calorimetry to be calculated.
- Good correlations were found between onset heat and yield stress for pastes including the coarser limestones L15 and L25 ( $R^2=0.712$ ) and L3 ( $R^2=0.809$ ). This distinction with respect to limestone particle size originates from the acceleration and nucleation effect introduced with the introduction of fine limestone particles (L3).
- The MK fraction was found to influence yield stress more than onset heat. This was related to increases not only in the TPD, but also to increases  $Al_2O_3/SO_3$  and MK/LS, with increasing MK content.

The modelling results presented in this study can be used to tailor the yield stress and plastic viscosity of LC<sup>3</sup> binders based on composition. Future work can extend these outcomes by also considering the influence of chemical admixtures, such as superplasticizers.

## **CHAPTER 5. RELATING LC<sup>3</sup> MICROSTRUCTURE, SURFACE RESISTIVITY AND COMPRESSIVE STRENGTH DEVELOPMENT**

### **5.1 Introduction**

Limestone calcined clay cements (“LC<sup>3</sup>”) have been identified as promising sustainable cementitious binder compositions that can be used globally at an industrial scale as an alternative to PC [13]. The appeal of LC<sup>3</sup> originates from the wide availability of the relatively minimally processed minerals that substitute for cement clinker at a relatively high rate, resulting in a binder composition which is lower in embodied energy and embodied carbon dioxide than PC [8, 13, 34]. A typical LC<sup>3</sup> binder formulation consists of 50% PC clinker, 30% calcined clay, 15% limestone and 5% gypsum, by mass [8, 13, 34]. However, variations in these proportions and in the purity of the calcined clay (i.e., kaolinite content) and limestone sources have been explored [33, 48, 137].

In addition to C-S-H formation due to cement hydration, compressive strength development in LC<sup>3</sup> is dependent on the formation of C-(A)-S-H, ettringite and carboaluminate phases [33, 48]. These phases form via multiple pathways, including the pozzolanic reaction between metakaolin (calcined kaolinite) and portlandite – forming C-(A)-S-H, and the reaction between metakaolin and limestone – forming hemicarboaluminate [33]. Portlandite that forms with the hydration of alite and belite is consumed in the pozzolanic reactions to form C-(A)-S-H and carboaluminates; therefore, the presence of portlandite is proposed as the limiting factor for satisfactory microstructural development of LC<sup>3</sup> [51].



The relationships between microstructural development and the resulting gain in mechanical property in LC<sup>3</sup> are complex. Significant pore refinement occurs in LC<sup>3</sup> incorporating calcined clay with high metakaolin content (> 65%) due to the metakaolin reaction as early as 3 days of hydration, resulting in a pore threshold radius of ~10 nm [48]. This can reduce the degree of hydration of the clinker [48] since a higher saturation level is needed for finer pores to accommodate the carboaluminate phases [48, 50]. Further, Zunino and Scrivener [33] found that strength development is dependent on metakaolin content up to 3 days of hydration, but is independent of metakaolin content by 7 days and beyond. These findings imply that factors impacting early (< 7 days) and late strength (> 7 days) development of LC<sup>3</sup> are not the same. This makes prediction of the LC<sup>3</sup> strength development a challenging task because the finer pore structure influenced by the composition of LC<sup>3</sup> contributes to strength, while it may limit further hydrate growth.

Given the significance of microstructural development for strength gain, quantification of these characteristics is desirable for assessing formulations and predicting performance. Non-destructive, time-series measurements of surface resistivity have emerged as an important tool to relate concrete composition to microstructure (and compressive strength) development. In an early study by Nadelman and Kurtis [138], different binary and ternary cement mixtures comprised of Type I/II ordinary PC, Type II blended cement, and two supplementary cementitious materials (SCMs) (i.e., an ASTM C618 Class F fly ash and metakaolin) were produced. The authors were able to capture the outset of pozzolanic reactions occurred by SCMs which is marked by a discernible slope change in the surface resistivity curves, providing a semi-quantitative assessment of the performance of different SCMs and the rate of the microstructural development of different

cement mixtures. Ramezaniapour et al. [139] investigated the surface resistivity, permeability and compressive strength development of 57 different concrete mixtures including various supplementary cementitious materials (SCMs), such as silica fume and metakaolin, and found strong a logarithmic relationship between surface resistivity and permeability for all concrete mixtures explored. This relationship was confirmed later in another study including a wider range of SCMs, including metakaolin [140]. However, despite that pore structure plays a significant role in both the surface resistivity and strength, only a modest correlation ( $R^2 = 0.767$ ) between these was observed for concrete mixtures containing metakaolin [139], and the authors concluded that they could not recommend surface resistivity measurements as a means of predicting strength. Recently, Dhandapani et al. [63] compared surface resistivity of LC<sup>3</sup> with PC-fly ash and neat PC binders. While the surface resistivity of LC<sup>3</sup> was found to be significantly higher than PC-fly ash and PC binders due to extensive pore refinement, again, this study showed that the variations in strength for all binders could not be well-explained by surface resistivity.

## **5.2 Research Significance**

Although pore structure and interconnectivity are significant factors for both surface resistivity and compressive strength, the relationship between these properties is difficult to establish for LC<sup>3</sup> binders because they contain mineral components of varying composition, size, solubility, and reactivity. Understanding of potential relationships between surface resistivity and compressive strength development for LC<sup>3</sup> binders can be useful in design guidance since both performance indicators are related to compositional variables. Toward the goal of providing design guidance by relating the composition of LC<sup>3</sup> binders to property evolution, the influence of metakaolin content, limestone particle

size and gypsum content on phase assemblage, concrete surface resistivity and mortar compressive strength is explored.

### **5.3 Experimental**

#### *5.3.1 Materials*

PC, metakaolin, three limestone powders and gypsum used for this study were introduced in previous chapter (Section 3.3.1). For the concretes, the coarse aggregate used was a crushed granite with a maximum size of 19 mm and a specific gravity of 2.79, whereas natural sand – with a fineness modulus of 2.4 and specific gravity of 2.62 - was used as the fine aggregate. For mortars, graded standard sand was used [141].

#### *5.3.2 Mix Design*

Seven LC<sup>3</sup> formulations were investigated (Table 5.1) that vary in constituent materials proportions and constituent particle size distribution. These formulations enable comparisons to examine the influence of PC, metakaolin and limestone proportioning (PC:MK:LS) in the binder, as well as the limestone particle size and gypsum dosage (i.e., G0, G2, and G5 representing the percent mass fraction), on surface resistivity and compressive strength development. Specifically, 55:30:15 (L15-G0), 55:22.5:22.5 (L15-G0) and 55:15:30 (L15-G0) were compared to explore the influence of PC:MK:LS. The effect of limestone particle size was elucidated with 55:30:15 (L3-G0), 55:30:15 (L15-G0) and 55:30:15 (L25-G0). Further, the influence of gypsum dosage was studied with 55:30:15 (L15-G0), 55:30:15 (L15-G2) and 55:30:15 (L15-G5).

The water-to-solid (PC + metakaolin + limestone+ gypsum) ratio (w/s) used for the mixes was 0.40 for both the surface resistivity and mortar strength experiments. This w/s ratio of 0.40 was selected as it was proven to achieve satisfactory performance with LC<sup>3</sup> and recommended for field applications [63]. Deionized (DI) water with a resistivity of 18.2 MΩ was utilized for all paste samples (TGA samples) and mortar cubes. Tap water was used for concrete mixtures. Superplasticizer (SP, BASF MasterGlenium 7920) was added up to 1% by mass of binder to achieve sufficient workability for mortar and concrete samples.

**Table 5.1 - Experimental matrix, showing binder content by mass fraction and superplasticizer content by weight of solids (PC+Metakaolin+Limestone+Gypsum).**

<b>Material</b>	<b>55:30:15 (L3-G0)</b>	<b>55:30:15 (L15-G0)</b>	<b>55:30:15 (L25-G0)</b>	<b>55:30:15 (L15-G2)</b>	<b>55:30:15 (L15-G5)</b>	<b>55:22.5 :22.5 (L15- G0)</b>	<b>55:1 5:30 (L15 -G0)</b>
<b>PC</b>	55	55	55	53.9	52.25	55	55
<b>MK</b>	30	30	30	29.4	28.5	22.5	15
<b>L3</b>	15	-	-	-	-	-	-
<b>L15</b>	-	15	-	14.7	14.25	22.5	30
<b>L25</b>	-	-	15	-	-	-	-
<b>Gypsum</b>	-	-	-	2	5	0	-
<b>SP*</b>	1	1	1	1	1	0.5	0.5
<b>Water (kg/m<sup>3</sup>)</b>	202	202	202	202	202	202	202
<b>Binder (kg/m<sup>3</sup>)</b>	504	504	504	504	504	504	504
<b>Fine aggregate (kg/m<sup>3</sup>)</b>	593	593	593	593	593	593	593
<b>Coarse aggregate (kg/m<sup>3</sup>)</b>	1031	1031	1031	1031	1031	1031	1031

\*These superplasticizer (SP) contents were the same for mortar and concrete samples of each formulation.

### 5.3.3 Analytical Methods

Phase development was assessed by thermogravimetric analysis (Hitachi EXSTAR TG/DTA 7300) performed on pastes prepared with w/s of 0.40 at 3, 7 and 28 days (also the testing days of strength). From the hydrated phases typically forming in LC<sup>3</sup>, it is known that C-(A)-S-H and ettringite can be identified with their mass losses between 90-120 °C [98] while the presence of carboaluminates can be confirmed with their decomposition peak at ~140 °C [41, 44, 98]. Portlandite, as expected to form via the PC hydration, decomposes between 400-470 °C [98]. Apart from these phases formed by hydration reactions, gypsum and calcite can also be identified with their decomposition temperature ranges between 140-160 °C [98] and 600-750 °C [44, 98], respectively. The samples for thermogravimetric analysis (TGA) were cast in sealed bags until testing to avoid the evaporation of water and carbonation and then were stored at room temperature (23±2 °C). On each testing day, the samples were first crushed and ground to 600 µm. The hydration of ground samples was stopped by solvent exchange according to the procedure described in [98] using isopropanol and diethyl ether under N<sub>2</sub> atmosphere. The powders obtained after the solvent exchange were sieved to 75 µm, and 20 ±2 mg of fine powder was placed in aluminum crucibles for analyses. The analysis was conducted by heating the sample from 40°C to 1000°C at a rate of 10°C/min under N<sub>2</sub> atmosphere with a flow rate of 100 cc/min. The portlandite content of the samples was calculated using the tangential method and normalized to 100 g anhydrous cement as described in [98]. Also, the bound water was quantified based on the mass loss between 40 °C and 550 °C [142]. The relative error of the portlandite and bound water quantifications were ±5% and ±10%, respectively, [98, 143].

#### 5.3.4 Testing

Compressive strength development of the LC<sup>3</sup> formulations was investigated based on 2-inch (50 mm) mortar cube specimens. Mortar was chosen instead of concrete for strength experiments to minimize variability [144] and because they are already used in standard specifications for assessing SCM performance, such as ASTM C618 [145]. Mortars with sand-to-cementitious materials ratio of 2.75 were mixed according to ASTM C305 [92]. The admixture was stirred into the DI water prior to adding to the cementitious materials. After mixing, the mortar cubes were molded according to ASTM C109 [71] and then kept in a humidity chamber at 23±2 °C and 100% humidity for 24 h. After demolding, the samples were cured in lime-saturated water (23±2 °C) until testing. The compressive strength was measured after 3, 7, and 28 days of hydration with a loading rate between 900 to 1800 N/s according to ASTM C109 [71]. Six specimens were tested for each age, and the average and standard deviation are reported.

Surface resistivity was measured on 4x8 in. (100 x 200 mm) concrete cylinders, cured in lime-saturated water, using a four-probe Wenner array (Resipod 38 mm probe spacing model, Proceq SA, Switzerland). The concrete cylinders were prepared according to ASTM C192 [146]. All concrete mixtures included the same proportions of fine and coarse aggregates, and with the binder composition (but not content) varying. On the testing days, for each of the concrete cylinders, the surface resistivity was measured at four longitudinal lines drawn that are located at 0-, 90-, 180-, and 270- degree points of the circumference, corresponding to eight measurements in total (two measurements per line) for each concrete cylinder (Please see Figure 1 in [147] for test setup). The measurements were taken following the procedure described in AASHTO T358 [148] until 56 days of hydration for three replicates of each set of samples. To take into account the limewater

curing, the surface resistivities were multiplied by 1.1 per the requirement in AASHTO T358 [148]. Hence, the average and the standard deviation of 24 measurements (eight measurements per each of three replicates) were reported per day.

The surface resistivity and compressive strength results were also compared in terms of the rate of change, in percentages, from 3 to 7 days ( $\Delta_{3-7d}$ ), and from 7 to 28 days ( $\Delta_{7-28d}$ ). The purpose of this comparison was to investigate whether a correlation can be established between the rates, as well as evaluating correlations between the absolute values. This analysis was motivated by [147] where the authors compared the pozzolanic reactivity of various candidate SCMs based on slope changes in time-series surface resistivity measurements. For both strength and resistivity, the change over these periods was calculated simply – based on average values of resistivity and strength –, as shown in Equations 5.1 to 5.4:

$$\Delta_{(3-7d)}(\%) = 100 \times \frac{\text{SR at 7 days} - \text{SR at 3 days}}{\text{SR at 3 days}} \quad (5.1)$$

$$\Delta_{(7-28d)}(\%) = 100 \times \frac{\text{SR at 28 days} - \text{SR at 7 days}}{\text{SR at 7 days}} \quad (5.2)$$

$$\Delta_{(3-7d)}(\%) = 100 \times \frac{\text{Strength at 7 days} - \text{Strength at 3 days}}{\text{Strength at 3 days}} \quad (5.3)$$

$$\Delta_{(7-28d)}(\%) = 100 \times \frac{\text{Strength at 28 days} - \text{Strength at 7 days}}{\text{Strength at 7 days}} \quad (5.4)$$

To compare all LC<sup>3</sup> binders in terms of their microstructural development decoupled from the influence of the pore solution, the formation factor (F) was calculated using Equation 5.5:

$$F = \frac{\sigma_p}{\sigma_b} = \frac{\rho_b}{\rho_p} \quad (5.5)$$

F is the ratio of pore solution conductivity ( $\sigma_p$ ) to bulk conductivity ( $\sigma_b$ ), or the ratio of bulk resistivity ( $\rho_b$ ) to pore solution resistivity ( $\rho_p$ ) [56]. Recently, water-filled porosity and formation factor were found to have a strong relationship for PC, PC-fly ash and LC<sup>3</sup> binders in which increasing the formation factor corresponded to lower water-filled porosity [149]. To calculate the formation factor, the bulk resistivities were obtained by dividing the surface resistivity with a geometric correction factor, 1.93 [140, 150], and the pore solution conductivities were estimated using the approach developed at NIST, which determines the pore solution conductivity as a function of the ionic concentration (i.e., [Na<sup>+</sup>], [K<sup>+</sup>], [OH<sup>-</sup>]) and the degree of hydration [151, 152]. The pore solution resistivities were calculated by taking the inverse of the pore solution conductivities [56]. Thereafter, bulk resistivities were divided by pore solution resistivities to calculate the formation factors.

Some assumptions were needed to use this NIST tool for LC<sup>3</sup>. For instance, the NIST tool does not take metakaolin and limestone fractions as inputs. Therefore, the average alkali contents, Na<sub>2</sub>O and K<sub>2</sub>O (wt. %), were calculated based on the oxide compositions of constituent materials (Table 3.2) for each mixture proportion (Table 5.1). The calculated alkali contents were then introduced as those of LC<sup>3</sup>. Variations in the phase



assemblage of  $LC^3$  formulations that may originate from different PC:MK:LS, limestone particle size or added gypsum were not considered by the NIST tool as impacting factors for the pore solution conductivities. For instance, this approach neglected the potential variations in the pore solution conductivity originating from varying amounts of C-(A)-S-H, which can bind alkalis [68, 69], formed in  $LC^3$  formulations. Instead, the assumption is 75% of alkali ions from  $LC^3$  are released into the pore solution by 28 days of hydration [152]. In addition, the degree of hydration values used as inputs were based on [48]. In this study, the authors showed more than 65% calcined kaolinite content in the calcined clay, the degree of hydration of PC clinker in  $LC^3$  plateaus around ~72% by 3 days of hydration. In the case of  $\leq 65\%$  calcined kaolinite content in the calcined clay, the degree of hydration increases from 70% to 90% depending on the calcined kaolinite content between 3 and 90 days. Table 5.2 shows the assumed degree of hydration inputs used to estimate the pore solution conductivities (S/m) for each formulation. A sensitivity analysis was performed to quantify the influence of  $LC^3$  reaction (i.e., degree of hydration) on formation factor; by varying degree of hydration by 10%, a maximum of 4% variation in the formation factor values resulted.

**Table 5.2 - The degree of hydration inputs assumed for each LC<sup>3</sup> formulation based on [48]. Effects of limestone fineness and gypsum dosage on the degree of hydration were assumed as negligible.**

<b>Mix ID</b>	<b>Age</b>				
	<b>1d</b>	<b>3d</b>	<b>7d</b>	<b>28d</b>	<b>56d</b>
<b>55:30:15 (L3-G0)</b>	0.60	0.74	0.74	0.74	0.74
<b>55:30:15 (L15-G0)</b>	0.60	0.74	0.74	0.74	0.74
<b>55:30:15 (L25-G0)</b>	0.60	0.74	0.74	0.74	0.74
<b>55:30:15 (L15-G2)</b>	0.60	0.74	0.74	0.74	0.74
<b>55:30:15 (L15-G5)</b>	0.60	0.74	0.74	0.74	0.74
<b>55:22.5:2 2.5 (L15- G0)</b>	0.56	0.70	0.76	0.78	0.78
<b>55:15:30 (L15-G0)</b>	0.58	0.72	0.77	0.81	0.81

#### **5.4 Results**

The relationship between concrete surface resistivity and mortar strength development was explored, to develop understanding useful for developing LC<sup>3</sup> binder compositions with desired performance. The compositional variables explored in this study were PC:MK:LS, limestone particle size and added gypsum content. Other factors (e.g., w/s, aggregate fraction, curing) were kept constant. The phase assemblage of LC<sup>3</sup> binder

compositions was measured at 3, 7 and 28 days, quantifying the portlandite consumption and bound water evolution.

#### *5.4.1 Influence of PC:MK:LS*

Figure 5.1 presents the phase assemblage of three LC<sup>3</sup> formulations, which were produced with the same limestone particle size but varying metakaolin and limestone contents. By 28 days of hydration, the phase assemblages for three LC<sup>3</sup> formulations – 55:30:15, 55:22.5:22.5, and 55:15:30 – are similar (Figure 5.1) and include C-(A)-S-H, ettringite, hemi- and monocarboaluminate phases, portlandite and calcite. The mass losses between 40°C and 550 °C due to the evaporation of bound water are also similar for all mixes, at ~15%, further indicating that no significant difference between the amount of hydrated phases formed in these mixes at 28 days. Hence, the highest mass loss in total observed with 55:15:30 is not because of the differences in the amount of hydrated phases but due to its higher calcite content than other formulations.

The formation of the hydrated phases, in similar amounts, despite the changes in PC:MK:LS support the results from [47] showing no significant differences in the total volume of hydrates at 28 days of hydration resulting from the changes in metakaolin fraction. This phenomenon can be attributed to varying mechanisms for the formation of C-(A)-S-H, ettringite and carboaluminates. For instance, it has been understood that increasing the metakaolin fraction enhances the C-(A)-S-H formation at the expense of portlandite, while the formation of carboaluminates increases until 50% calcined kaolinite by mass in calcined clay [47-49]. Thus, the mix (55:30:15) incorporating highest metakaolin content is likely to have formed more C-(A)-S-H but less carboaluminates

compared to other mixes at 28 days. This is supported through XRD analysis with Rietveld by Avet et al. [47] and by thermodynamic simulations [153] of similar LC<sup>3</sup> blends. On the other hand, ettringite formation is mainly dependent on the sulfate content of the mix [47, 50], which is the same for the mixes displayed in Figure 5.1. Therefore, it can be argued that the variations in the C-(A)-S-H and carboaluminates contents were too subtle to create significant differences in the TGA results.

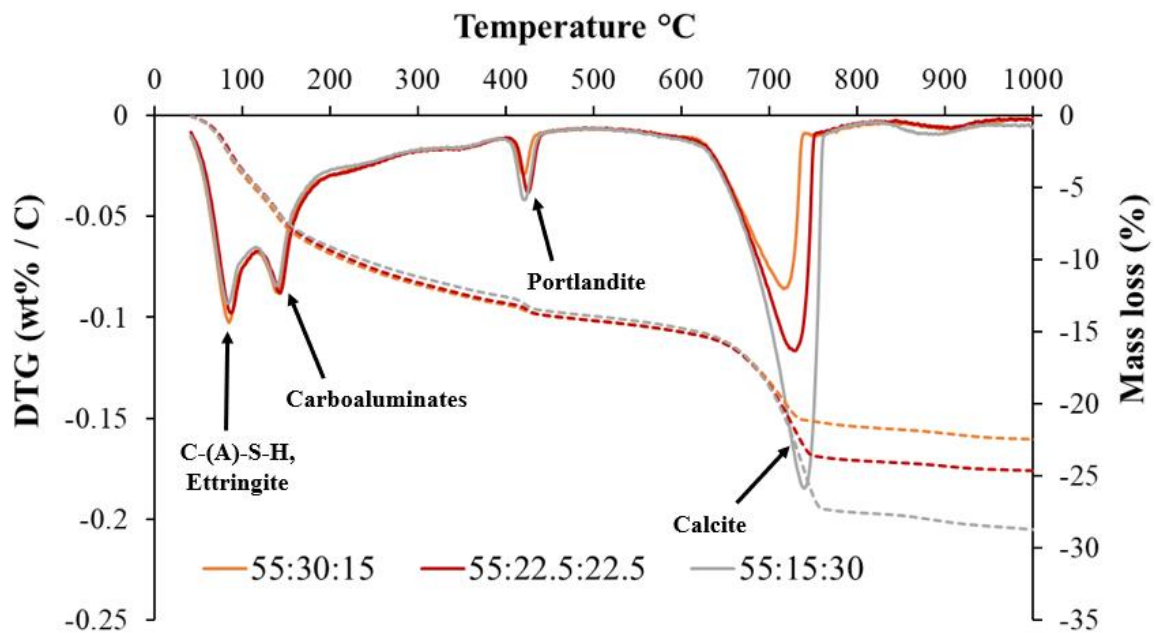


**Figure 5.1 - DTG and mass loss of LC<sup>3</sup> at 28 days of hydration influenced by PC:MK:LS.**

The surface resistivity development was enhanced after 3 days and was directly correlated to the metakaolin content until 7 days (Figure 5.2); it is difficult to draw strong conclusions because of the closeness of the measurements. For example, 55:30:15 (L15-G0) achieves 40 kΩ-cm surface resistivity, whereas 55:22.5:22.5 (L15-G0) and 55:15:30 (L15-G0) achieve 37 and 33 kΩ-cm surface resistivity, respectively at 7 days. This difference may be related to early pore refinement that depends on the metakaolin content

[48]. Overall, after 28 days, any differences in the surface resistivity among these are subtle and fall within the standard deviation range of the measurement.

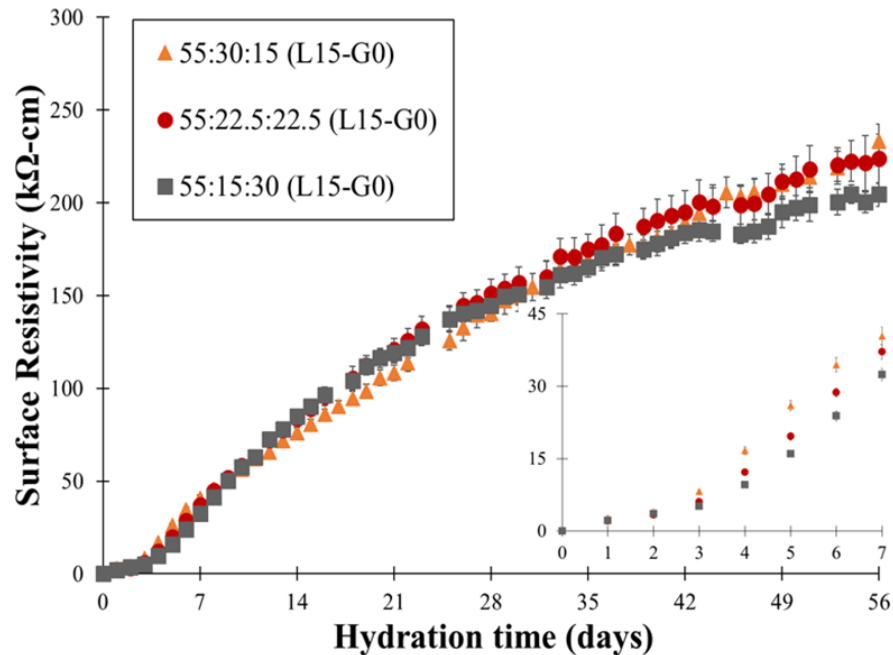


**Figure 5.2 - Surface resistivity development of LC<sup>3</sup> mixtures influenced by PC:MK:LS. Inset shows the results until 7 days of hydration.**

The compressive strength development of these three formulations at 3, 7 and 28 days increased with metakaolin fraction, with the mixture with the highest MK content 55:30:15 (L15-G0) achieving the highest strength. This shows that increasing metakaolin fraction enhanced both the strength development and surface resistivity until 7 days. After 7 days, while surface resistivity was not significantly influenced by the metakaolin fraction, strength was still enhanced by incorporating more metakaolin. To illustrate, by 28 days of hydration 55:30:15 (L15-G0) achieves 55.3 MPa compressive strength, which is 9% and 15% higher than 55:22.5:22.5 (L15-G0) and 55:15:30 (L15-G0), respectively. The differences in 3-day and 28-day strength between 55:22.5:22.5 (L15-G0) and 55:15:30 (L15-G0) fall within the standard deviation range. It should be noted that the phase

assemblage of these formulations (Figure 5.1) showed no significant differences. Therefore, the differences in strength were likely related to physical microstructural differences such as pore structure.

To better understand the rate of change in strength and surface resistivity in these formulations with time, Table 5.3 shows the changes in each between 3 and 7 days ( $\Delta_{3-7d}$ ) and between 7 and 28 days ( $\Delta_{7-28d}$ ). Surface resistivity manifests greater changes in both  $\Delta_{3-7d}$  and  $\Delta_{7-28d}$  than strength, implying that it is more sensitive to the changes in microstructure with hydration. (This phenomenon will be revisited in Discussion section 4.3). However, the rate of change in strength and surface resistivity did not increase with increasing metakaolin fraction. In fact, the highest  $\Delta_{3-7d}$  and  $\Delta_{7-28d}$  in surface resistivity was also the highest  $\Delta_{7-28d}$  for strength and was achieved by the mixture with the lowest MK content 55:15:30 (L15-G0). This can be due to relatively higher degree of hydration of clinker reached with this mixture by 28 days (Table 5.2). Further, these results show a stronger correlation between surface resistivity and compressive strength development from 7 to 28 days, compared to results from 3 to 7 days, for LC<sup>3</sup> with varying metakaolin contents. Overall, these results show that surface resistivity provides an earlier indication of microstructural densification in these mixes than compressive strength.

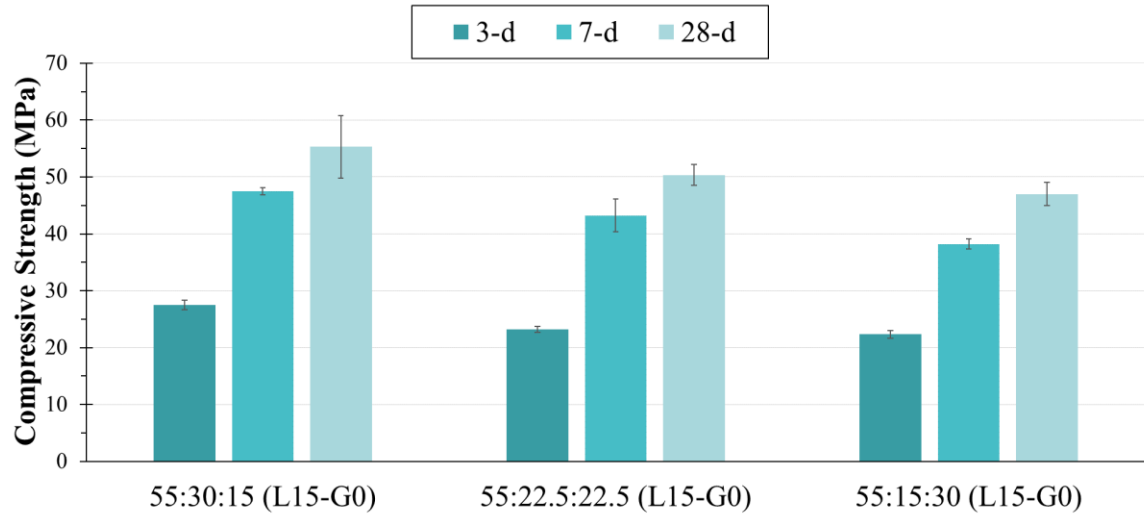


**Figure 5.3 - Compressive strength development of LC<sup>3</sup> mixtures influenced by mixture proportioning.**

**Table 5.3 - Percentage (%) change in surface resistivity and compressive strength of LC<sup>3</sup> mixtures with varying PC:MK:LS between 3 and 7 days and 7 and 28 days.**

Mix ID	Surface resistivity (% change)		Compressive strength (% change)	
	$\Delta(3-7d)$	$\Delta(7-28d)$	$\Delta(3-7d)$	$\Delta(7-28d)$
55:30:15 (L15-G0)	393	247	73	16
55:22.5:22.5 (L15-G0)	511	307	86	16
55:15:30 (L15-G0)	528	346	71	23

#### 5.4.2 Influence of limestone particle size

The hydration products identified in LC<sup>3</sup> mixes with varying limestone particle sizes (Figure 5.4) were identical among the mixtures and included C-(A)-S-H, ettringite, carboaluminates, portlandite and calcite at 28 days of hydration. The mass loss until the temperature associated with the onset of portlandite decomposition, between 40°C, and 400 °C, indicated the total amount of C-(A)-S-H, ettringite and carboaluminate phases. Up to this range, L25 showed a slightly lower mass loss (~0.5%) – within the standard

deviation range - compared to L3 and L15. However, no significant difference in the total amount of hydrated phases – mass loss between 40°C and 550 °C – among the three limestone particle sizes was observed. Moreover, no systematic dependency is found between portlandite or bound water contents and limestone particle size on other ages of testing (i.e., 3 and 7 days). While acceleration in hydration due to the nucleation effect may have been expected for the finest L3, any effects on hydration product formation could not be discerned by TGA. It is possible that the limestone size range tested (Table 3.1) is not be varied enough to demonstrate a measurable nucleation effect through TGA [154].

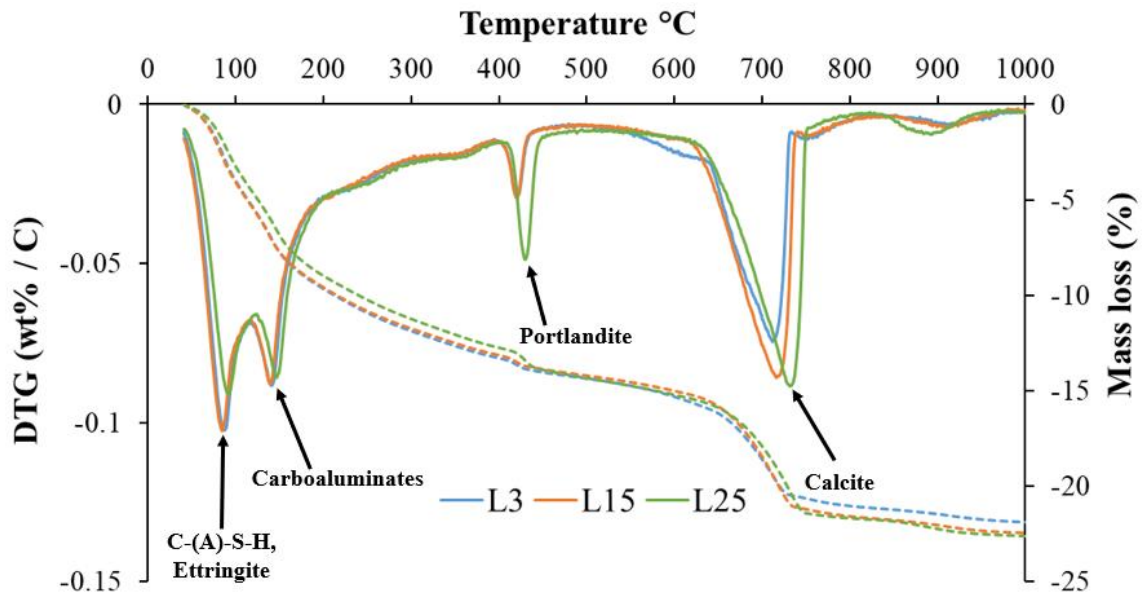


**Figure 5.4 - DTG and mass loss of LC<sup>3</sup> at 28 days of hydration influenced by limestone particle size.**

Figure 5.5 shows the surface resistivity development of LC<sup>3</sup> formulations including the different limestone particle sizes. The surface resistivity of all mixes was enhanced after 3 days of hydration, with the steepest slope observed by the concrete with the finest limestone size, L3, resulting in significantly higher resistivities at all ages than L15 and L25. For instance, by 28 days hydration, L3 achieves 182 kΩ-cm 23% and 31% higher than



that achieved by L15 and L25, respectively. This difference could result from filler and nucleation effects created by L3, leading to denser packing, accelerated precipitation of hydration products (e.g., C-(A)-S-H) and a resulting more disconnected pore structure compared to L15 and L25 [9, 25, 26, 52]. However, as observed in Figure 5.5, no significant difference in the total amount of hydrated phases was found when comparing L3 with L15 and L25 at 28 days. This observation suggests that the filler effect is the more prevalent influence on surface resistivity development for fine limestones and that the nucleation effects, if present, are less significant. Similarly, relatively poor packing – and thus higher porosity, at least initially – could have contributed to the lower surface resistivity measured for the coarsest limestone in 55:30:15 (L25-G0) [58].

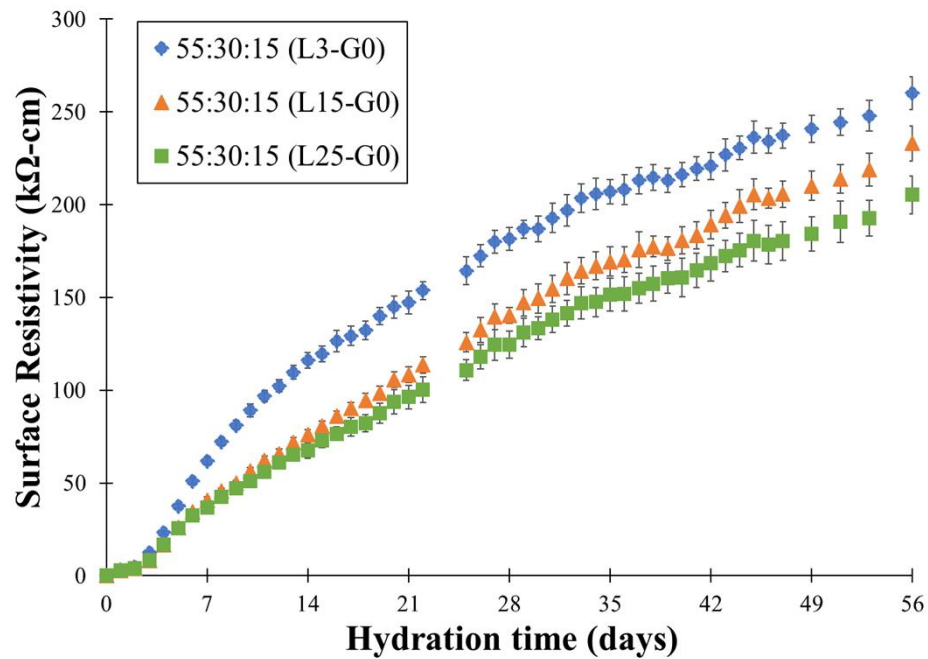


**Figure 5.5 - Surface resistivity development of LC<sup>3</sup> mixtures influenced by limestone particle size.**

The compressive strength development of LC<sup>3</sup> mortars with varying limestone particle sizes is presented in Figure 5.6. It appears that decreasing the limestone particle

size increases early strength, potentially up to a 7-day strength. For instance, 55:30:15 (L3-G0) achieves 33.7 MPa at 3 days, which is 18% and 19% higher than that achieved with L15 and L25, respectively. However, the effectiveness of limestone particle size appears to decrease by 28 days similar to the findings from [58]. By 28 days, the compressive strength varies by only 4% to 8% when comparing L3 and L25 to L15, respectively. In other words, the filler effect from L3 could not be distinguished by the compressive strength at 28 days, contrary to the distinction observed by surface resistivity. That is, the microstructural differences manifested by particle size effects were more evident through surface resistivity testing than through compressive strength. Further evidence of this, through the use of estimated formation factors, will support this hypothesis (see Discussion section).

The mixtures 55:30:15 (L3-G0) exhibited the highest increase in surface resistivity from 3 to 7 days of hydration (Table 5.4), which might be linked to the filler effect observed with L3, resulting in a denser microstructure at early ages. This enhancement in surface resistivity with L3 was not, however, consistent with compressive strength development. That is, L15 and L25, which showed lower (from 2 to 39%) surface resistivity increase, achieves higher (from 13 to 27%) compressive strength increase than L3 between 3 and 7 days. Also, L3 continues to demonstrate the least strength increase from 7 to 28 days of hydration; over this time period, the least surface resistivity increase is also observed. The binding of water within agglomerates of fine limestone, which could limit hydration, might be the reason for this relatively lower increase in both resistivity and strength observed with L3 compared to L15 and L25 [53]. This slower increase in resistivity and strength development can also be due to the higher supersaturation level required for precipitation

within finer pores [48, 50], limiting the formation of hydration products for LC<sup>3</sup> from about 3 days onwards.

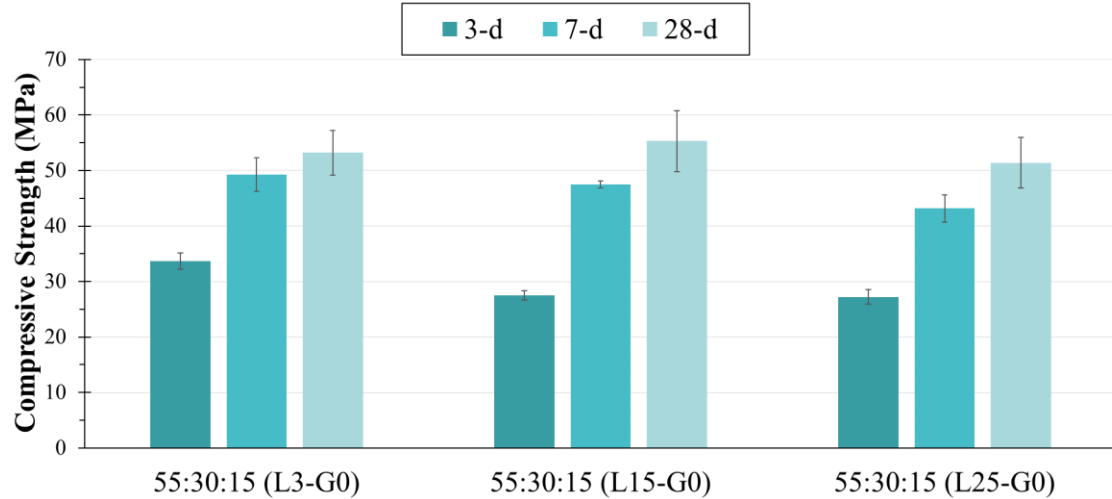


**Figure 5.6 - Compressive strength development of LC<sup>3</sup> mixtures influenced by limestone particle size.**

**Table 5.4 - Percentage (%) change in surface resistivity and compressive strength of LC<sup>3</sup> mixtures with varying limestone particle size between 3 and 7 days and 7 and 28 days.**

Mix ID	Surface resistivity (%)		Compressive strength (%)	
	$\Delta(3-7d)$	$\Delta(7-28d)$	$\Delta(3-7d)$	$\Delta(7-28d)$
55:30:15 (L3-G0)	395	194	46	8
55:30:15 (L15-G0)	393	247	73	16
55:30:15 (L25-G0)	356	237	59	19

#### 5.4.3 Influence of added gypsum content

The prior systems examined excluded gypsum in the interest of understanding the effects of PC:MK:LS and limestone particle size on property evolution, but the effect of gypsum dosage on surface resistivity and strength development also needs to be understood as it can greatly influence the phase assemblage of LC<sup>3</sup> [30, 33]. Figure 5.7 shows the

hydration products identified and the mass loss of LC<sup>3</sup> formulations with varying gypsum contents at 28 days of hydration, investigated with thermogravimetric analyses. The only difference in phase assemblages is gypsum, found only in 5% gypsum incorporating mix 55:30:15 (L15-G5). No significant difference between mass losses of 55:30:15 (L15-G2) and 55:30:15 (L15-G5) was observed, suggesting a similar total amount of hydration products formed in these formulations at 28 days. On the other hand, both these pastes lost ~1.5% more mass – within the standard deviation range – between 40 and 550 °C (due to the evaporation of bound water) than 55:30:15 (L15-G0), indicating the presence of more hydrated phases in the mixes containing gypsum.

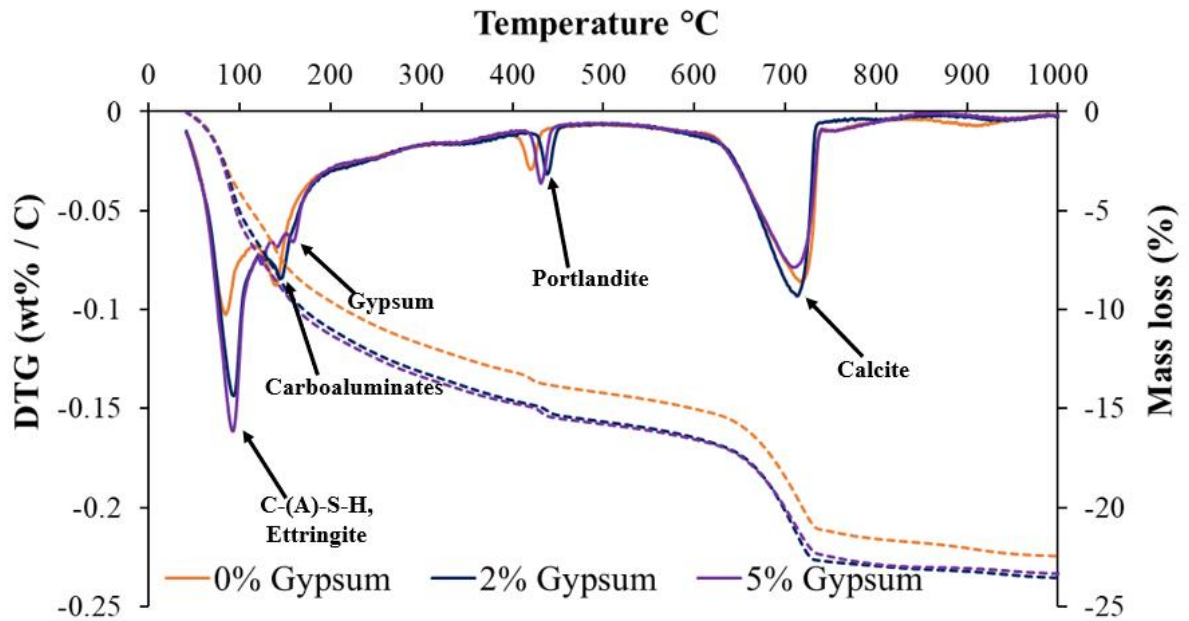


**Figure 5.7 - DTG and mass loss of LC<sup>3</sup> at 28 days of hydration influenced by gypsum dosage.**

Figure 5.8 shows the surface resistivity development of LC<sup>3</sup> formulations at different gypsum dosages. At all ages of measurement, increasing additions of gypsum produce higher surface resistivity. To illustrate, by 28 days of hydration, 55:30:15 (L15-

G5) achieves 195 k $\Omega$ -cm surface resistivity, which is 23% and 28% higher than that achieved with 55:30:15 (L15-G2) and 55:30:15 (L15-G0). This finding agrees with the higher mass losses measured from hydrated phases with gypsum-including formulations than the companion mix without, 55:30:15 (L15-G0). The increase in surface resistivity with gypsum can be related to the greater amount of ettringite formed in the solid matrix, which is understood to be more persistent in LC<sup>3</sup> compared to plain PC systems due to the presence of carboaluminates [41, 42, 155].

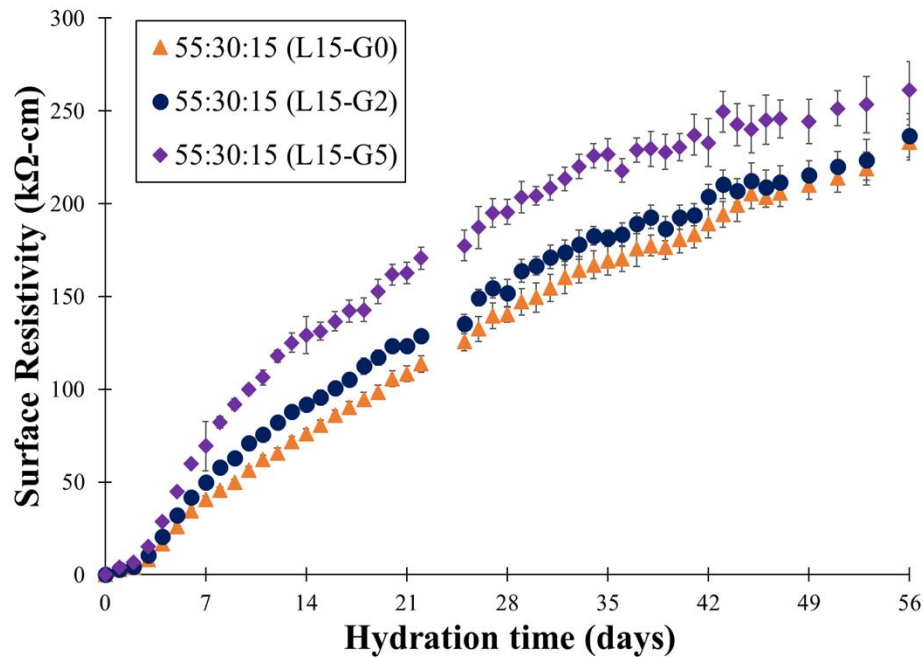


**Figure 5.8 - Surface resistivity development of LC<sup>3</sup> mixtures influenced by gypsum dosage.**

Figure 5.9 introduces the compressive strength development of LC<sup>3</sup> mixtures with varying added gypsum contents. Increasing added gypsum does not greatly influence the 3-d strength, but variations are observed by 7 days, wherein 2% added gypsum results in roughly 11% lower strength than other mixtures. By 28-d 55:30:15 (L15-G0) achieved the highest average strength with 55.3 MPa, but the differences in strength are within the standard deviation of the measurement. Similar to this trend, Antoni et al. [41] also

observed enhancement in compressive strength at early ages (1 day) but a decrease in strength at 28 days with increasing added gypsum, which could not be explained. Based on these results, it is deduced that the higher ettringite formation with increasingly added gypsum can be beneficial for early strength (< 3 days), but the diluted fraction of PC by added gypsum is likely to result in a decrease of strength beyond 7 days. Although the differences in mass losses due to evaporation of bound water and strength are not statistically significant, it is still worth mentioning that the mixture with the highest strength, 55:30:15 (L15-G0), demonstrated the lowest bound water content (Figure 5.7). This contrast casts doubts on the ability of bound water to capture the differences in LC<sup>3</sup> strength influenced by the amount of added gypsum. The bound water-strength relationship will be revisited in Discussion section.

Table 5.5 compares surface resistivity and compressive strength development for LC<sup>3</sup> formulations with varying amounts of gypsum. There is a systematic dependency on gypsum dosage in which higher gypsum contents correspond to less increase in surface resistivity and strength for both  $\Delta_{(3-7d)}$  and  $\Delta_{(7-28d)}$ . Although a strong relationship between surface resistivity and compressive strength influenced by gypsum dosage could not be observed, a linkage between the rate of change in surface resistivity and strength development is present, which can be useful for further predictions of performance with these binders.

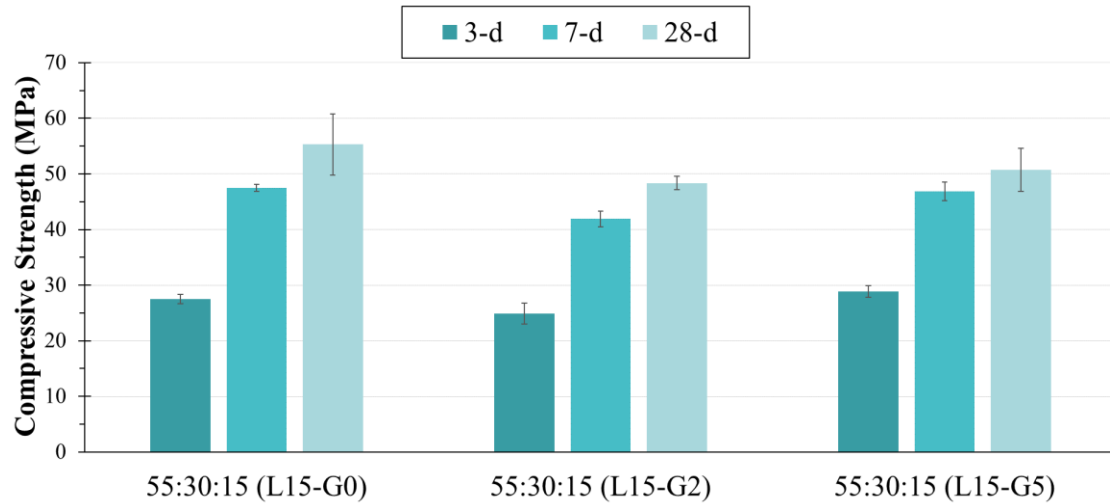


**Figure 5.9 - Compressive strength development of LC3 mixtures influenced by gypsum dosage.**

**Table 5.5 - Percentage (%) change in surface resistivity and compressive strength of LC<sup>3</sup> mixtures with varying added gypsum content between 3 and 7 days and 7 and 28 days.**

Mix ID	Surface resistivity (%)		Compressive strength (%)	
	$\Delta(3-7d)$	$\Delta(7-28d)$	$\Delta(3-7d)$	$\Delta(7-28d)$
55:30:15 (L15-G0)	393	247	73	16
55:30:15 (L15-G2)	378	205	68	16
55:30:15 (L15-G5)	360	182	62	8

## 5.5 Discussion

### 5.5.1 Formation Factor

While the results presented here considered direct measurements of resistivity, the variations in pore solution composition, both among samples and with time, influence those measurements. To minimize pore solution effects and to allow for a greater focus on solid microstructure, formation factors were determined for each of the LC<sup>3</sup> formulations, as

described in the experiment section 5.3.4. Table 5.6 displays the formation factor of all LC<sup>3</sup> formulations at different ages. In the following discussion, the formation factors are compared with respect to varying PC:MK:LS, limestone particle size and gypsum dosage, similar to the organization followed in the previous section.

The formation factors increase with the metakaolin content in concrete. The higher measured formation factor in 55:30:15 (L15-G0) at both 7 and 28 days as compared to 55:15:30 (L15-G0) supports the idea that the relatively lower surface resistivities achieved with 55:30:15 (L15-G0) between these ages (Figure 5.2) were linked to its relatively higher pore solution conductivity, not because of a lower degree of porosity refinement. The only exception for the direct relationship between metakaolin fraction and formation factor is observed at 28 days, where 55:22.5:22.5 (L15-G0) achieves a slightly higher (4%) formation factor than concrete incorporating higher metakaolin, 55:30:15 (L15-G0).

Formation factor was found to increase with limestone fineness. This correlation corroborates the proposed mechanism derived from the surface resistivity curves, shown in Figure 5.5, that denser microstructure is achieved with increasing limestone fineness beyond 24 hours of hydration. Similar trends observed with formation factor and surface resistivity measurements further promise that the surface resistivity test can be adapted to compare the microstructural property of LC<sup>3</sup> binders including varying limestone particle sizes.

Increasing gypsum content corresponded to higher formation factor at all ages, except 56 days when the 0%-gypsum mix (55:30:15 (L15-G0)) achieved a slightly (0.4%) higher formation factor than the corresponding 2% gypsum mix. Remarkably,



incorporating 5% gypsum can increase the formation factor by 44% as early as 1 day. This increase is to a lesser extent at later ages and decreases from 44 to 7% at 56 days of hydration. Overall, these results reinforce that the gypsum dosage is of paramount importance for LC<sup>3</sup> and needs to be optimized properly to achieve a refined microstructure.

Based on these results, optimizing the limestone fineness and gypsum content are both effective ways to densify microstructure in LC<sup>3</sup> concrete. When all mixes are considered, the added gypsum content is the most significant parameter until 28 days. This observation is based on the highest formation factor of 55:30:15 (L15-G5) until 28 days of hydration and can be attributed to the enhanced ettringite formation with increasing gypsum content (Figure 5.7). Beyond 28 days, using relatively finer limestone size has a greater effect, over both PC:MK:LS and added gypsum content, suggesting that the filler effect by limestone has a long-term significance for LC<sup>3</sup> microstructural development.

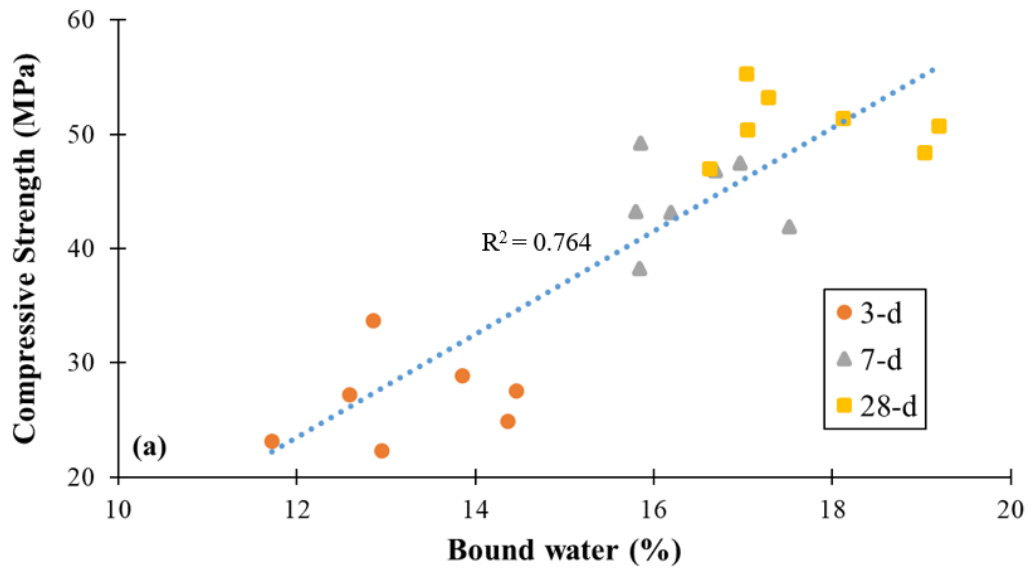
**Table 5.6 - Estimated formation factor (unitless) of LC<sup>3</sup> formulations.**

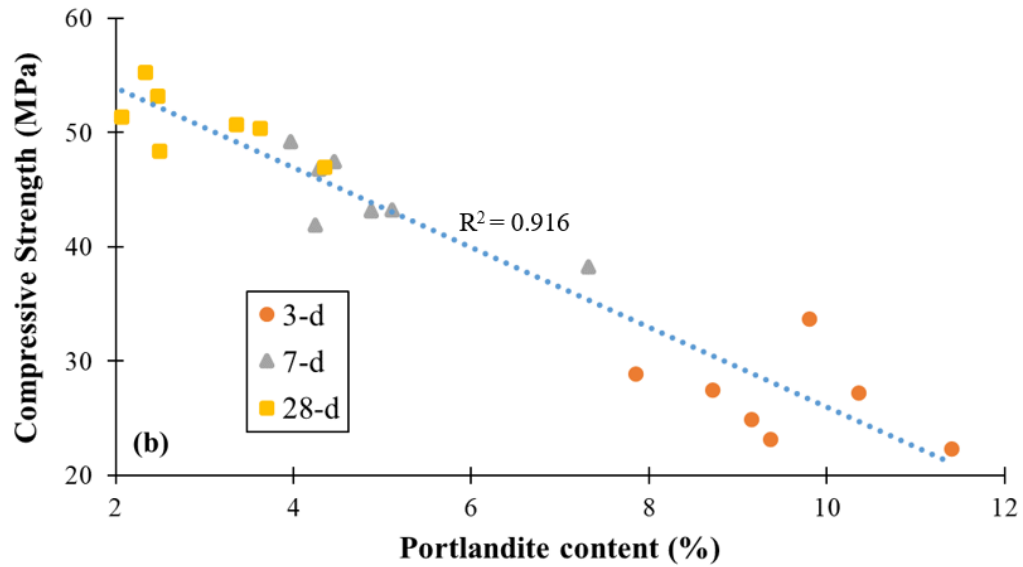
Mix ID	Age				
	1d	3d	7d	28d	56d
<b>55:30:15 (L3-G0)</b>	82	360	1779	5220	7483
<b>55:30:15 (L15-G0)</b>	73	236	1163	4033	6699
<b>55:30:15 (L25-G0)</b>	72	233	1062	3581	5902
<b>55:30:15 (L15-G2)</b>	76	293	1400	4276	6673
<b>55:30:15 (L15-G5)</b>	105	413	1896	5347	7144
<b>55:22.5:2 2.5 (L15- G0)</b>	52	161	1016	4182	6192
<b>55:15:30 (L15-G0)</b>	51	129	834	3801	5371

*5.5.2 Linking portlandite consumption and bound water evolution to surface resistivity and strength development*

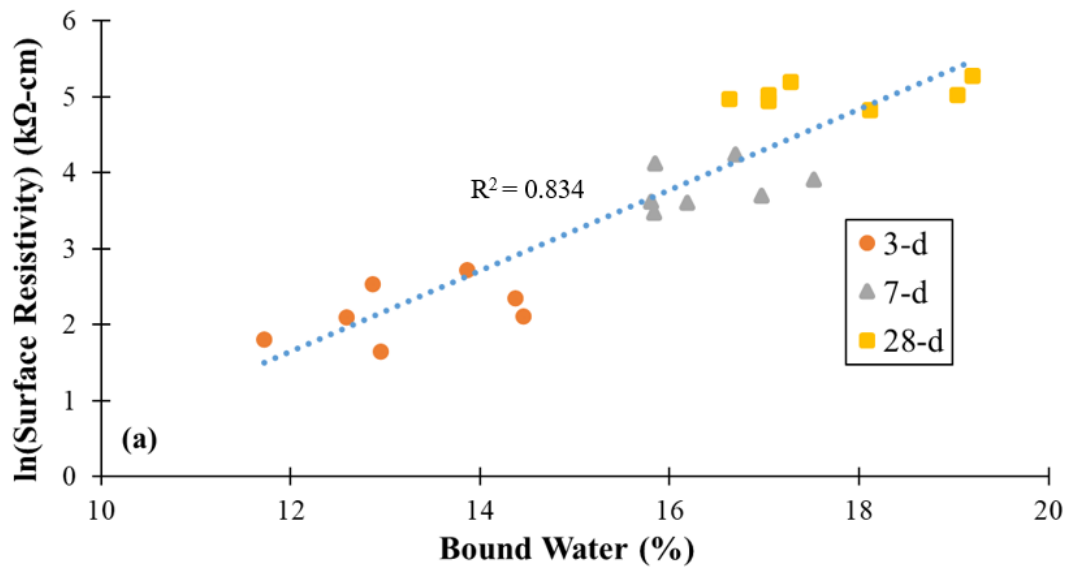
In this section, LC<sup>3</sup> mortar compressive strength and LC<sup>3</sup> concrete surface resistivity are compared with the amount of portlandite, and bound water quantified by TGA analyses, for all of the mixes examined. From these data, as shown in Figure 5.10, portlandite content is found to be a significantly better predictor for compressive strength of LC<sup>3</sup> mortars than bound water. For all LC<sup>3</sup> mixes investigated in this research, the portlandite is consumed, largely after 3 days, through its reaction with metakaolin and

limestone, forming C-(A)-S-H and carboaluminate phases. Hence, a lower portlandite content indicated more pozzolanic reaction, leading to higher amount of hydration products and higher compressive strength [51, 156-158]. Moreover, Figure 5.11 shows a stronger exponential relationship between portlandite consumption over time and the surface resistivity of LC<sup>3</sup> formulations investigated ( $R^2 = 0.903$ ) compared to bound water ( $R^2 = 0.834$ ). A potential reason why the bound water evolution is not as strong a predictor of LC<sup>3</sup> performance compared with the portlandite is that the bound water increased not only with the C-(A)-S-H and carboaluminate contents but also with the remaining gypsum and portlandite contents. In other words, while the amount of hydration products which influence strength and resistivity such as C-(A)-S-H and carboaluminates [33] cannot be differentiated via bound water content, decreasing portlandite content is an indicator of the formation of these phases.





**Figure 5.10 - (a) Relationship between bound water (measured by TGA) and compressive strength, (b) Relationship between portlandite content and compressive strength. The blue dotted line represents the linear trendlines fitted to the data.**



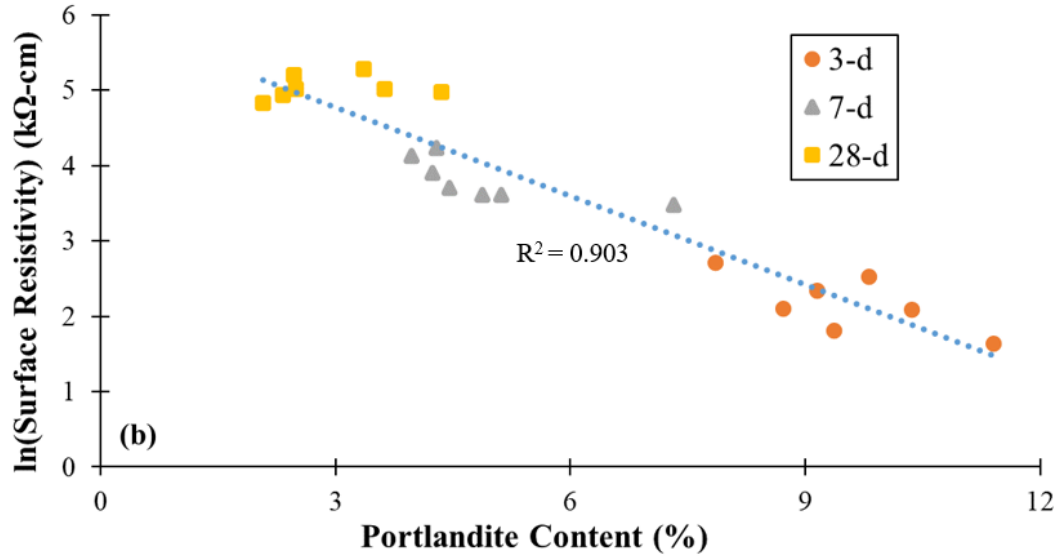


**Figure 5.11 - (a) Relationship between bound water (measured by TGA) and surface resistivity, (b) Relationship between portlandite content and surface resistivity. In both figures y-axis represents the natural logarithm (ln) of the surface resistivity. The blue dotted line represents the linear trendlines fitted to the data.**

### 5.5.3 Compressive strength vs. Surface Resistivity

A logarithmic relationship was found between surface resistivity and strength development of the LC<sup>3</sup> formulations investigated, with a R<sup>2</sup> of 0.917, as shown in Figure 5.12. Equation 5.6 presents the logarithmic relationship found. Specifically, after 3 days of hydration, the rate of surface resistivity increase was significantly higher than the compressive strength for all mixes, as also shown in Table 5.3, 5.4 and 5.5. When all mixes are considered, it is observed that the LC<sup>3</sup> formulations gain > 46% of their 28-d compressive strength but only < 8% of their 28-d surface resistivity until 3 days of hydration.

$$\text{Compressive Strength} = 8.4905 \times \ln(\text{Surface Resistivity}) + 9.4739 \quad (5.6)$$

This great difference in the rate of increase between the resistivity and strength from 3 to 28 days can be explained by early pore refinement ( $\leq 3$  days) and continuous C-(A)-S-H formation. Pore refinement of LC<sup>3</sup> incorporating more than 65% of calcined kaolinite by mass in calcined clay mostly occurs until 3 days, which enhances the strength and surface resistivity but also hinders the formation of carboaluminates [48]. Considering the fixed 2:1 calcined clay-to-limestone ratio used in [48] with ~30% calcined clay in the total solid mass, 65% calcined kaolinite in calcined clay corresponds to ~20% calcined kaolinite by mass in the total solid mixture. Therefore, all formulations investigated here including more than 20% calcined kaolinite in their total solid mass, all mixtures except 55:15:30, can be assumed as the mixtures in which further formation of the carboaluminates have become limited after 3 days because of the unavailability of pores large enough to accommodate these phases [48, 50]. However, as Avet and Scrivener [48] showed, C-(A)-S-H continues forming via ongoing metakaolin reaction and contributes to strength development beyond 3 days. This C-(A)-S-H formation can produce greater increases in surface resistivity than strength, also potentially through its binding of pore solution alkalis [63, 69]. In summary, the hypothesis here is that binding of alkalis into C-(A)-S-H could be a major reason for the significant differences between the rate of increase in surface resistivity and strength beyond 3 days since a lower alkali concentration translates into a lower pore solution conductivity and thus higher surface resistivity. Conversely, compressive strength is not enhanced by this phenomenon, negating the influence of alkali binding and changes in the pore solution conductivity. This hypothesis can be tested through pore solution conductivity and scanning electron microscopy coupled with energy-dispersive spectroscopy (SEM/EDS) measurements in the future.

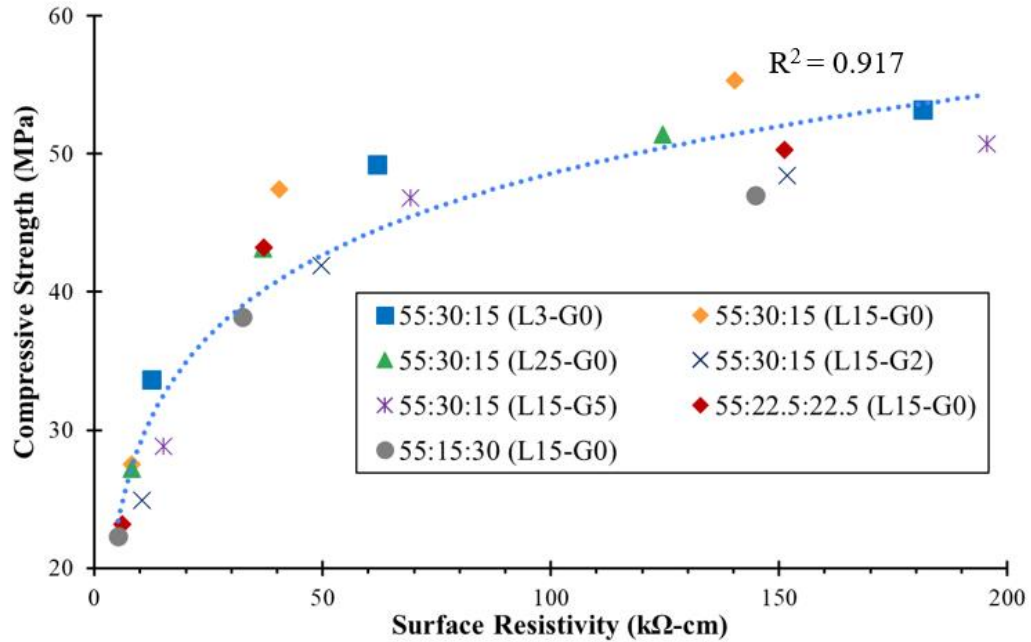


**Figure 5.12 - Relationship between compressive strength development and surface resistivity at 3, 7 and 28 days of hydration. All the resistivity and strength results at 3, 7 and 28 days of hydration are included. The blue dotted line represents the logarithmic trendline fitted to the data.**

## 5.6 Conclusions

The effect of metakaolin content, limestone particle size and added gypsum dosage on the surface resistivity and compressive strength development of LC<sup>3</sup> formulations were investigated. The significance of hydration reactions that consume portlandite for property evolution was demonstrated. Based on the results presented, the following conclusions can be drawn:

- Increasing the metakaolin fraction enhances both the strength development and surface resistivity until 7 days. Beyond 7 days, while surface resistivity is not significantly influenced by the metakaolin fraction, strength is still enhanced. As the TGA results did not reveal significant variations in the total amount of hydrated phases at 28 days from the changes in metakaolin fraction, increasing strength but

similar resistivity achieved with increasing metakaolin fraction beyond 7 days may be due to the physical microstructural differences.

- Fine limestone enhances the surface resistivity until 56 days, while also increases the compressive strength until 7 days. This suggests that the microstructural differences manifested by the filler effect are more evident through surface resistivity testing than through compressive strength.
- Increasing gypsum dosage results in higher surface resistivities at all ages due to the greater amount of ettringite formed in the solid matrix with gypsum. While the increasing ettringite content can lead to higher strength before 3 days of hydration, the diluted fraction of PC by added gypsum results in a decrease of strength beyond 7 days.
- The formation factor data show that optimizing the limestone fineness and gypsum content are of paramount importance to densify microstructure in LC<sup>3</sup> concrete. Considering all mixes, the added gypsum content is the most significant factor until 28 days of hydration for the formation factor. Beyond 28 days, using relatively finer limestone has a greater effect on the formation factor, over both compositional ratio (i.e., PC:MK:LS) and added gypsum content, due to the long-term significance of the filler effect by limestone for microstructural development in LC<sup>3</sup>.
- LC<sup>3</sup> compressive strength and surface resistivity can be predicted from the portlandite content, which decreases after 3 days of hydration due to the formation of strength-giving C-(A)-S-H and carboaluminate phases.



- $LC^3$  concrete surface resistivity and mortar compressive strength have a logarithmic relationship ( $R^2 = 0.917$ ) for mixtures including similar PC content but varying limestone particle size, metakaolin content and gypsum dosages. Greater rate of increase in resistivity compared to strength after 3 days is attributed to the alkali binding into C-(A)-S-H, which can significantly affect the resistivity but not the strength.

Unlike strength experiments, surface resistivity test is non-destructive, rapid, and relatively straightforward to perform. Based on the outcomes of this study, the surface resistivity test appears to be a promising technique to discard strength experiments for  $LC^3$  binders as it can estimate the compressive strength development. For instance, the correlations established in this study enable to predict later age strength if early age resistivity and portlandite content over this time interval of interest are known, without performing any strength testing. Furthermore, the significance of monitoring portlandite content to predict both the surface resistivity and strength of  $LC^3$  demonstrated here can guide not only designing  $LC^3$  formulations but also can facilitate the identification of suitable calcined clay sources based on their pozzolanicity toward achieving strength and durability requirements. It must be noted that the experimental matrix demonstrated here is limited to a certain composition and materials. Therefore, future work should consider a wider range of  $LC^3$  composition such as incorporating impure calcined clay sources. Also, surface resistivity test can be adapted to mortars, which would eliminate the need for coarse aggregate and increase the rate of experimentation, providing a broader view of the complex phenomena underlying this important material.

## **CHAPTER 6. MULTI-OBJECTIVE DESIGN OF LC<sup>3</sup>: SUSTAINABILITY AND STRENGTH**

### **6.1 Introduction**

Limestone-calcined clay cements (“LC<sup>3</sup>”) have been identified as one of the most promising sustainable cementitious binders that can be used at an industrial scale as an alternative to Portland cement (PC) [13, 16]. The appeal of LC<sup>3</sup> originates from the wide availability of the relatively minimally processed minerals that substitute for cement clinker at a relatively high rate, together with lower embedded CO<sub>2</sub> emissions than PC. A typical LC<sup>3</sup> binder formulation consists of 50% PC clinker, 30% calcined clay, 15% limestone and 5% gypsum, by mass [13]. This results in a binder that has lower embedded CO<sub>2</sub> emissions due to a lower amount of calcined constituent materials (namely PC and calcined clay) compared to only PC.

The strength development of LC<sup>3</sup> is significantly impacted by the calcined kaolinite (metakaolin) content in the calcined clay, with a positive linear relationship between compressive strength and metakaolin content observed for up to 7 days. This is due to the rapid reaction of metakaolin leading to the formation of C-(A)-S-H and carboaluminate hydrates, creating a denser microstructure with pore refinement [17, 48]. However, metakaolin is produced by calcining kaolinite between 600°C and 800°C and its embedded global warming potential (GWP) is highly variable depending on the type of fuel used during the calcination process and the type of calcination process (flash calcination versus rotary kiln calcination) [159]. As a result the GWP of metakaolin can be as high as 559 kg CO<sub>2</sub>e/t when coal is used as a primary fuel source [22], or almost 60% of the GWP of PC (see Table 4). Additionally, the cost of pure metakaolin is up to 4-5 times than that of PC.

Therefore, it is critical to optimize the amount of metakaolin in the mix to achieve lower GWP than a conventional mix, while maintaining cost competitiveness and mechanical performance.

The limestone component in LC<sup>3</sup> can be produced at lower cost and with lower GWP than calcined clays (since it does not need to be calcined) and can be tailored through proportioning and grinding (versus clay) [13]. Partial substitution of finely divided limestone for cement can act as a filler, nucleation agent, dilutant, and chemical reactant [26, 43]. The extent of the filler effect is mainly affected by the limestone particle size, while the dilution effect is mainly related to the replacement level of PC with limestone [26]. These effects can be interactive. Improved packing, therefore, shorter interparticle distance with replacing PC partially by fine limestone can accelerate and enhance C-S-H formation due to the increased shearing between particles [9, 25, 55, 160, 161]. However, ternary blends like LC<sup>3</sup> may incorporate different amounts of limestone with various particle diameters that may prompt further complexities. For instance, it is an unresolved question whether the filler or dilution effect of limestone would be dominant in these systems.

Further research is needed to understand the influence of relative proportions and particle size of constituent materials on LC<sup>3</sup> sustainability and performance. To investigate the interaction between the constituent materials, a quantitative multi-objective design tool, which can simultaneously predict the LC<sup>3</sup>'s GWP and compressive strength development is presented. The model is supported by experimental results from various LC<sup>3</sup> compositions with varying proportions of PC:MK:LS and limestone (LS) particle sizes, and a “cradle-to-gate” life cycle assessment (LCA) to quantify the GWP.

## **6.2 Research Significance**

Several studies have examined limestone-blended ternary cements' mechanical properties and their capacity to replace PC to reduce GWP. However, the literature lacks a means by which to optimize a LC<sup>3</sup> mix to concurrently achieve a decrease in CO<sub>2</sub> emissions while improving mechanical properties. This study addresses this research gap and introduces a multi-objective design tool, which can improve the understanding on LC<sup>3</sup> strength development and will be useful for designers in formulating LC<sup>3</sup> while considering sustainability and performance. Furthermore, the methodology used in this paper can be extended to optimize mix design with different raw materials.

## **6.3 Methodology**

Eighteen LC<sup>3</sup> blends were investigated to explore (1) the relative contribution of PC, MK, and LS and (2) the impact of variables such as LS particle size on mechanical properties and overall GWP. Therefore, this section first introduces the experimental program (materials used and tests undertaken), followed by the sustainability assessment of the LC<sup>3</sup> blends. Finally statistical methods adopted to interpret the results, and the multi-objective optimization tool are presented. Figure 6.1 clarifies how each section contributed to the definition of optimized mix designs.

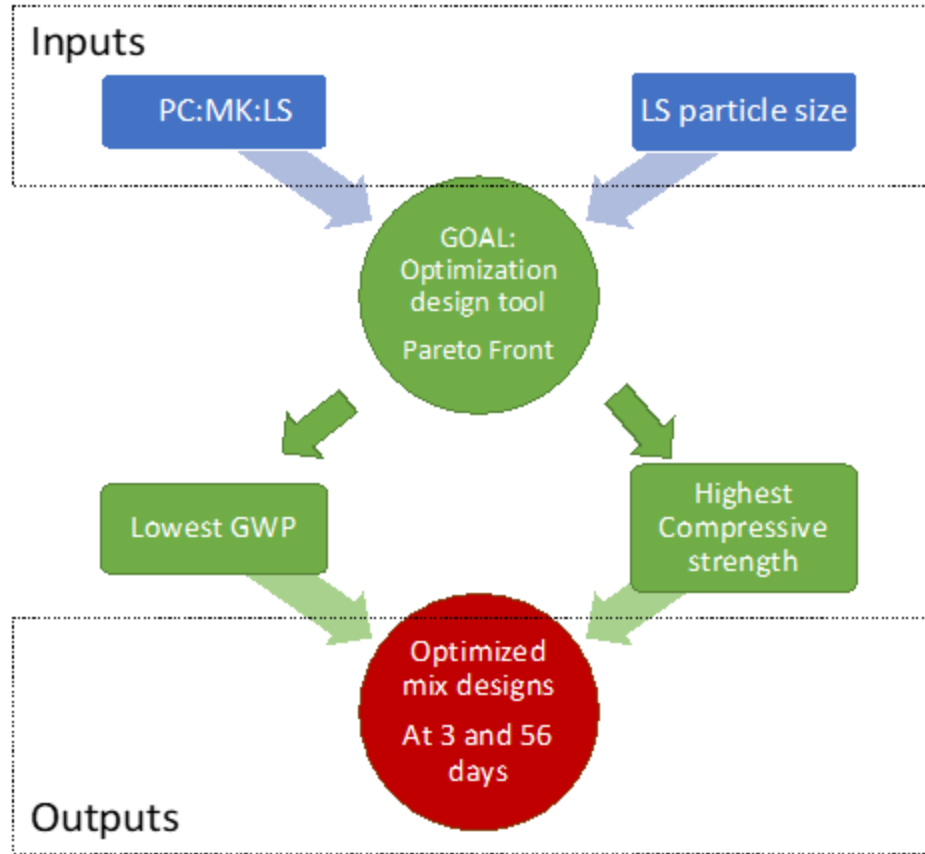


**Figure 6.1 - Methodology followed to obtain the optimized LC<sup>3</sup> mix designs at 3 and 56 days**

### 6.3.1 Mix Design

Eighteen ternary blends composed of PC, metakaolin and limestone, at constant water-to-solid ratio (w/s), were investigated (Table 6.1). Physical and chemical properties of these materials used were introduced in Section 3.3.1. The solids were considered as the total mass of PC, metakaolin and limestone in the binder. In designing these blends, the main motivation was to further reduce the PC and MK content from a typical LC<sup>3</sup> mix, to further enhance sustainability, and to explore the impact of these changes on property evolution. In parallel, the proportions were determined to examine the influence of increasing limestone while maintaining constant PC and MK proportions separately. For

instance, comparing a baseline mixture with Cement:Metakaolin:Limestone (PC:MK:LS) of 55:30:15 with one with 55:15:30 and a baseline of 45:25:30 with 45:20:35 represent pairs of mixtures with high and low PC replacement levels within which the influence of limestone content can be probed. Also, the influence of increasing limestone content at the expense of PC can be elucidated by comparing 50:25:25 with 45:25:30, and 45:20:35 with 40:20:40. The influence of limestone particle size was investigated within blends of the same composition. In this research, gypsum addition and using low-grade calcined clays were not considered to study mainly the filler effect of limestone and mixture proportioning.

The water to solid (PC + metakaolin + limestone) ratio (w/s) used for the mixes was at 0.40, which was proven effective for optimal performance [4]. Deionized (DI) water with a resistivity of 18.2 mΩ-cm (7.2 mΩ-inch) was utilized for all samples. Superplasticizer (SP) (BASF MasterGlenium 7920) first dissolved in mixing water was added to each mix at a dosage of 0.50% by mass of solid. This dosage was kept constant in all mixes for consistency, and slight variations in the flowability observed with the fresh cement pastes were not considered as a predictor in modelling strength development (discussed in later sections).

**Table 6.1 - Experimental matrix by sample identifier, based on mass ratio**

<b>Material (wt.% of solid)</b>	<b>55:30:15</b>	<b>55:15:30</b>	<b>50:25:25</b>	<b>45:25:30</b>	<b>45:20:35</b>	<b>40:20:40</b>
PC	55	55	50	45	45	40
Metakaolin	30	15	25	25	20	20
Limestone*	15	30	25	30	35	40

\*Each blend (PC:MK:LS) was prepared with three limestone particle sizes (L3, L15, L25) corresponding to 18 mixes (6 PC:MK:LS\*3 limestone particle sizes = 18 blends)

### 6.3.2 Analytical and Test Methods

Paste cube specimens (2-inch) were prepared for compression strength testing. Paste was chosen instead of mortar or concrete for the strength testing to focus on the influence of only the binder composition varied by PC:MK:LS and limestone particle size while avoiding any potential impact from aggregates such as formation of the interfacial transition zone in the case of mortar and concrete. First, the measured materials were dry blended for 30 seconds in a countercurrent mixer (Hobart model C100, 10-quart capacity). The paste was mixed on at a low setting for 30 seconds, then on medium for an additional 60 seconds, and stopped for a 30-second rest period. During this time, the sides and bottom of the mixer bowl were scraped to better incorporate the paste solids and any unmixed material. The mixing regime ended with a final 60 seconds on the medium setting. Paste cubes were molded in accordance with procedures in ASTM C109 [71] and then kept in a humidity chamber at  $23\pm2$  °C ( $73.4\pm3.6$  °F) and 100% humidity for 24 h. After demolding, the samples were cured in water ( $23\pm2$  °C ( $73.4\pm3.6$  °F)) until testing was completed [64].

The compressive strength was measured after 3, 7, 28, and 56 days of hydration according to ASTM C109 [71]. Six specimens were tested for each age and the average and standard deviation were reported.

Paste samples for isothermal calorimetry were prepared using a high shear blender for cementitious materials. Heat evolution of blended cement pastes was investigated using an isothermal calorimeter (TAM Air, TA Instruments) with a w/s of 0.40. The samples were prepared outside the calorimeter at room temperature ( $23 \pm 2$  °C ( $73.4 \pm 3.6$  °F)) and then 10 g of pastes were loaded into the calorimeter. Rate of heat evolution and cumulative heat evolution of cement pastes were assessed at 23 °C (73.4 °F) up to 48 hours.

### 6.3.3 Sustainability Analysis

In this study the six mix designs shown in Table 6.1 were also assessed from an environmental perspective, to quantify the possible savings in terms of greenhouse gas (GHG) emissions of LC<sup>3</sup> cements. Life Cycle Assessment (LCA) is an effective method to evaluate the environmental impacts of all products and processes associated to a given system. There are various LCA approaches that can be adopted depending on the analysis and the product of interest. In this case it has been chosen to follow a “cradle-to-gate” approach, considering all the components of the production process but only until the product is released to the market, hence not considering the transportation, placement, maintenance, durability, and disposal of the product outside the cement plant. This is a common approach because cementitious materials can be part of various end-products. In this preliminary LCA, the goal is to compare the global warming potential (GWP),



expressed as kg CO<sub>2e</sub>/t released during the production of LC<sup>3</sup> cements. The choice of the functional unit should reflect the similar function and performance that may be obtained using two products. Since LC<sup>3</sup> cement is potentially used for different end products it has been chosen to consider 1 metric tonne of cement as functional unit similarly to what is considered for PC.

The data used for this estimate were sourced from the literature. The GWP for PC in Table 6.2 was higher than other estimates available in the literature, and this is due to the fuel mix considered in the source. The fuel mix adopted was mainly heavy fuel and coal based and represents the average fuel mix for cement kilns in the United States (data from the Portland Cement Association) [162]. A metric ton of PC production is associated with 942 kg CO<sub>2e</sub> emissions, in which limestone calcination contributes to nearly 60%, in total. The GWP of various limestone sizes significantly varies, shown in Table 6.2, depending on the grinding steps. For instance, the embedded CO<sub>2</sub> emissions associated with the production of one tonne of fine (3 µm) limestone are 269 kg CO<sub>2e</sub>/t, approximately 5 times that of coarse (25 µm) limestone, making coarse limestone a preferable source for LC<sup>3</sup>. Literature shows that the GWP of metakaolin is strongly dependent on the fuel used for the calcination of the kaolin clay, ranging from 94 kg CO<sub>2e</sub>/t if the fuel source is biogas, up to 559 kg CO<sub>2e</sub>/t when coal is the main combustible [22]. In this study, an average fuel mix of heavy fuel and coal was considered, resulting in 435 kg CO<sub>2e</sub>/t of metakaolin produced [22].

**Table 6.2 - GWP (kg CO<sub>2</sub>e/t) of the raw materials used to produce LC<sup>3</sup> cement**

<b>Impact</b>	<b>L3</b>	<b>L15*</b>	<b>L25</b>	<b>PC</b>	<b>MK</b>
GWP	269	117	52	942	435

\*GWP of 15  $\mu$ m limestone is not provided in [24]. Therefore, it is estimated based on the average GWP of 3, 20, and 30  $\mu$ m limestone sizes given in [24].

#### 6.3.4 Statistical methods

With the purpose of achieving computational simplicity in the multi-objective algorithm, multiple linear regression models predicting the 3 and 56-d strength, and GWP of the LC<sup>3</sup> formulations were developed based on compositional variables. These variables were defined as the proportion of PC and metakaolin, and an interaction term between limestone content and the limestone particle size, which will be discussed in later sections. The robustness of each model was assessed with Monte Carlo Cross-Validation algorithm, which randomly splits the data set to 75% training and 25% testing sets 100 times. Root mean squared error (RMSE) – average of 100 computations - (Equation 3.3) was computed as the model performance.

#### 6.3.5 Multi-Objective Optimization

A multi-objective evolutionary algorithm known as the nondominated sorting genetic algorithm (NSGA-II) was utilized, optimizing two objectives (hence the multi-objective optimization) as the strength development and GWP of the LC<sup>3</sup> formulations with varying composition. This genetic algorithm randomly samples a set of points in the compositional space and outputs the predicted strength and GWP for those points. Crossover and mutation occur to create a new generation of points and a sorting algorithm

selects the points which move towards a non-dominated (points where no better objectives exist) Pareto front solutions [163].

A Python package, jMetalPy, was utilized to perform the multi-objective analysis where either the regression model for 3-day or 56-day strength was maximized against a minimization in predicted CO<sub>2</sub>e/t [164].

## **6.4 Results and Discussion**

### *6.4.1 Assessment of Sustainability*

The GWP of the different LC<sup>3</sup> blends introduced in Table 6.1, is given in Figure 6.2. The analysis is based on cement paste (w/s = 0.40, same as for the experiments), hence not including any aggregate source. The variability shown by the error bars represent the impact of the limestone particle size. The GWP of PC paste with w/s of 0.40 is equal to 673 kg CO<sub>2</sub>e/t, considerably higher than that of all LC<sup>3</sup> blends of in Figure 6.2.

Regarding the LC<sup>3</sup> blends investigated, the limestone content and size are factors that highly impact the overall GWP of the blend. Increasing the limestone content at the expenses of PC or metakaolin consistently corresponds to a decrease in GWP. Among six different LC<sup>3</sup> blends, the highest GWP is observed with the mix 55:30:15. If fine limestone (3 µm) is adopted in this mix the embedded CO<sub>2</sub> emission is 492 kg CO<sub>2</sub>e/t, ~27% lower than that of PC. On the contrary, the lowest GWP can be achieved with the mix 40:20:40 prepared using coarse limestone (25 µm). This results in a total of 346 kg CO<sub>2</sub>e/t or approximately 49% lower than PC.

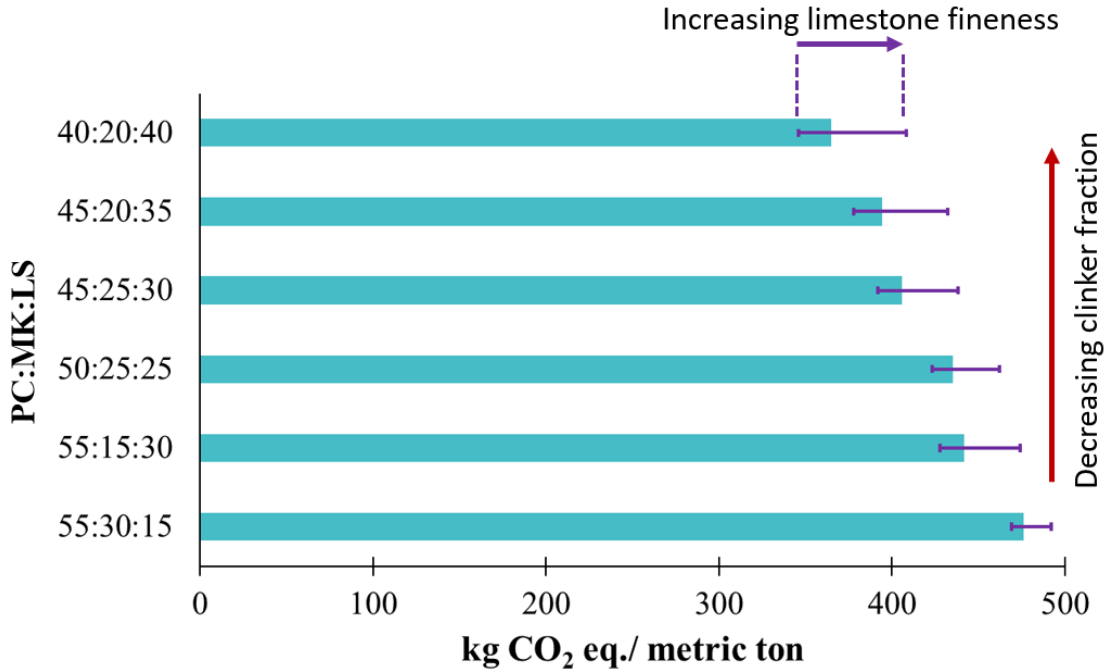


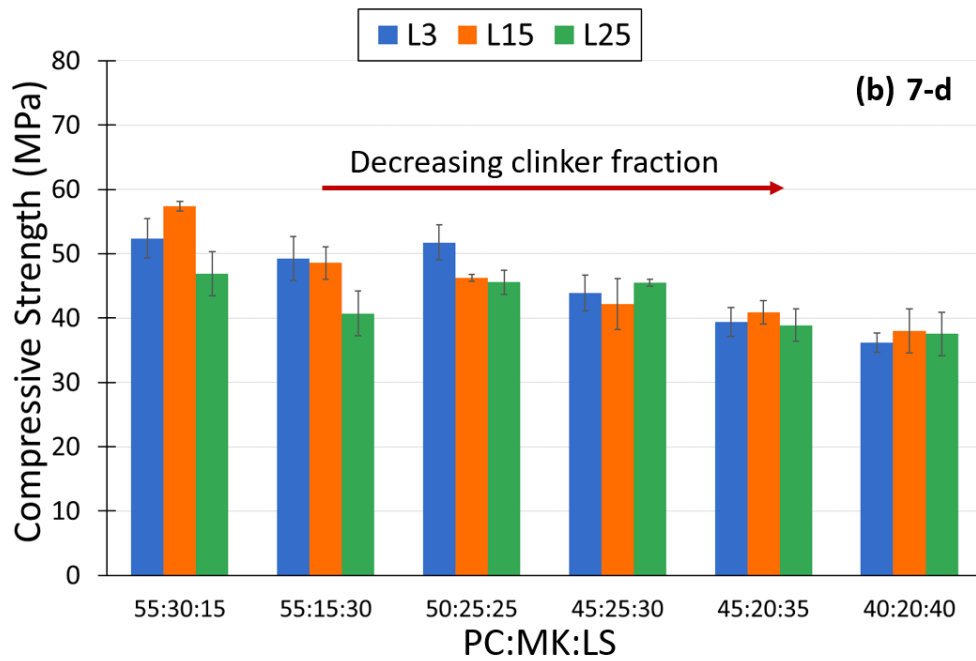
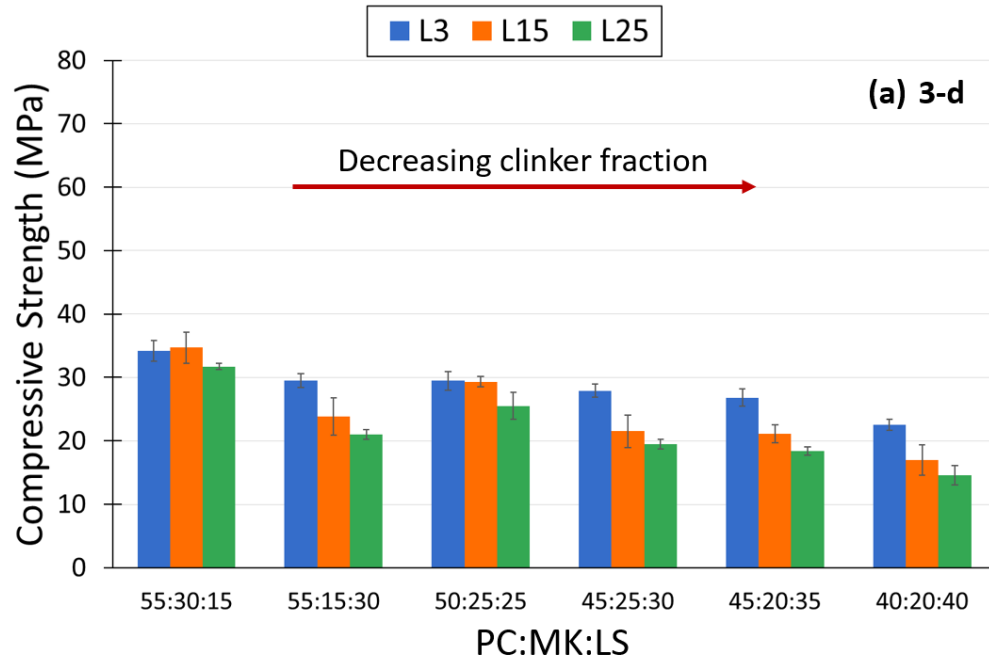
**Figure 6.2 - GWP potential (kg CO<sub>2</sub> e/t) of different LC<sup>3</sup> pastes investigated in laboratory. Purple bars represent the variability from various limestone sizes considered for each mix**

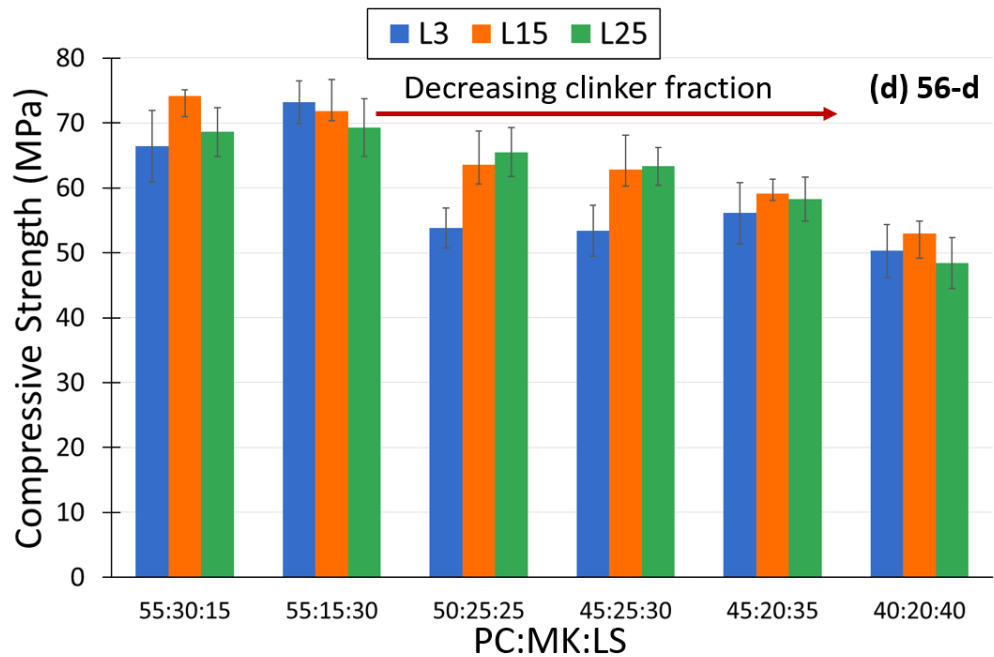
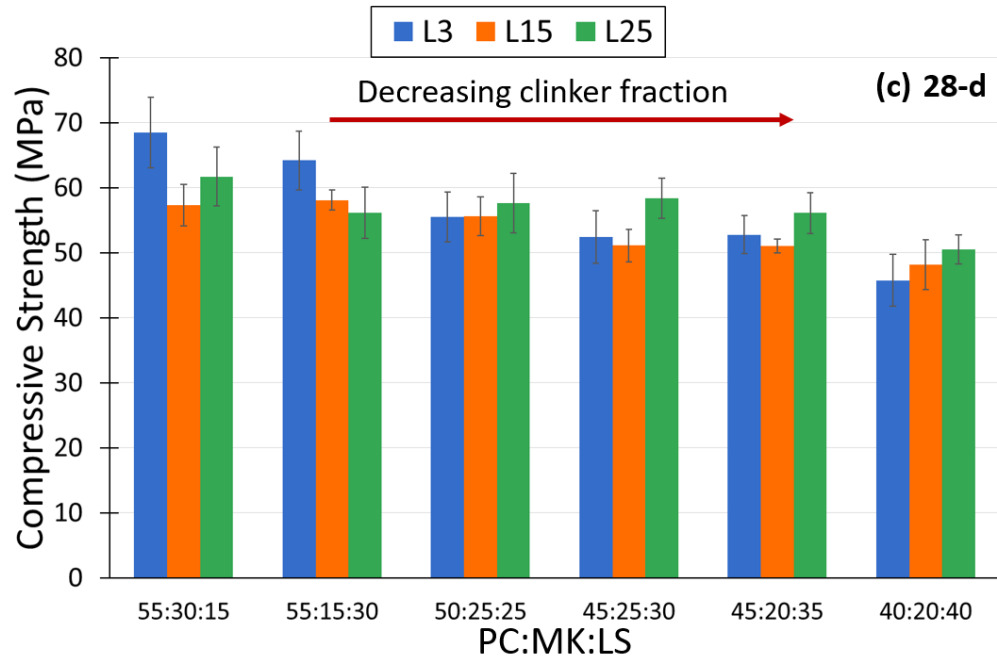
#### 6.4.2 Compressive Strength

Figure 6.3 displays the compressive strength development of LC<sup>3</sup> pastes up to 56 days of hydration, where the limestone particle size is varied for each of the LC<sup>3</sup> pastes. All mixes - except 55:30:15 and 50:25:25 - significantly benefited from incorporating of the finest limestone (L3) for 3-d strength. Most mixes with L3 achieve a higher 3-d strength than those containing L15 or L25, likely due to the accelerated nucleation of early hydration products [26, 142]. It must be noted that 55:30:15 and 50:25:25 are the only mixes studied that do not incorporate limestone in a greater proportion than metakaolin. In these mixes, the higher surface area provided by L3 is apparently less significant than the higher proportion of metakaolin in terms of early ( $\leq$  3-d) strength development. A systematic dependence on limestone particle size is hard to deduce for 7-, 28-, and 56-d strength for none of the pastes investigated. For instance, 55:30:15 achieves a 9.5% higher

7-d strength with L15 compared to L3, and a 22.5% higher 7-d strength than L25. However, L15 results in lower 28-d strength than that achieved with L3 and L25. Such complexity holds for other formulations as well.

Increasing limestone content at the expense of metakaolin does not necessarily lead to lower late strength; this is an important finding for further improving the sustainability of LC<sup>3</sup> binders. For instance, the 3-d strengths are lower in 55:15:30 compared to 55:30:15, regardless of the limestone particle size, despite that both mixes incorporate an equal PC content. However, 55:15:30 achieves a 10.2% higher 56-d strength than 55:30:15 when L3 is used. A similar trend is observed for the mixes 45:25:30 and 45:20:35, with slightly higher metakaolin content of the former mix giving slightly higher 3-d strengths – 4.1% for L3, 6.0% for L15 and 1.9% for L25 - for each of the limestone particle sizes explored, whereas the finest limestone (L3) achieves higher 56-d strength for 45:20:35.





**Figure 6.3 - Compressive strength development of LC<sup>3</sup> pastes including different limestone particle sizes; (a) at 3 days of hydration, (b) 7 days of hydration, (c) 28 days of hydration, (d) 56 days of hydration. Black bars indicate the standard deviation of compressive strength,  $\pm 1\sigma$ , for each mix**

#### 6.4.3 Strength vs. Sustainability

The relationship between compressive strength and GWP influenced by limestone particle size and PC:MK:LS is shown in Figure 6.4. In this figure, the limestone particle size is colored differently to decouple its influence on the GWP estimates and strength. Kernel density estimates using Gaussian kernels are placed above the top horizontal and secondary vertical axes to observe the differences in distributions with three limestone particle sizes.

Effect of fine limestone (L3) is pronounced only for the 3-d strength with a higher GWP than that of LC<sup>3</sup> pastes including medium (L15) and coarse limestone sizes (L25). The mean of 3-d strengths achieved by LC<sup>3</sup> pastes including L3 is 28.4 MPa, which is ~4 and ~7 MPa higher than that of the pastes containing L15 and L25, respectively. This trend does not continue for 56-d strength as L3 resulted in the mean 56-d strength of 58.9 MPa, which is ~3 MPa lower than that of L25, and ~5 MPa lower than that of L15. On the other hand, the mean GWP of LC<sup>3</sup> pastes is always proportional to the limestone particle size, with the finest limestone (L3) corresponding to the highest mean GWP - 451 kg CO<sub>2</sub>e/t for L3, 420 kg CO<sub>2</sub>e/t for L15 and 406 kg CO<sub>2</sub>e/t for L25. These results suggest that coarser limestone particle sizes are favorable compared to fine limestone particles in terms of the sustainability (L25 results in ~10% lower mean GWP than L3) and strength development of LC<sup>3</sup> binders after 3 days of hydration.



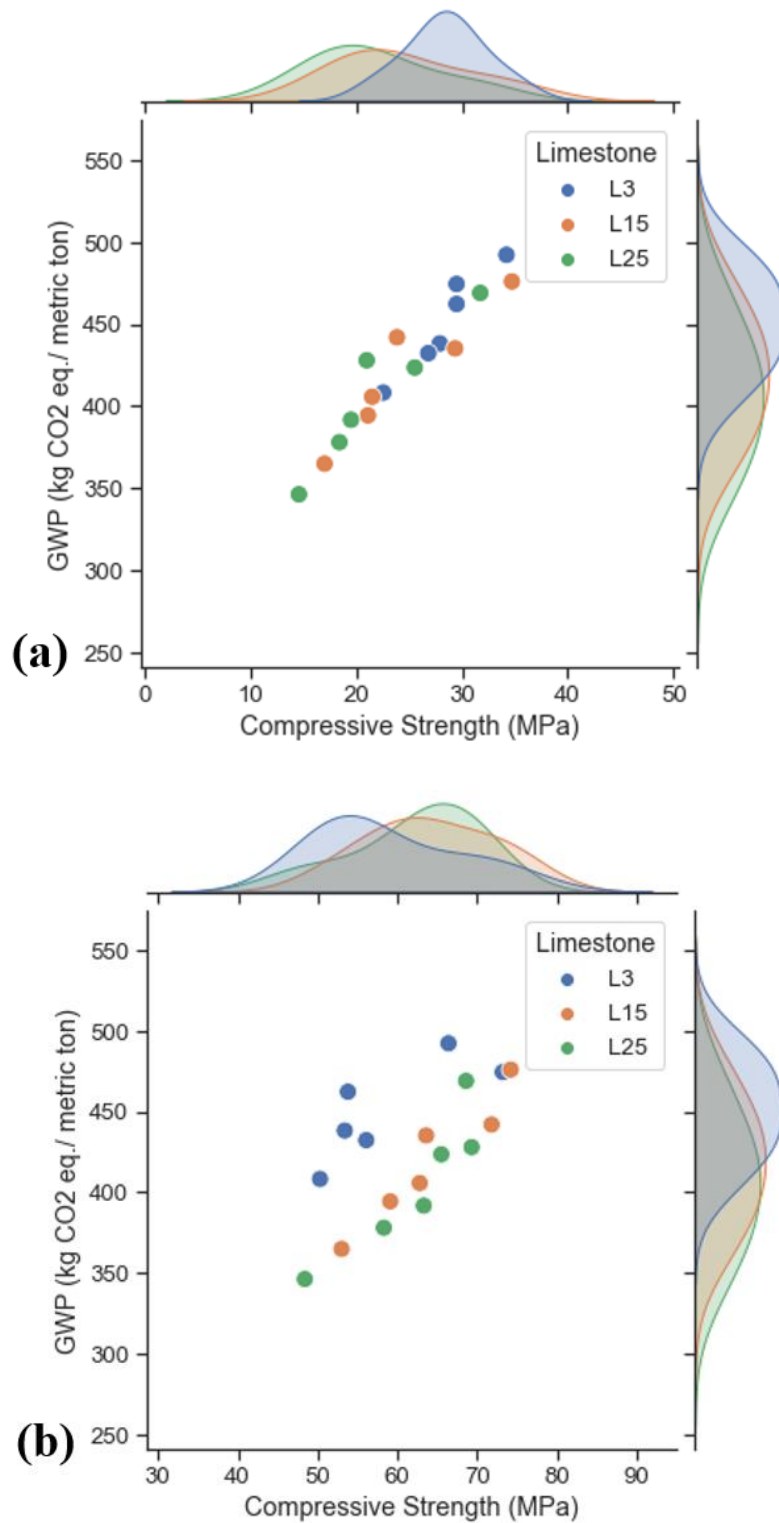


**Figure 6.4 - Strength development vs. GWP of LC<sup>3</sup> pastes investigated; (a) at 3 days of hydration, (b) at 56 days of hydration. Kernel density estimates for each of the limestone particle sizes are shown next to top horizontal and secondary vertical axes**

#### 6.4.4 Significance of Limestone Characteristics on Heat Evolution

As displayed in Figure 6.4, the fine limestone particle size enhances the 3-d strength for LC<sup>3</sup> pastes containing limestone at a higher proportion than metakaolin. This conditional dependence on limestone particle size for the 3-d strength implies an interaction between limestone particle size and content in LC<sup>3</sup>, modifying the early hydration kinetics. To test this hypothesis, an interaction term is defined (Equation (6.1)) and then utilized to explain the hydration kinetics.

$$LSI = \sum D_{50} (\text{Limestone used}) \times \text{Limestone content (wt. \%)} \quad (6.1)$$

The hydration kinetics, herein, were represented by the peak rate of heat release in the acceleration period (obtained from the heat evolution curves), which indicates the reactivity of siliceous and aluminous phases and the rate of precipitation of C-(A)-S-H and ettringite [30, 48]. A strong linear relationship ( $R^2 = 0.82$ ) is found between the LSI parameter and the peak rate of heat release (Figure 6.5). This correlation confirms the hypothesis that the early hydration of LC<sup>3</sup> is not only controlled by the limestone content but also depends on the limestone particle characteristics. In other words, the limestone content and particle size jointly impact the C-(A)-S-H and ettringite formation at early ages. Considering the mix design (Table 6.1) where the proportions of all constituent materials are varying, accurate predictions on early-age hydration parameters using only the limestone content and its median particle diameter is beneficial, and this approach can be adapted for designing and optimizing LC<sup>3</sup> blends.

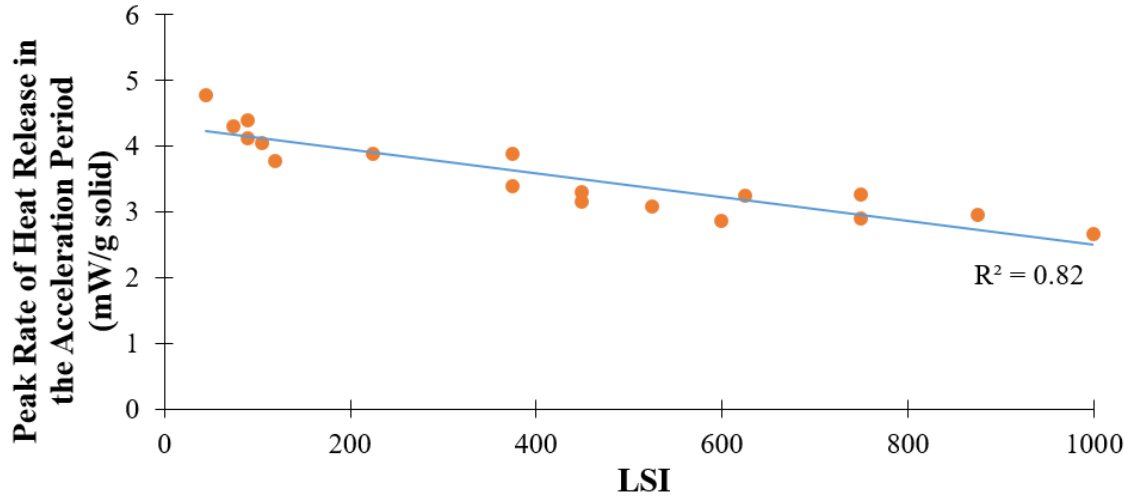


**Figure 6.5 - The peak rate of heat release in the acceleration period (mW/g) explained by LSI**

#### 6.4.5 Statistical Analysis

Motivated by Figure 6.5, showing the significance of the interaction between limestone particle size and content on the hydration kinetics, the interaction term LSI is also used as a predictor variable for LC<sup>3</sup> strength. The multiple regression models to predict LC<sup>3</sup> strength at 3 (Equation 6.2) and 56 days (Equation 6.3) shows a high R<sup>2</sup> of 0.96 and 0.81, with the RMSE of 1.6 MPa (232.1 psi) and 4.6 MPa (667.2 psi), respectively. The equations (6.2 and 6.3) incorporate the non-standardized coefficients for the model variables. Their standardized coefficients and p-values are given separately in Table 6.3.

$$3d \text{ strength (MPa)} = 0.511 \times PC \text{ (wt. \%)} + 0.401 \times MK \text{ (wt. \%)} - 0.010 \times LSI - 4.538 \quad (6.2)$$

$$56d \text{ strength (MPa)} = 1.327 \times PC \text{ (wt. \%)} - 0.033 \times MK \text{ (wt. \%)} + 0.004 \times LSI - 3.547 \quad (6.3)$$

**Table 6.3 - The model variables, standardized coefficients, and p-values**

<b>Model variables</b>	<b>3-d Strength</b>		<b>56-d Strength</b>	
	<b>Standardized coefficient</b>	<b>p-value</b>	<b>Standardized coefficient</b>	<b>p-value</b>
PC (wt. %)	0.492	$4.27 \times 10^{-7}$	0.937	$2.65 \times 10^{-6}$
MK (wt. %)	0.340	$2.49 \times 10^{-5}$	-0.020	0.87
LSI	-0.540	$2.06 \times 10^{-7}$	0.168	0.21

The p-values of the model variables indicate that the PC proportion is a highly significant variable for both 3- and 56-d strength considering 95% confidence level. Evidently, the PC proportion is the only significant variable for 56-d strength regarding the p-values in contrast to 3-d strength. This finding also highlights that coarser limestone particles can be preferred over fine limestone particles without compromising 56-d strength. The regression models demonstrate that increasing PC content improves 3- and 56-d strength. This is not surprising as PC hydration leads to the formation of some strength-giving hydration products such as ettringite and C-(A)-S-H. Also, portlandite that forms from the PC hydration, partakes in the hydration reactions with metakaolin and limestone to precipitate carboaluminate phases that further improves the strength [41, 51].

Increasing metakaolin proportion is shown to enhance the 3-d strength, but it decreases the 56-d strength. This trend is the opposite of what is observed with LSI, which is inversely proportional to the 3-d but directly proportional to the 56-d strength. In fact, both variables demonstrate a minor effect for the 56-d strength compared to the PC proportion. Still, a 56-d strength model excluding the metakaolin proportion and LSI is not

considered to quantify the relative importance of these variables. Higher 3-d strength demonstrated with increasing MK proportion and decreasing LSI indicates that lower limestone proportion – relative to the proportion of PC and metakaolin - with finer particle sizes can be favored for early strength gain ( $\leq 3$ -d). It can also be inferred that statistically meaningful improvements in 56-d strength can be achieved with increasing the PC content in a LC<sup>3</sup> formulation.

#### 6.4.6 Multi-Objective Optimization

The model to predict LC<sup>3</sup> strength at 3 and 56 days shows a high  $R^2$  of 0.96 and 0.81, respectively. However, a more complete assessment of the model's accuracy can be provided through the optimization and testing of a unique LC<sup>3</sup> composed of optimal fractions of PC, MK, and a disparate size distribution of LS. Furthermore, to design an LC<sup>3</sup> blend which also considers the GWP of the designed material is included for a multi-objective optimization. While this model is specifically designed for a w/s of 0.40, the amount of PC, MK, and LS are allowed to vary within the range of the training data and the bounds for the optimization are listed in Table 6.4:

**Table 6.4 - Constraints on the minimum and maximum fractions of each LC<sup>3</sup> component (for w/s = 0.40), considering LS particle size**

<b>Bounds</b>	min	max
PC	40%	55%
MK	15%	30%
LS3	0%	40%
LS15	0%	40%
LS25	0%	40%

Additionally, the following constraints are applied within the optimization:

$$\% PC + \% MK + \%LS\ 3 + \% LS\ 15 + \% LS\ 25 = 100\% \quad (6.4)$$

$$\% LS\ 3 + \% LS\ 15 + \% LS\ 25 \leq 40\% \quad (6.5)$$

Two separate optimizations were performed, the first optimization maximized the 3-day predicted compressive strength while minimizing the GWP, and the optimization maximized the 56-day predicted compressive strength while minimizing the GWP. The corresponding Pareto fronts are shown in Figure 6.6.

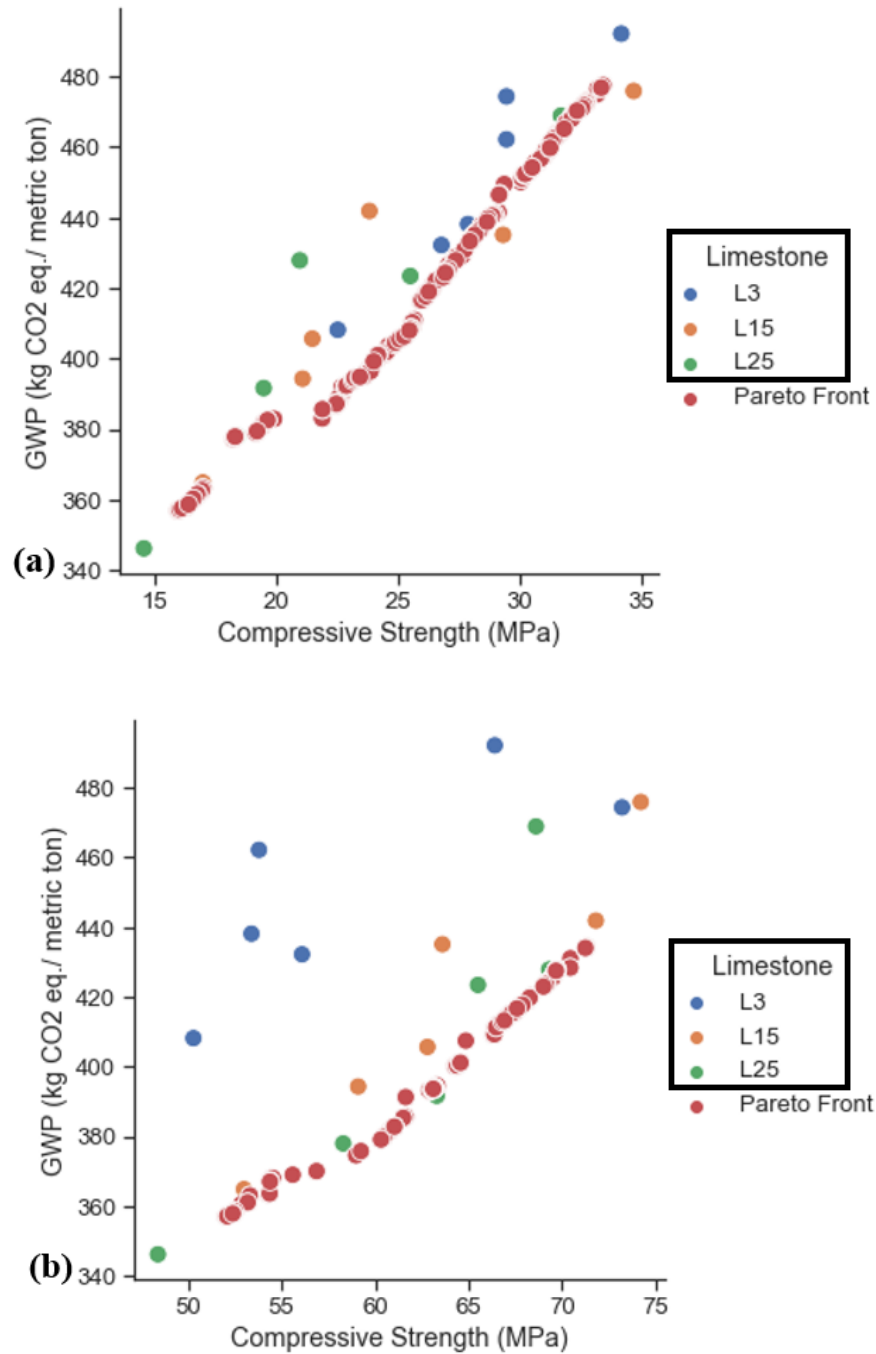


**Figure 6.6 - In multi-objective optimization, there exists a ‘frontier’ of optimal solutions. From this there is an inherent trade-off shown where the maximization of one output leads to a lower value in the other. (a) Shows this Pareto front for the 3-day strength while (b) plots this front for the 56-day strength**

From each of these optimization routines, the Pareto solution which maximizes strength with the lowest possible GWP and minimizes the GWP with the highest possible

predicted strength are selected for testing. The composition, measured and predicted strengths, and GWP of the selected formulations from the Pareto front are shown in Table 6.5.

**Table 6.5 - Compressive strength and GWP of the selected LC<sup>3</sup> compositions from the Pareto front**

	Mix ID	Predicted Strength (MPa)	Measured Strength (MPa)	GWP (kg CO <sub>2</sub> e/t)	PC%	MK%	L3 %	L15 %	L25 %
3-D Strength	P3-L	16.0	16.2	357	40.0	22.0	3.2	0.6	34.2
	P3-H	33.5	29.9	478	53.7	29.9	8.7	7.2	0.5
56-D Strength	P56-L	52.0	53.1	357	40.0	20.1	1.6	17.2	21.1
	P56-H	71.3	69.6	434	54.8	15.0	4.3	1.8	24.1

After testing it is observed that the predictions from the optimization algorithm for both 3- and 56-d strength are satisfactory. The highest discrepancy between the actual and predicted strength is only 10.7%, observed with P3-H. The optimization algorithm proposes the P3-H as the highest 3-d strength formulation, with 8.7% L3 (~58% of the total limestone content). In addition, this formulation has almost the maximum allowed MK content as set by the bounds imposed (30%), highlighting the importance of metakaolin content combined with fine limestone to achieve early strength development.

The combination of the lowest GWP with the highest possible strengths at 3-d (P3-L) and 56-d (P56-L) is reached by minimizing the L3 in the total limestone proportion and the PC and metakaolin contents in the total cementitious solid. This is in line with Figure 6.2, where 40:20:40 including L25 was suggested as the most preferable formulation in terms of GWP. It is noteworthy that P56-L reached 53.1 MPa in compressive strength, with only 40% of PC content. Also remarkable is that the highest 56-d strength (P56-H) is



achieved by minimizing the metakaolin content (15%) and preferring coarser LS (24%), while limiting to 4.3% the finer L3. These results support the premise that the metakaolin content can be lowered and coarser limestone particle sizes can be incorporated to optimize the strength development and GWP of LC<sup>3</sup>.

## 6.5 Conclusions

In an effort to contribute to the design of LC<sup>3</sup>, a multi-objective design tool that can predict the GWP and compressive strength development of LC<sup>3</sup> formulations at w/s of 0.40 is developed. The influence of the PC:MK:LS and the limestone particle size on the property evolution and GWP of LC<sup>3</sup> pastes is examined. Based on the results presented, the following conclusions are drawn:

- LC<sup>3</sup> binders can be formulated with a multi-objective optimization approach considering performance and sustainability with accurate predictions (within 10.7% error rate) for the compressive strength.
- Sustainability of LC<sup>3</sup> is improved by optimizing the limestone particle sizes (up to 10% improvement in the mean GWP considering all PC:MK:LS investigated), preferring coarser limestone particle sizes. The GWP is also lowered by optimizing the relative proportion of the raw materials (PC:MK:LS), especially by using lower cement and metakaolin contents.
- Early compressive strength ( $\leq 3$ -d) is enhanced significantly with the incorporation of fine limestone particle sizes if the limestone proportion is higher than metakaolin. When the sustainability is also considered as a variable, and for strength development after 3 days, coarser limestone particle sizes are favorable.

- The LSI is defined as the multiplication of the limestone particle size and content to explain the peak rate of heat release in the acceleration period thus the early hydration kinetics. Lower LSI corresponds to higher peak rate of heat release, suggesting enhanced formation of C-(A)-S-H. This interaction term is also greatly significant in predicting 3-d strength.

## **CHAPTER 7. CONCLUSIONS AND RECOMMENDATIONS**

### **7.1 Summary of Findings**

This dissertation focused on building composition-property linkages for LC<sup>3</sup> with the purpose of facilitating the transition from the laboratory to field while providing design approaches. An interdisciplinary approach combining materials science with data analytics was followed to elucidate the fresh and hardened properties of LC<sup>3</sup>. Feature engineering allowed for identifying representative and generalizable compositional variables, which can be varied to tailor the fresh properties of LC<sup>3</sup> (i.e., rheology). Analytical methods such as portlandite quantification were used to investigate the microstructural development towards predicting hardened properties such as compressive strength development and surface resistivity.

Chapter 3 proposed a quantitative approach to determining sulfate balance of LC<sup>3</sup>, which can also be applied to other cementitious materials. This was accomplished by NW kernel regression parametrizing the derivatives of the measured heat flow curves obtained from isothermal calorimetry. With this methodology, the influence of various compositional variables (e.g., metakaolin fraction and limestone particle size) on the required sulfate balance and on the early hydration kinetics parameters of LC<sup>3</sup> were quantified. It has been understood that metakaolin fraction is a significant factor in controlling the necessary sulfate addition not only because it can adsorb sulfates but also this research showed that the metakaolin fraction also determines the extent of the effect of other compositional variables, including such as limestone particle size, on the sulfate

balance. Understanding and quantifying these relationships is important to formulate LC<sup>3</sup> with desired performance in terms of both fresh and hardened properties.

Chapter 4 argues that while a single compositional predictor can be used to predict yield stress or plastic viscosity of some PC-based systems (i.e., neat PC and PC-limestone) [113, 133], LC<sup>3</sup> systems require several predictors. For instance, four compositional predictors – K, Al<sub>2</sub>O<sub>3</sub>/SO<sub>3</sub>, TPD and MK/LS – are needed to accurately predict the yield stress of LC<sup>3</sup>. These predictors were identified with stepwise regression. SVR algorithm was suggested to make accurate predictions for both the yield stress and plastic viscosity. Further, the hypothesis relating onset heat to initial yield stress was tested. Increasing onset heat – identified with NW kernel regression method - corresponded with higher yield stresses for pastes incorporating relatively coarse limestone sizes L15 and L25 ( $R^2 = 0.712$ ) and L3 ( $R^2 = 0.809$ ). The yield stress of LC<sup>3</sup> pastes has been found remarkably more sensitive to modifications in composition than onset heat.

Chapter 5 investigated the relationship between surface resistivity and compressive strength development of LC<sup>3</sup> binders to inform design guidance. A strong logarithmic relationship was found between the resistivity and strength development until 28 days ( $R^2 = 0.917$ ) when composition was varied by metakaolin fraction, limestone particle size and added gypsum content. Also, both these properties could be accurately predicted from the changes in portlandite content over time. From the logarithmic relationship observed between the resistivity and strength, it has been hypothesized that binding of alkalis in the pore solution by C-(A)-S-H could be an important factor behind why surface resistivity increased at a much higher rate than strength beyond 3 days. Overall, the findings propose that non-destructive surface resistivity test can discard strength experiments for LC<sup>3</sup>.

Given the increasing environmental awareness due to the climate change it is of paramount importance to formulate cement binders with low CO<sub>2</sub> emissions but with satisfactory performance. Chapter 6 demonstrated that multi-objective optimization can be used to formulate LC<sup>3</sup> pastes with relatively low CO<sub>2</sub> emissions but high 3-d or 56-d compressive strength. Remarkably, 56-d compressive strength higher than 50 MPa could still be achieved with the LC<sup>3</sup> paste including only 40% PC and 20% metakaolin by mass, whose formulation suggested, and 56-d strength predicted by the multi objective optimization algorithm. The results suggested that relatively low metakaolin fractions and coarser limestone particle sizes can be used to optimize the sustainability and compressive strength of LC<sup>3</sup>.

## **7.2 Recommendations for Practice**

This dissertation provides design guidance for fresh (i.e., rheology) and hardened properties (i.e., compressive strength and surface resistivity) of LC<sup>3</sup> supported by empirical findings and predictive models. These findings can inform not only engineers and practitioners in field but also future standards and specifications addressing the formulation of LC<sup>3</sup> binders.

NW kernel regression appears to be a useful technique to parametrize the heat flow curves obtained from isothermal calorimeter. In Chapter 3, this technique allowed to establish a new methodology quantifying the early hydration kinetics parameters of LC<sup>3</sup> pastes. In the future, researchers can use this methodology to investigate the sulfate balance of other alternative cementitious materials or to simply parametrize the heat flow curves in a reproducible manner without following ad hoc procedures.

The modelling results presented in Chapter 4 can be used to modify the yield stress and plastic viscosity of LC<sup>3</sup> pastes. Because the dataset in this dissertation included the rheological properties of only pastes not including any aggregate, yield stress and plastic viscosity predictions by SVR may not be as accurate for mortar or concrete mixtures. Nevertheless, the compositional predictors identified for the paste rheology can still be used to tailor the rheological properties of LC<sup>3</sup> concrete provided that modifications in these predictors (i.e., particle packing) brought about by various aggregate sources are accounted for.

The surface resistivity test is rapid and non-destructive, which allows for the examination of microstructural development in concrete over time. The correlation established between the concrete resistivity and mortar strength development of LC<sup>3</sup> in Chapter 5 is promising in terms of replacing resource-consuming strength experiments with the faster, non-destructive, and inexpensive surface resistivity test. This correlation can be exploited by organizations and owners writing specifications to provide design guidance for LC<sup>3</sup> only based on surface resistivity. In addition, Chapter 5 shows that both the surface resistivity and compressive strength development of LC<sup>3</sup> binders can simply be predicted based on portlandite content over time. RILEM, which is leading the adoption of the R<sup>3</sup> method, can adapt the methodology used for portlandite content quantification in Chapter 5 as an alternative procedure to R<sup>3</sup> portlandite consumption method [158]. Another implication of the findings from Chapter 5 is, perhaps, to predict later age strength from early age resistivity and portlandite content over the time period of interest for LC<sup>3</sup> binders. For instance, if concrete surface resistivity development until 28 days of hydration and paste portlandite content until 90 days of hydration of a given LC<sup>3</sup> formulation are known,

the exponential equation can be found between the resistivity development and portlandite content until 28 days. Using this equation, concrete surface resistivity and then the mortar compressive strength at 90 days can be predicted.

As LC<sup>3</sup> binders are being adapted by the concrete industry over time, formulations of LC<sup>3</sup> must be adjusted to meet performance, cost, and sustainability criteria. This problem can be addressed with the multi objective optimization tool demonstrated in Chapter 6. In this chapter, this tool was used to formulate LC<sup>3</sup> pastes while optimizing GWP and compressive strength. Future research can use this tool to optimize other objectives such as set time, cost, and yield stress depending on the application.

### **7.3 Recommendations for Future Research**

Incorporating inexpensive, widely available impure calcined clay sources is an effective way to further improve the sustainability and cost of LC<sup>3</sup> binders. In this dissertation, however, only a single source of high purity ( $\geq 95\%$  calcined kaolinite) metakaolin was used to minimize variability in the development of composition-property linkages. Another critical limitation of this dissertation regarding material composition is the single source of calcium sulfate carrier used, gypsum. It is anticipated that calcium sulfate carriers other than gypsum such as anhydrite and hemihydrate may correspond with different early hydration thus property evolution of LC<sup>3</sup>. These potential differences in LC<sup>3</sup> properties can originate mainly from varying solubility rates across anhydrite, hemihydrate, and gypsum. Therefore, future research should include impure calcined clay sources and various calcium sulfate carriers in the compositional design space and revisit the findings of this dissertation.

Similar to other studies [63, 77], this dissertation also shows the necessity of superplasticizers to produce LC<sup>3</sup> concrete or mortars at relatively low w/s (i.e., 0.40) desired by the concrete industry. Because LC<sup>3</sup> needs to be produced with locally available clay sources to reveal the sustainability and cost benefits [16], it is of paramount importance to design superplasticizers that are robust against a wide range of clay compositions. Therefore, future research should be devoted to understand how these polymers interacts with various clay minerals [78].

Finally, composition-property relationships should be investigated for common degradation mechanisms such as freeze-thaw and carbonation induced corrosion that were not investigated in this dissertation. New information gained with such future studies – coupled with findings from this dissertation - can facilitate the globalization of LC<sup>3</sup> binders.



## REFERENCES

- [1] K.E. Kurtis, Innovations in cement-based materials: Addressing sustainability in structural and infrastructure applications, *MRS Bulletin*, 40 (2015) 1102-1109.
- [2] M.C.G. Juenger, F. Winnefeld, J.L. Provis, J.H. Ideker, Advances in alternative cementitious binders, *Cement and Concrete Research*, 41 (2011) 1232-1243.
- [3] D. Coffetti, E. Crotti, G. Gazzaniga, M. Carrara, T. Pastore, L. Coppola, Pathways towards sustainable concrete, *Cement and Concrete Research*, 154 (2022).
- [4] U.S. Geological Survey, Mineral Commodity Summaries 2020, U.S. Department of Interior, 2020. <https://pubs.usgs.gov/periodicals/mcs2020/mcs2020.pdf>.
- [5] M. Schneider, The cement industry on the way to a low-carbon future, *Cement and Concrete Research*, 124 (2019).
- [6] A. Petek Gursel, E. Masanet, A. Horvath, A. Stadel, Life-cycle inventory analysis of concrete production: A critical review, *Cement and Concrete Composites*, 51 (2014) 38-48.
- [7] M. Tokyay, *Cement and Concrete Mineral Admixtures*. CRC Press. Boca Raton, (2016).
- [8] M.C.G. Juenger, R. Snellings, S.A. Bernal, Supplementary cementitious materials: New sources, characterization, and performance insights, *Cement and Concrete Research*, 122 (2019) 257-273.
- [9] B. Lothenbach, K. Scrivener, R.D. Hooton, Supplementary cementitious materials, *Cement and Concrete Research*, 41 (2011) 1244-1256.
- [10] PCA, 2021. Roadmap to Carbon Neutrality. [https://www.cement.org/docs/default-source/roadmap/pca-roadmap-to-carbon-neutrality\\_10\\_10\\_21\\_final.pdf?sfvrsn=7ae5fcbf\\_60](https://www.cement.org/docs/default-source/roadmap/pca-roadmap-to-carbon-neutrality_10_10_21_final.pdf?sfvrsn=7ae5fcbf_60)
- [11] McKinsey&Company., Pathways to a Low Carbon Economy. 2009. p. 192. Available from: [https://www.mckinsey.com/~/media/mckinsey/dotcom/client\\_service/sustainability/cost%20curve%20pdfs/pathways\\_lowcarbon\\_economy\\_version2.ashx](https://www.mckinsey.com/~/media/mckinsey/dotcom/client_service/sustainability/cost%20curve%20pdfs/pathways_lowcarbon_economy_version2.ashx)
- [12] A. Chatterjee, T. Sui, Alternative fuels – Effects on clinker process and properties, *Cement and Concrete Research*, 123 (2019).
- [13] K. Scrivener, F. Martirena, S. Bishnoi, S. Maity, Calcined clay limestone cements (LC3), *Cement and Concrete Research*, 114 (2018) 49-56.

- [14] A. Ito, R. Wagai, Global distribution of clay-size minerals on land surface for biogeochemical and climatological studies, *Sci Data*, 4 (2017) 170103.
- [15] R. Fernandez, F. Martirena, K.L. Scrivener, The origin of the pozzolanic activity of calcined clay minerals: A comparison between kaolinite, illite and montmorillonite, *Cement and Concrete Research*, 41 (2011) 113-122.
- [16] S. Sánchez Berriel, A. Favier, E. Rosa Domínguez, I.R. Sánchez Machado, U. Heierli, K. Scrivener, F. Martirena Hernández, G. Habert, Assessing the environmental and economic potential of Limestone Calcined Clay Cement in Cuba, *Journal of Cleaner Production*, 124 (2016) 361-369.
- [17] A. Alujas, R. Fernández, R. Quintana, K.L. Scrivener, F. Martirena, Pozzolanic reactivity of low grade kaolinitic clays: Influence of calcination temperature and impact of calcination products on OPC hydration, *Applied Clay Science*, 108 (2015) 94-101.
- [18] M. Antoni, Investigation of Cement Substitution by Blends of Calcined Clays and Limestone, EPFL thesis (2013), p. 6001
- [19] F. Lolli, Molecular structure and early age behaviour of metakaolin geopolymers: insights from nanoscale modelling. Doctoral Dissertation, Newcastle University, 2019
- [20] A. Menon, C.M. Childs, B. Poczos, N.R. Washburn, K.E. Kurtis, Molecular Engineering of Superplasticizers for Metakaolin-Portland Cement Blends with Hierarchical Machine Learning, *Advanced Theory and Simulations*, 2 (2018).
- [21] F. Lagier, K.E. Kurtis, Influence of Portland cement composition on early age reactions with metakaolin, *Cement and Concrete Research*, 37 (2007) 1411-1417.
- [22] G. Habert, C. Oullet-Plamondon, Recent update on the environmental impact of geopolymers, *RILEM Tech. Lett.* 1 (2016) 17-23.
- [23] R. Fernández López, Calcined clayey soils as a potential replacement for cement in developing countries, EPFL thesis (2009), p. 4302
- [24] “IMA-NA Calcium Carbonate Life Cycle Assessment,” 2016, p. 66
- [25] E. Berodier, K. Scrivener, G. Scherer, Understanding the Filler Effect on the Nucleation and Growth of C-S-H, *Journal of the American Ceramic Society*, 97 (2014) 3764-3773.
- [26] D. Wang, C. Shi, N. Farzadnia, Z. Shi, H. Jia, Z. Ou, A review on use of limestone powder in cement-based materials: Mechanism, hydration and microstructures, *Construction and Building Materials*, 181 (2018) 659-672.
- [27] L.G. Briendl, F. Mittermayr, A. Baldermann, F.R. Steindl, M. Sakoparnig, I. Letofsky-Papst, I. Galan, Early hydration of cementitious systems accelerated by aluminium sulphate: Effect of fine limestone, *Cement and Concrete Research*, 134 (2020).

- [28] D. Marchon, S. Kawashima, H. Bessaies-Bey, S. Mantellato, S. Ng, Hydration and rheology control of concrete for digital fabrication: Potential admixtures and cement chemistry, *Cement and Concrete Research*, 112 (2018) 96-110.
- [29] A. Quennoz, K.L. Scrivener, Interactions between alite and C3A-gypsum hydrations in model cements, *Cement and Concrete Research*, 44 (2013) 46-54.
- [30] F. Zunino, K. Scrivener, The influence of the filler effect on the sulfate requirement of blended cements, *Cement and Concrete Research*, 126 (2019).
- [31] J.d.S. Andrade Neto, A.G. De la Torre, A.P. Kirchheim, Effects of sulfates on the hydration of Portland cement – A review, *Construction and Building Materials*, 279 (2021).
- [32] R. Hay, L. Li, K. Celik, Shrinkage, hydration, and strength development of limestone calcined clay cement (LC3) with different sulfation levels, *Cement and Concrete Composites*, 127 (2022).
- [33] F. Zunino, K. Scrivener, The reaction between metakaolin and limestone and its effect in porosity refinement and mechanical properties, *Cement and Concrete Research*, 140 (2021).
- [34] M. Sharma, S. Bishnoi, F. Martirena, K. Scrivener, Limestone calcined clay cement and concrete: A state-of-the-art review, *Cement and Concrete Research*, 149 (2021).
- [35] S. Nickovic, A. Vukovic, M. Vujadinovic, V. Djurdjevic, G. Pejanovic, Technical Note: High-resolution mineralogical database of dust-productive soils for atmospheric dust modeling, *Atmospheric Chemistry and Physics*, 12 (2012) 845-855.
- [36] H. Mukai, Y. Kon, K. Sanematsu, Y. Takahashi, M. Ito, Microscopic analyses of weathered granite in ion-adsorption rare earth deposit of Jianxi Province, China, *Sci Rep*, 10 (2020) 20194.
- [37] A. Perrot, D. Rangeard, A. Levigneux, Linking rheological and geotechnical properties of kaolinite materials for earthen construction, *Materials and Structures*, 49 (2016) 4647-4655.
- [38] M.E. Awad, A. Lopez-Galindo, M. Setti, M.M. El-Rahmany, C.V. Iborra, Kaolinite in pharmaceuticals and biomedicine, *Int J Pharm*, 533 (2017) 34-48.
- [39] A.Z. Khalifa, Ö. Cizer, Y. Pontikes, A. Heath, P. Patureau, S.A. Bernal, A.T.M. Marsh, Advances in alkali-activation of clay minerals, *Cement and Concrete Research*, 132 (2020).
- [40] T. Abdullahi, Z. Harun, M.H.D. Othman, A review on sustainable synthesis of zeolite from kaolinite resources via hydrothermal process, *Advanced Powder Technology*, 28 (2017) 1827-1840.

- [41] M. Antoni, J. Rossen, F. Martirena, K. Scrivener, Cement substitution by a combination of metakaolin and limestone, *Cement and Concrete Research*, 42 (2012) 1579-1589.
- [42] V.L. Bonavetti, V.F. Rahhal, E.F. Irassar, Studies on the carboaluminate formation in limestone filler-blended cements, *Cem. Concr. Res.* 31 (2001) 853-859.
- [43] B. Lothenbach, G. Le Saout, E. Gallucci, K. Scrivener, Influence of limestone on the hydration of Portland cements, *Cement and Concrete Research*, 38 (2008) 848-860.
- [44] B.H. Zaribaf, K.E. Kurtis, Admixture compatibility in metakaolin–portland-limestone cement blends, *Materials and Structures*, 51 (2018).
- [45] S. Krishnan, A.C. Emmanuel, S. Bishnoi, Hydration and phase assemblage of ternary cements with calcined clay and limestone, *Construction and Building Materials*, 222 (2019) 64-72.
- [46] W. Kunther, Z. Dai, J. Skibsted, Thermodynamic modeling of hydrated white Portland cement–metakaolin–limestone blends utilizing hydration kinetics from <sup>29</sup>Si MAS NMR spectroscopy, *Cement and Concrete Research*, 86 (2016) 29-41.
- [47] F. Avet, K. Scrivener, Hydration Study of Limestone Calcined Clay Cement (LC3) Using Various Grades of Calcined Kaolinitic Clays, *Calcined Clays for Sustainable Concrete* 2018, pp. 35-40.
- [48] F. Avet, K. Scrivener, Investigation of the calcined kaolinite content on the hydration of Limestone Calcined Clay Cement (LC3), *Cement and Concrete Research*, 107 (2018) 124-135.
- [49] H. Maraghechi, F. Avet, H. Wong, H. Kamyab, K. Scrivener, Performance of Limestone Calcined Clay Cement (LC3) with various kaolinite contents with respect to chloride transport, *Materials and Structures*, 51 (2018).
- [50] Y. Briki, F. Avet, M. Zajac, P. Bowen, M.B. Haha, K. Scrivener, Understanding of the factors slowing down metakaolin reaction in limestone calcined clay cement (LC3) at late ages, *Cement and Concrete Research*, 146 (2021).
- [51] S. Krishnan, S. Bishnoi, A numerical approach for designing composite cements with calcined clay and limestone, *Cement and Concrete Research*, 138 (2020).
- [52] T. Oey, A. Kumar, J.W. Bullard, N. Neithalath, G. Sant, G. Scherer, The Filler Effect: The Influence of Filler Content and Surface Area on Cementitious Reaction Rates, *Journal of the American Ceramic Society*, 96 (2013) 1978-1990.
- [53] A. Kumar, T. Oey, G. Falzone, J. Huang, M. Bauchy, M. Balonis, N. Neithalath, J. Bullard, G. Sant, The filler effect: The influence of filler content and type on the hydration rate of tricalcium silicate, *Journal of the American Ceramic Society*, 100 (2017) 3316-3328.

- [54] A. Kumar, T. Oey, S. Kim, D. Thomas, S. Badran, J. Li, F. Fernandes, N. Neithalath, G. Sant, Simple methods to estimate the influence of limestone fillers on reaction and property evolution in cementitious materials, *Cement and Concrete Composites*, 42 (2013) 20-29.
- [55] X. Ouyang, D.A. Koleva, G. Ye, K. van Breugel, Understanding the adhesion mechanisms between C S H and fillers, *Cement and Concrete Research*, 100 (2017) 275-283.
- [56] E.I. Nadelman, Hydration and Microstructural Development of Portland Limestone Cement-Based Materials Doctoral dissertation, Georgia Institute of Technology, 2016.
- [57] M. Maier, R. Sposito, N. Beuntner, K.-C. Thienel, Particle characteristics of calcined clays and limestone and their impact on early hydration and sulfate demand of blended cement, *Cement and Concrete Research*, 154 (2022).
- [58] F. Zunino, K.L. Scrivener, Influence of Kaolinite Content, Limestone Particle Size and Mixture Design on Early-Age Properties of Limestone Calcined Clay Cements (LC3), *Calcined Clays for Sustainable Concrete* 2020, pp. 331-337.
- [59] E.M.J. Bérodier, A.C.A. Muller, K.L. Scrivener, Effect of sulfate on C-S-H at early age, *Cement and Concrete Research*, 138 (2020).
- [60] K. Scrivener, F. Avet, H. Maraghechi, F. Zunino, J. Ston, W. Hanpongpun, A. Favier, Impacting factors and properties of limestone calcined clay cements (LC3), *Green Materials*, 7 (2019) 3-14.
- [61] G. Mishra, A.C. Emmanuel, S. Bishnoi, Influence of temperature on hydration and microstructure properties of limestone-calcined clay blended cement, *Materials and Structures*, 52 (2019).
- [62] Y. Dhandapani, T. Sakthivel, M. Santhanam, R. Gettu, R.G. Pillai, Mechanical properties and durability performance of concretes with Limestone Calcined Clay Cement (LC3), *Cement and Concrete Research*, 107 (2018) 136-151.
- [63] Y. Dhandapani, M. Santhanam, Investigation on the microstructure-related characteristics to elucidate performance of composite cement with limestone-calcined clay combination, *Cement and Concrete Research*, 129 (2020).
- [64] O. Akhlaghi, T. Aytas, B. Tatli, D. Sezer, A. Hodaei, A. Favier, K. Scrivener, Y.Z. Menceloglu, O. Akbulut, Modified poly(carboxylate ether)-based superplasticizer for enhanced flowability of calcined clay-limestone-gypsum blended Portland cement, *Cement and Concrete Research*, 101 (2017) 114-122.
- [65] S. Krishnan, S. Bishnoi, Understanding the hydration of dolomite in cementitious systems with reactive aluminosilicates such as calcined clay, *Cement and Concrete Research*, 108 (2018) 116-128.

- [66] R.G. Pillai, R. Gettu, M. Santhanam, S. Rengaraju, Y. Dhandapani, S. Rathnarajan, A.S. Basavaraj, Service life and life cycle assessment of reinforced concrete systems with limestone calcined clay cement (LC3), *Cement and Concrete Research*, 118 (2019) 111-119.
- [67] R. Gettu, R.G. Pillai, M. Santhanam, A.S. Basavaraj, S. Rathnarajan, B.S. Dhanya, Sustainability-based decision support framework for choosing concrete mixture proportions, *Materials and Structures*, 51 (2018).
- [68] Q.D. Nguyen, T. Kim, A. Castel, Mitigation of alkali-silica reaction by limestone calcined clay cement (LC3), *Cement and Concrete Research*, 137 (2020).
- [69] W. Wilson, F. Georget, K. Scrivener, Unravelling chloride transport/microstructure relationships for blended-cement pastes with the mini-migration method, *Cement and Concrete Research*, 140 (2021).
- [70] T. Chappex, K.L. Scrivener, The influence of aluminium on the dissolution of amorphous silica and its relation to alkali silica reaction, *Cement and Concrete Research*, 42 (2012) 1645-1649.
- [71] ASTM C1260 -14 Standard Test Method for Potential Alkali Reactivity of Aggregates (Mortar-Bar Method), ASTM International, 2014.
- [72] J.M. Khatib, R.M. Clay, Absorption characteristics of metakaolin concrete, *Cement and Concrete Research*, 34 (2004) 19-29.
- [73] P. Hou, T.R. Muzenda, Q. Li, H. Chen, S. Kawashima, T. Sui, H. Yong, N. Xie, X. Cheng, Mechanisms dominating thixotropy in limestone calcined clay cement (LC3), *Cement and Concrete Research*, 140 (2021).
- [74] T.R. Muzenda, P. Hou, S. Kawashima, T. Sui, X. Cheng, The role of limestone and calcined clay on the rheological properties of LC3, *Cement and Concrete Composites*, 107 (2020).
- [75] W.-J. Long, C. Lin, J.-L. Tao, T.-H. Ye, Y. Fang, Printability and particle packing of 3D-printable limestone calcined clay cement composites, *Construction and Building Materials*, 282 (2021).
- [76] S. Ferreiro, D. Herfort, J.S. Damtoft, Effect of raw clay type, fineness, water-to-cement ratio and fly ash addition on workability and strength performance of calcined clay – Limestone Portland cements, *Cement and Concrete Research*, 101 (2017) 1-12.
- [77] D. Zhang, B. Jaworska, H. Zhu, K. Dahlquist, V.C. Li, Engineered Cementitious Composites (ECC) with limestone calcined clay cement (LC3), *Cement and Concrete Composites*, 114 (2020).
- [78] R. Li, L. Lei, T. Sui, J. Plank, Effectiveness of PCE superplasticizers in calcined clay blended cements, *Cement and Concrete Research*, 141 (2021).

- [79] M. Yang, C.M. Neubauer, H.M. Jennings, Interparticle potential and sedimentation behavior of cement suspensions, *Adv. Cem. Based Mater.* 5 (1997) 1–7.
- [80] D. Lowke, C. Gehlen, The zeta potential of cement and additions in cementitious suspensions with high solid fraction, *Cement and Concrete Research*, 95 (2017) 195-204.
- [81] B. Lorentz, H. Zhu, D. Mapa, K.A. Riding, A. Zayed, Effect of Clay Mineralogy, Particle Size, and Chemical Admixtures on the Rheological Properties of CCIL and CCI/II Systems, *Calcined Clays for Sustainable Concrete2020*, pp. 211-218.
- [82] K. Yoshioka, E. Sakai, M. Daimon, A. Kitahara, Role of steric hindrance in the performance of superplasticizers for concrete, *J. Am. Ceram. Soc.* 80 (1997) 2667–2671.
- [83] M.A.B. Beigh, V.N. Nerella, C. Schröfl, V. Mechtcherine, Studying the Rheological Behavior of Limestone Calcined Clay Cement (LC3) Mixtures in the Context of Extrusion-Based 3D-Printing, *Calcined Clays for Sustainable Concrete2020*, pp. 229-236.
- [84] Y. Chen, S. Chaves Figueiredo, Z. Li, Z. Chang, K. Jansen, O. Çopuroğlu, E. Schlangen, Improving printability of limestone-calcined clay-based cementitious materials by using viscosity-modifying admixture, *Cement and Concrete Research*, 132 (2020).
- [85] I. Mehdipour, K.H. Khayat, Elucidating how particle packing controls rheology and strength development of dense cementitious suspensions, *Cement and Concrete Composites*, 104 (2019).
- [86] F. Zunino, K. Scrivener, Factors influencing the sulfate balance in pure phase C3S/C3A systems, *Cement and Concrete Research*, 133 (2020).
- [87] X. Liu, P. Feng, C. Lyu, S. Ye, The role of sulfate ions in tricalcium aluminate hydration: New insights, *Cement and Concrete Research*, 130 (2020).
- [88] A. Quennoz, K.L. Scrivener, Hydration of C3A–gypsum systems, *Cement and Concrete Research*, 42 (2012) 1032-1041.
- [89] S. Joseph, J. Skibsted, Ö. Cizer, A quantitative study of the C3A hydration, *Cem. Concr. Res.* 115 (2019) 145–159.
- [90] ASTM Standard C1679, "Standard Practice for Measuring Hydration Kinetics of Hydraulic Cementitious Mixtures Using Isothermal Calorimetry", ASTM International, West Conshohocken, PA, 2017.
- [91] C. Rodriguez, J.I. Tobon, Influence of calcined clay/limestone, sulfate and clinker proportions on cement performance, *Construction and Building Materials*, 251 (2020).
- [92] ASTM International. ASTM C305, Standard Practice for Mechanical Mixing of Hydraulic Cement Pastes and Mortars of Plastic Consistency. West Conshohocken, PA: ASTM International; 2012.

- [93] C.M. Childs, O. Canbek, T.M. Kirby, C. Zhang, J. Zheng, C. Szeto, B. Póczos, K.E. Kurtis, N.R. Washburn, Cheminformatics for accelerated design of chemical admixtures, *Cement and Concrete Research*, 136 (2020).
- [94] P.J.M. Monteiro, G. Geng, D. Marchon, J. Li, P. Alapati, K.E. Kurtis, M.J.A. Qomi, Advances in characterizing and understanding the microstructure of cementitious materials, *Cement and Concrete Research*, 124 (2019).
- [95] T. Danner, H. Justnes, M. Geiker, R.A. Lauten, Early hydration of C 3 A–gypsum pastes with Ca- and Na-lignosulfonate, *Cement and Concrete Research*, 79 (2016) 333-343.
- [96] D. Marchon, P. Juilland, E. Gallucci, L. Frunz, R.J. Flatt, Molecular and submolecular scale effects of comb-copolymers on tri-calcium silicate reactivity: Toward molecular design, *Journal of the American Ceramic Society*, 100 (2017) 817-841.
- [97] T. Hastie, R. Tibshirani, J. Friedman, *The Elements of Statistical Learning: Data Mining, Inference, and Prediction* 2nd edn (Springer, 2009).
- [98] K. Scrivener, R. Snellings, B. Lothenbach, *A Practical Guide to Microstructural Analysis of Cementitious Materials*, CRC Press, Boca Raton, 2016.
- [99] M. Maier, S. Scherb, A. Neißer-Deiters, N. Beuntner, K.C. Thienel, Hydration of cubic tricalcium aluminate in the presence of calcined clays, *Journal of the American Ceramic Society*, 104 (2021) 3619-3631.
- [100] S. Scherb, M. Maier, N. Beuntner, K.-C. Thienel, J. Neubauer, Reaction kinetics during early hydration of calcined phyllosilicates in clinker-free model systems, *Cement and Concrete Research*, 143 (2021).
- [101] H. Bessaies-Bey, R. Baumann, M. Schmitz, M. Radler, N. Roussel, Organic admixtures and cement particles: Competitive adsorption and its macroscopic rheological consequences, *Cement and Concrete Research*, 80 (2016) 1-9.
- [102] D.P. Bentz, T. Barrett, I. De la Varga, W.J. Weiss, Relating compressive strength to heat release in mortars, *Adv. Civ. Eng. Mater.* 1 (2012) (14 pp.).
- [103] L. Frølich, L. Wadsö, P. Sandberg, Using isothermal calorimetry to predict one day mortar strengths, *Cement and Concrete Research*, 88 (2016) 108-113.
- [104] A.M. Ley-Hernandez, J. Lapeyre, R. Cook, A. Kumar, D. Feys, Elucidating the Effect of Water-To-Cement Ratio on the Hydration Mechanisms of Cement, *ACS Omega*, 3 (2018) 5092-5105.
- [105] J. Cheung, A. Jeknavorian, L. Roberts, D. Silva, Impact of admixtures on the hydration kinetics of Portland cement, *Cement and Concrete Research*, 41 (2011) 1289-1309.



- [106] R. Barbarulo, H. Peycelon, S. Leclercq, Chemical equilibria between C–S–H and ettringite, at 20 and 85 °C, *Cement and Concrete Research*, 37 (2007) 1176-1181.
- [107] N. Roussel, Rheology of fresh concrete: from measurements to predictions of casting processes, *Materials and Structures*, 40 (2007) 1001-1012.
- [108] R. Sposito, N. Beuntner, K.-C. Thienel, Characteristics of components in calcined clays and their influence on the efficiency of superplasticizers, *Cement and Concrete Composites*, 110 (2020).
- [109] W. Meng, A. Kumar, K.H. Khayat, Effect of silica fume and slump-retaining polycarboxylate-based dispersant on the development of properties of portland cement paste, *Cement and Concrete Composites*, 99 (2019) 181-190.
- [110] S. Mantellato, M. Palacios, R.J. Flatt, Relating early hydration, specific surface and flow loss of cement pastes, *Materials and Structures*, 52 (2019).
- [111] Olivas, A. , Helsel, M. , Martys, N. , Ferraris, C. , George, W. and Ferron, R. (2016), Rheological Measurement of Suspensions Without Slippage: Experimental and Model, Technical Note (NIST TN), National Institute of Standards and Technology, Gaithersburg, MD, [online], <https://doi.org/10.6028/NIST.TN.1946> (Accessed March 26, 2022)
- [112] D. Feys, R. Cepuritis, S. Jacobsen, K. Lesage, E. Secrieru, A. Yahia, Measuring Rheological Properties of Cement Pastes: Most common Techniques, Procedures and Challenges, *RILEM Technical Letters*, 2 (2017) 129-135.
- [113] D.P. Bentz, C.F. Ferraris, M.A. Galler, A.S. Hansen, J.M. Guynn, Influence of particle size distributions on yield stress and viscosity of cement–fly ash pastes, *Cement and Concrete Research*, 42 (2012) 404-409.
- [114] N. Roussel, A. Lemaître, R.J. Flatt, P. Coussot, Steady state flow of cement suspensions: A micromechanical state of the art, *Cement and Concrete Research*, 40 (2010) 77-84.
- [115] N. Roussel, G. Ovarlez, S. Garrault, C. Brumaud, The origins of thixotropy of fresh cement pastes, *Cement and Concrete Research*, 42 (2012) 148-157.
- [116] F.D. Larrard, *Concrete mixture proportioning: A scientific approach*. London and New-York: E&FN SPON: An imprint of Routledge, 1999.
- [117] E. Moulin, P. Blanc, D. Sorrentino, Influence of key cement chemical parameters on the properties of metakaolin blended cements, *Cem. Concr. Compos.* 23 (2001) 463–469.
- [118] N.A. Tregger, M.E. Pakula, S.P. Shah, Influence of clays on the rheology of cement pastes, *Cement and Concrete Research*, 40 (2010) 384-391.
- [119] C.M. Childs, *Design and Optimization of Cementitious Systems with Machine Learning*, Doctoral Dissertation, Carnegie Mellon University, 2021.

- [120] T. Sedran, F. De-Larrard, Optimization of SCC thanks to packing model, RILEM Proceedings, 1999, pp. 320–332.
- [121] F. De Larrard, T. Sedran, Optimization of ultra-high-performance concrete by the use of a packing model, *Cement Concr. Res.* 24 (6) (1994) 997–1009.
- [122] A. Miller, Development and optimization of ultra-high performance concrete using local materials, Masters Thesis, Georgia Institute of Technology, 2020.
- [123] F. de Larrard, T. Sedran, Mixture-proportioning of high-performance concrete, *Cement Concr. Res.* 32 (11) (2002) 1699–1704.
- [124] C.J.C. Burges, A tutorial on support vector machines for pattern recognition. *Data Min. Knowl. Discov.* 2, 121–167 (1998).
- [125] B.A. Young, A. Hall, L. Pilon, P. Gupta, G. Sant, Can the compressive strength of concrete be estimated from knowledge of the mixture proportions?: New insights from statistical analysis and machine learning methods, *Cement and Concrete Research*, 115 (2019) 379–388.
- [126] E. Ford, S. Kailas, K. Maneparambil, N. Neithalath, Machine learning approaches to predict the micromechanical properties of cementitious hydration phases from microstructural chemical maps, *Construction and Building Materials*, 265 (2020).
- [127] W.-G. Lei, L.J. Struble, Microstructure and flow behavior of fresh cement paste, *J. Am. Ceram. Soc.* 80 (2005) 2021–2028.
- [128] N. Roussel, H. Bessaies-Bey, S. Kawashima, D. Marchon, K. Vasilic, R. Wolfs, Recent advances on yield stress and elasticity of fresh cement-based materials, *Cement and Concrete Research*, 124 (2019).
- [129] J.M. Makar, G.W. Chan, K.Y. Esseghaier, A peak in the hydration reaction at the end of the cement induction period, *Journal of Materials Science*, 42 (2007) 1388–1392.
- [130] J. Deou, H. Bessaies-Bey, F. Declercq, P. Smith, S. Debon, J. Wallecan, N. Roussel, Decrease of the amount of fat in chocolate at constant viscosity by optimizing the particle size distribution of chocolate, *Food Structure*, 31 (2022).
- [131] J. Hot, H. Bessaies-Bey, C. Brumaud, M. Duc, C. Castella, N. Roussel, Adsorbing polymers and viscosity of cement pastes, *Cement and Concrete Research*, 63 (2014) 12–19.
- [132] I. Navarrete, Y. Kurama, N. Escalona, M. Lopez, Impact of physical and physicochemical properties of supplementary cementitious materials on structural build-up of cement-based pastes, *Cement and Concrete Research*, 130 (2020).

- [133] K. Vance, A. Kumar, G. Sant, N. Neithalath, The rheological properties of ternary binders containing Portland cement, limestone, and metakaolin or fly ash, *Cement and Concrete Research*, 52 (2013) 196-207.
- [134] I. Mehdipour, A. Kumar, K.H. Khayat, Rheology, hydration, and strength evolution of interground limestone cement containing PCE dispersant and high volume supplementary cementitious materials, *Materials & Design*, 127 (2017) 54-66.
- [135] P. Juilland, L. Nicoleau, R.S. Arvidson, E. Gallucci, Advances in dissolution understanding and their implications for cement hydration, *RILEM Technical Letters*, 2 (2017) 90-98.
- [136] K. Scrivener, A. Ouzia, P. Juilland, A. Kunhi Mohamed, Advances in understanding cement hydration mechanisms, *Cement and Concrete Research*, 124 (2019).
- [137] M. Zajac, P. Durdzinski, C. Stabler, J. Skocek, D. Nied, M. Ben Haha, Influence of calcium and magnesium carbonates on hydration kinetics, hydrate assemblage and microstructural development of metakaolin containing composite cements, *Cement and Concrete Research*, 106 (2018) 91-102.
- [138] E.I. Nadelman, K.E. Kurtis, A resistivity-based approach to optimizing concrete performance, *Concr. Int.* (2014) 50–54.
- [139] A.A. Ramezaniapour, A. Pilvar, M. Mahdikhani, F. Moodi, Practical evaluation of relationship between concrete resistivity, water penetration, rapid chloride penetration and compressive strength, *Construction and Building Materials*, 25 (2011) 2472-2479.
- [140] C.M. Tibbetts, J.M. Paris, C.C. Ferraro, K.A. Riding, T.G. Townsend, Relating water permeability to electrical resistivity and chloride penetrability of concrete containing different supplementary cementitious materials, *Cement and Concrete Composites*, 107 (2020).
- [141] ASTM C778, Standard Specification for Standard Sand, ASTM International, West Conshohocken, PA, 2017, <https://doi.org/10.1520/C0778-17.2>.
- [142] K. De Weerd, M.B. Haha, G. Le Saout, K.O. Kjellsen, H. Justnes, B. Lothenbach, Hydration mechanisms of ternary Portland cements containing limestone powder and fly ash, *Cement and Concrete Research*, 41 (2011) 279-291.
- [143] T. Kim, J. Olek, Effects of Sample Preparation and Interpretation of Thermogravimetric Curves on Calcium Hydroxide in Hydrated Pastes and Mortars, *Transportation Research Record: Journal of the Transportation Research Board*, 2290 (2012) 10-18.
- [144] E.S. Fortes, G.A. Parsekian, F.S. Fonseca, Relationship between the compressive strength of concrete masonry and the compressive strength of concrete masonry units, *J. Mater. Civ. Eng.* (2015).

- [145] ASTM International, C618-19 Standard Specification for Coal Fly Ash and Raw or Calcined Natural Pozzolan for Use in Concrete, ASTM International, West Conshohocken, PA, 2019.
- [146] ASTM International, C192/C192M-18 Standard Practice for Making Concrete Test Specimens in the Laboratory, ASTM International, West Conshohocken, PA, 2018.
- [147] R.T. Rios, F. Lolli, L. Xie, Y. Xie, K.E. Kurtis, Screening candidate supplementary cementitious materials under standard and accelerated curing through time-series surface resistivity measurements and change-point detection, *Cement and Concrete Research*, 148 (2021).
- [148] AASHTO Standard T358, Standard Method of Test for Surface Resistivity Indication of Concrete's Ability to Resist Chloride Ion Penetration, American Association of State Highway and Transportation Officials, Washington, DC, 2017.
- [149] Y. Dhandapani, M. Santhanam, Assessment of pore structure evolution in the limestone calcined clay cementitious system and its implications for performance, *Cement and Concrete Composites*, 84 (2017) 36-47.
- [150] R. Spragg, C. Villani, J. Weiss, Electrical Properties of Cementitious Systems: Formation Factor Determination and the Influence of Conditioning Procedures, *Advances in Civil Engineering Materials*, 5 (2016).
- [151] K.A. Snyder, X. Feng, B.D. Keen, T.O. Mason, Estimating the electrical conductivity of cement paste pore solutions from  $\text{OH}^-$ ,  $\text{K}^+$  and  $\text{Na}^+$  concentrations, *Cement and Concrete Research*, 33 (2003) 793-798.
- [152] D.P. Bentz, A virtual rapid chloride permeability test, *Cement and Concrete Composites*, 29 (2007) 723-731.
- [153] F. Avet, X. Li, K. Scrivener, Determination of the amount of reacted metakaolin in calcined clay blends, *Cement and Concrete Research*, 106 (2018) 40-48.
- [154] K.D. Weerdt, E. Sellevold, K.O. Kjellsen, H. Justnes, Fly ash–limestone ternary cements: effect of component fineness, *Advances in Cement Research*, 23 (2011) 203-214.
- [155] M. Zajac, A. Rossberg, G. Le Saout, B. Lothenbach, Influence of limestone and anhydrite on the hydration of Portland cements, *Cement and Concrete Composites*, 46 (2014) 99-108.
- [156] S. Al-Shmaisani, R.D. Kalina, R.D. Ferron, M.C.G. Juenger, Critical assessment of rapid methods to qualify supplementary cementitious materials for use in concrete, *Cement and Concrete Research*, 153 (2022).
- [157] Y. Wang, L. Burris, C.R. Shearer, D. Hooton, P. Suraneni, Strength activity index and bulk resistivity index modifications that differentiate inert and reactive materials, *Cement and Concrete Composites*, 124 (2021).

- [158] X. Li, R. Snellings, M. Antoni, N.M. Alderete, M. Ben Haha, S. Bishnoi, Ö. Cizer, M. Cyr, K. De Weerd, Y. Dhandapani, J. Duchesne, J. Haufe, D. Hooton, M. Juenger, S. Kamali-Bernard, S. Kramar, M. Marroccoli, A.M. Joseph, A. Parashar, C. Patapy, J.L. Provis, S. Sabio, M. Santhanam, L. Steger, T. Sui, A. Telesca, A. Vollpracht, F. Vargas, B. Walkley, F. Winnefeld, G. Ye, M. Zajac, S. Zhang, K.L. Scrivener, Reactivity tests for supplementary cementitious materials: RILEM TC 267-TRM phase 1, *Materials and Structures*, 51 (2018).
- [159] R. San Nicolas, M. Cyr, G. Escadeillas, Characteristics and applications of flash metakaolins, *Applied Clay Science*, 83-84 (2013) 253-262.
- [160] S. Pourchet, I. Pochard, F. Brunel, D. Perrey, Chemistry of the calcite/water interface: Influence of sulfate ions and consequences in terms of cohesion forces, *Cement and Concrete Research*, 52 (2013) 22-30.
- [161] D. Wagner, F. Bellmann, J. Neubauer, Influence of aluminium on the hydration of triclinc C3S with addition of KOH solution, *Cement and Concrete Research*, 137 (2020).
- [162] Marceau, M. L., Nisbet, M. A., and VanGeem, M. G. "Life Cycle Inventory of Portland Cement Concrete," n.d., p. 120.
- [163] Deb, K.; Pratap, A.; Agarwal, S.; Meyarivan, T. A Fast and Elitist Multiobjective Genetic Algorithm: NSGA-II. *IEEE Trans. Evol. Comput.* 2002, 6 (2), 182–197.
- [164] Benitez-Hidalgo, A.; Nebro, A. J.; Garcia-Nieto, J.; Oregi, I.; Del Ser, J. JMetalPy: A Python Framework for Multi-Objective Optimization with Metaheuristics. *Swarm Evol. Comput.* 2019, 51.